Analysis of Intensity of Singular Stress Field for Cylindrical and Three-Dimensional Butt Joints in Comparison with Two-Dimensional Model

By

Fei Ren

Department of Mechanical Engineering

Kyushu Institute of Technology

Acknowledgments

My study at Kyushu Institute of Technology will soon come to an end and, at the completion of my graduation thesis; I wish to express my sincere appreciation to all those who have offered me invaluable help during the four years of my study.

Firstly, I would like to express my heartfelt gratitude to my supervisor, Professor Nao-Aki Noda, for his constant encouragement and guidance. He has walked me through all the stages of the writing of this thesis. I was first introduced to the study in Japan when profess Noda visit Shandong University, and then he helped me with the application of MEXT scholarship, which supported my study in Japan for 4 years. Without his consistent and illuminating instruction and enthusiastic help, this thesis could not have reached its present form.

Secondly, I am also greatly indebted to Dr. Yasushi Takase, who has been supporting my study with patience and kindness since I entered KIT.

My supervisor, Professor Weiming Feng in Shandong University, introduced me to the study in Japan, and helped me in the application of scholarship. I would like to give my thanks to him for all his contribution and encouragement during my toughest period. I am also indebted to him for his constructive comments on my career.

I also owe my sincere gratitude to my friends and my fellow collaborators who gave me their time in helping me work out my problems during the difficult course of the thesis, especially to Mr. Rei Takaki, who helped me with the translation of Japanese.

My thanks would go to my beloved parents, for their loving considerations and great confidence in me all through these years. And I would like give my wife, Mrs. Ye Wang, many thanks for her support and encouragement. Without her companion, I'm not sure I could have the courage to face the difficulty in my study.

Finally, the financial support of MEXT scholarship of Japanese government, which made it possible for my study in Japan, is gratefully acknowledged.

Abstract

Adhesive joints are widely used in numerous industrial sectors, such as automobile, shipbuilding and aeronautics. However, as is known that there is stress singularity at the end of interface for different materials, which may result in the failure of the joint. The intensity of singular stress field (ISSF) has already been discussed for bonded plate under arbitrary material combination, while few studies are available for the ISSF of butt joints in axi-symmetrical and three-dimensional problems, and no results with varying material combination. Thus this research concentrated on the analysis of ISSFs of axi-symmetrical and three-dimensional butt joint problems, which may make a contribution on a general understanding of the strength for the axi-symmetrical and three-dimensional problems. This thesis is composed of total 5 chapters and organized as follows.

Chapter 1 gives an introduction of composites and bonded structures applied to aviation industry, microelectronic packaging, and steel process equipment. With the extensive application of the technology, structural failure problems are emerging, which requires further study. Then, the issues of the research on singularity in the bonded structures are reviewed, and it is found that there are only few papers focused on the ISSF for axi-symmetrical and three-dimensional butt joint problems. Then, the research purpose of this thesis is introduced, focusing on the analysis of ISSF for axi-symmetrical and three-dimensional butt joints.

In Chapter 2, the ISSF variations were clarified over the entire adhesive thickness range for plate butt joint. An effective mesh-independent technique was

applied to obtaining the ISSFs under arbitrary material combinations. The bonded plate, which has been solved by the body force method, was used as the reference solution to eliminate FEM error.

In Chapter 3, the ISSF variations were clarified over the entire adhesive thickness range for cylindrical butt joint. The results were calculated by changing the material combination systematically under the space of Dundurs' parameters. The result of cylindrical butt joint has been compared with that of plate butt joint and the difference was elaborated. The non-singular stresses caused by the circumferential strain are contained in the FEM stresses at the interface end. The accurate method was used for calculating the ISSF from the ratio of the stress obtained by subtracting the non-singular stress to the stress of the plate butt joint adopted as the reference solution. The ISSF of axi-symmetrical problem cannot be governed by the Dunders' parameters, therefore, the maximum and minimum values of the ISSFs were considered and shown in tables and charts in the space of Dundurs' parameters.

In Chapter 4, the adhesive strength of three-dimensional butt joint was studied in terms of the intensity of singular stress on the interface outer edge. The interface stress distributions of three-dimensional butt joint were obtained by using different mesh sizes. It was found that the singularity occurs on the interface outer edges. The stress distributions on the interface outer edge of three-dimensional butt joint were investigated by using the ratios of singular stresses. The adhesive strength on the interface outer edge can be evaluated by the constant critical ISSF as $K_{\sigma c}^{3D}$=const. The ISSF at interface vertex cannot yet be obtained, fillet was considered instead of the vertex. The ISSF distributions on the fillet arc were investigated. The effect of fillet radius on the ISSF was discussed. When the fillet radius $r/W \geq 0.0005$, the adhesive strength can be evaluated by using the ISSF at the middle point of the interface outer

edge.

In the last chapter of this thesis, Chapter 5, main conclusions of this study were summarized for axi-symmetrical and three-dimensional butt joints.

Contents

Acknowledgments.....i

Abstract..... iii

Contents vi

List of tables.....ix

List of figures.....xi

Nomenclature.....xiv

Chapter 1 Introduction 1

1.1 Research backgrounds.....1

1.2 Studies in history.....4

1.3 Research purposes 7

1.4 Overview of chapters 8

1.5 Reference of Chapter 1.....11

Chapter 2 Analysis on intensity of singular stress for plate butt joint in comparison with bonded plate.....16

2.1 Introduction 16

2.2 Mesh-independent technique to evaluate the ISSF of plate butt joint.....19

2.3 Effect of adhesive thickness on the ISSF for plate butt joint 24

2.4 Experimental evaluation of debonding strength of plate butt join 29

2.5 Conclusion.....31

2.6 Reference of Chapter 2.....32

Chapter 3 Analysis on intensity of singular stress for cylindrical butt joint in comparison with plate butt joint 35
3.1 Introduction 35
3.2 Mesh-independent technique to evaluate the ISSF of cylindrical butt joint 36
3.3 Difference of singularity between cylindrical butt joint and plate butt joint 42
3.4 Effect of adhesive thickness on the ISSF for cylindrical butt joint 43
3.5 Discussion of suitable prediction for debonding strength 47
3.6 Analysis results for cylindrical butt joint under arbitrary material combinations 49
3.7 Experimental evaluation of debonding strength of cylindrical butt joint 54
3.8 Conclusion 57
3.9 Reference of Chapter 3 59
Chapter 4 Analysis on intensity of singular stress on the interface outer edge of three-dimensional butt joint 60
4.1 Introduction 60
4.2 Stress distribution on the interface outer edge 61
4.3 ISSF distribution and critical ISSF of three-dimensional butt joint 69
4.4 ISSF distribution and critical ISSF of butt joint with rectangular cross section 74
4.5 ISSF distribution of fillet corner 77
4.6 Conclusion 81
4.7 Reference of Chapter 4 82
Chapter 5 Conclusion 83
Appendix 86
Appendix A: ISSF for the bonded plate 86
Appendix B: ISSF for the bonded cylinder in comparison with the bonded plate 88

Reference of Appendix.....92

List of tables

Table 2.1 Singular index λ for different material combinations.....21

Table 2.2 Mesh-independent FEM stress ratio $\sigma_{ij0,FEM}^{P}/\sigma_{ij0,FEM}^{REF}$.....24

Table 2.3 F_{σ}^{P} and $F_{\sigma}^{P}/F_{\sigma}^{P}|_{h/W\to\infty}$ of butt joint with varying adhesive thickness.....25

Table 2.4 F_{σ}^{P*} and $F_{\sigma}^{P*}/F_{\sigma}^{P*}|_{h/W\to 0}$ of butt joint with varying adhesive thickness 26

Table 2.5 Normalized ISSF F_{σ}^{P*} of a semi-infinite butt joint 28

Table 2.6 Material properties of experimental specimens 30

Table 3.1 Table 3.1 Ratio of $\sigma_{ij0,FEM}^{C}/\sigma_{ij0,FEM}^{P}$.....36

Table 3.2 Non-singular stresses of cylindrical butt joint 41

Table 3.3 Singular stresses of cylindrical butt joint.....41

Table 3.4 The ratios of singular stresses at the interface end of the cylindrical butt joint and the plate butt joint 41

Table 3.5 F_{σ}^{C} and $F_{\sigma}^{C}/F_{\sigma}^{C}|_{h/W\to\infty}$ of cylindrical butt joint by varying adhesive thickness.....44

Table 3.6 F_{σ}^{C*} and $F_{\sigma}^{C*}/F_{\sigma}^{C*}|_{h/W\to 0}$ of cylindrical butt joint with varying adhesive thickness.....45

Table 3.7 Maximum and minimum values of $K_{\sigma}^{C}/K_{\sigma}^{P}$ when $h/W \le 0.01$ 50

Table 3.8 Maximum and minimum values of $\sigma_{z0,FEM}^{C}/\sigma_{z0,FEM}^{P}$ when $h/W \le 0.01$ .51

Table 3.9 Dundurs' parameters (α, β) and order of singular index λ of cylindrical butt joint (aluminum/polyimide).....55

Table 4.1 Stress distributions for three-dimensional joint under tension obtained by different mesh sizes when h/W=0.01 and h/W≥1.....64

Table 4.2 The ratios of stress components at y=0 64

Table 4.3 The ratios of singular stress components at y=0 66

Table 4.4 The ratios of singular stresses when bonded plate is the reference 68

Table 4.5 Material properties of adherent and adhesives 74

Table 4.6 Singular stress ratios on the fillet 79

Table A1 F_{σ}^{P} of bonded plate (h/W≥1.0) 87

Table B1 Maximum and minimum values of $K_{\sigma}^{C}/K_{\sigma}^{P}$ of bonded cylinder (h/W≥1.0) 90

Table B2 Maximum and minimum values of $\sigma_{z0,\,FEM}^{C}/\sigma_{z0,\,FEM}^{P}$ of bonded cylinder (h/W≥1.0) 91

List of figures

Fig. 1.1 The electrical device Chip Scale Package 2

Fig. 1.2 Application of composite in Boeing 787 air plane 2

Fig. 1.3 Debonding from the end of adhesive joint of Chip Scale Package [9] 3

Fig. 1.4 Several forms of composite material interface failure 3

Fig. 1.5 Several types of bonded structure 6

Fig. 1.6 Cylindrical and three-dimensional butt joint 7

Fig. 2.1 Adhesive butt joints 17

Fig. 2.2 Relationship between critical remote tensile stress σ_c, normalized ISSF F_σ and adhesive thickness h 18

Fig. 2.3 Relationship between $K_{\sigma c}$ and h 18

Fig. 2.4 FEM mesh for the plate butt joint (h/W=0.001) and bonded plate (h/W=1) ... 23

Fig. 2.5. F_σ^P is constant when $h/W \geq 1.0$ 27

Fig. 2.6. F_σ^{P*} is constant when $h/W \leq 0.01$ 27

Fig. 2.7 Normalized ISSF F_σ^{P*} of a semi-infinite butt joint 28

Fig. 2.8 Experimental remote debonding stress σ_c of plate butt joint 30

Fig. 2.9 ISSF of experimental specimen 30

Fig. 2.10 Critical ISSF of experimental specimen 31

Fig. 3.1 Plate and cylindrical butt joints 35

Fig. 3.2 (a) v_2, (b) E_2/E_1, (c) K_σ^C/K_σ^P and $\sigma_{z0,FEM}^C/\sigma_{z0,FEM}^P$ values depending on v_1 under fixed (α, β) = (0.8, 0.3) 42

Fig. 3.3 F_σ^C is constant when $h/W \geq 1.0$ 46

Fig. 3.4 F_{σ}^{C*} is constant when $h/W \leq 0.01$ 46

Fig. 3.5 Maximum values of $K_{\sigma}^{C}/K_{\sigma}^{P}$ and $\sigma_{z0,FEM}^{C}/\sigma_{z0,FEM}^{P}$ when $\beta = 0.2$ 48

Fig. 3.6 3.6 Maximum values of $K_{\sigma}^{C}/K_{\sigma}^{P}$ and $\sigma_{z0,FEM}^{C}/\sigma_{z0,FEM}^{P}$ when $\beta = 0.3$ 48

Fig. 3.7 Maximum value of $K_{\sigma}^{C}/K_{\sigma}^{P}$ and $\sigma_{z0,FEM}^{C}/\sigma_{z0,FEM}^{P}$ when $h/W \leq 0.01$ 52

Fig. 3.8 Minimum value of $K_{\sigma}^{C}/K_{\sigma}^{P}$ and $\sigma_{z0,FEM}^{C}/\sigma_{z0,FEM}^{P}$ when $h/W \leq 0.01$ 52

Fig. 3.9 Dundurs' parameters for the several engineering materials 53

Fig. 3.10 Schematic illustration of cylindrical butt joint 54

Fig. 3.11 Experimental remote debonding stress σ_c of cylindrical butt joint 56

Fig. 3.12 ISSF of experimental cylindrical butt joint specimen 56

Fig. 3.13 Critical ISSF of experimental cylindrical butt joint specimen 57

Fig. 4.1 Three-dimensional and two-dimensional butt joint models 61

Fig. 4.2 Mesh details 62

Fig. 4.3 Interface stress distribution of three-dimensional butt joint 63

Fig. 4.4 ISSF distribution on the interface outer edge 69

Fig. 4.5 ISSF distribution near the interface vertex 70

Fig. 4.6 Critical ISSF distribution on the interface outer edge 71

Fig. 4.7 Critical ISSF distribution near the interface vertex 72

Fig. 4.8 Critical ISSF at y=0 73

Fig. 4.9 The butt joint with rectangular cross section 75

Fig. 4.10 ISSF distributions on the interface outer edges of butt joint with rectangular cross section 75

Fig. 4.11 Critical ISSF distributions on the interface outer edges of butt joint with rectangular cross section 76

Fig. 4.12 Critical ISSF at x=0 and y=0 77

Fig. 4.13 Fillet corner in the interface 78

Fig. 4.14 ISSF distribution on the edge of fillet case.....80

Fig. 4.15 ISSF distribution on the fillet arc 80

Fig. A1 ISSF for the bonded plate ($h/W \geq 1.0$) 86

Fig. B1 K_σ^C / K_σ^P and $\sigma_{z0,\,FEM}^C / \sigma_{z0,\,FEM}^P$ in α, β map for bonded cylinder.....89

Nomenclature

E	Young's modulus
$e_{\min}$	Minimum element size
F_σ^C	ISSF of cylindrical butt joint normalized by W, $= K_\sigma^C/\sigma W^{1-\lambda}$
F_σ^{C*}	ISSF of cylindrical butt joint normalized by h, $= K_\sigma^C/\sigma h^{1-\lambda}$
F_σ^P	ISSF of plate butt joint normalized by W, $= K_\sigma^P/\sigma W^{1-\lambda}$
F_σ^{P*}	ISSF of plate butt joint normalized by h, $= K_\sigma^P/\sigma h^{1-\lambda}$
G	Shear modulus
K_σ^C	ISSF for cylindrical butt joint
K_σ^P	ISSF for plate butt joint
$K_{\sigma c}$	Critical ISSF at debonding fracture
h	Adhesive layer thickness
u_{r0}^{CYL}	Real radial displacement of cylindrical butt joint
W	Width and radius of plate and cylindrical butt joints
α, β	Dundurs' parameters
$\varepsilon_{j0,FEM}^C, \gamma_{rz0,FEM}^C$	FEM strain of cylindrical butt joint at interface end
$\varepsilon_{i0,FEM}^P, \gamma_{xy0,FEM}^P$	FEM strain of plate butt joint at interface end
λ	Singular index

ν	Poisson's ratio
σ_c	Adhesive tensile strength
$\sigma_j^C,\ \tau_{rz}^C$	Real stress of cylindrical butt joint
$\sigma_i^P,\ \tau_{xy}^P$	Real stress of plate butt joint
$\sigma_{i0,FEM}$,$\tau_{xy0,FEM}$	FEM stress at interface end
$\sigma_{j0,FEM}^C$,$\tau_{rz0,FEM}^C$	FEM stress of cylindrical butt joint at interface end
$\sigma_{i0,FEM}^P$,$\tau_{xy0,FEM}^P$	FEM stress of plate butt joint at interface end
$\tilde{\sigma}_{j0,FEM}^C$,$\tilde{\tau}_{rz0,FEM}^C$	Non-singular stress of cylindrical butt joint at interface end
σ^{real}	Real stress at interface end

Chapter 1 Introduction

1.1 Research backgrounds

Composites, bonded and multiple-layer structures are widely employed in automotive and aerospace industries as well as in microelectronics packaging. The advantages offered by the chip scale packages include smaller size, lower weight, easier assembly process, lower over-all production costs and improvement in electrical performance. Fig.1.1 demonstrates a wire-bond BGA ball grid array chip [1]. A typical chip scale packaging process starts with the mounting of the die on the interposer using epoxy. The die is then wire-bonded to the interposer using gold or aluminum wires. Plastic encapsulation then follows to protect the die and wires, usually by transfer molding. After encapsulation, solder balls are attached to the bottom side of the interposer. Finally, the parts are separated from the lead frame.

Composites are also widely used in aviation industries. Boeing first had composite used in the manufacturing of the rudder on B767 air plane, and in the B787 air plane, up to 50% of composites were used. Air Bus has also developed its own new air crafts with composites are widely used such as A380 and the new A350XWB [2-8].

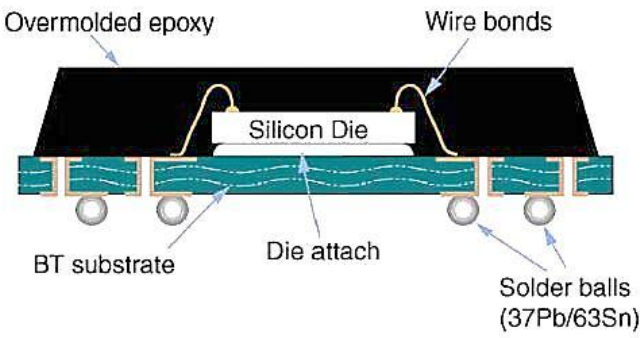

Fig. 1.1 The electrical device Chip Scale Package

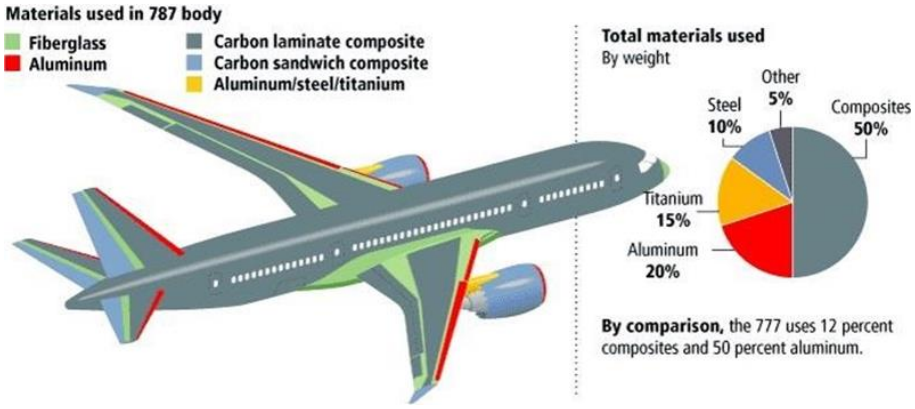

Fig. 1.2 Application of composite in Boeing 787 air plane

However, a mismatch of different materials properties may cause stress singularity at the edge of the interface between different materials, which leads to failure of bonding part in structures. As can be seen from Fig. 1.1, quite a lot interfaces exist inside the CSP assemblies. Stress concentration happens along the interfaces due to the discontinuous of material property and geometric configuration. And cyclic pressure and temperature as well as humidity will increase the speed of delamination. Therefore, there is an increasing concern that the CSP assemblies may

not meet the mechanical and the thermal cycling reliability requirements. In Fig. 1.3, the cross-section image reveals delamination after the 3x JEDEC 260° C reflow test. Delamination initiates at the interface between the underfill and the flux residue, and then propagated along the solder mask [9].

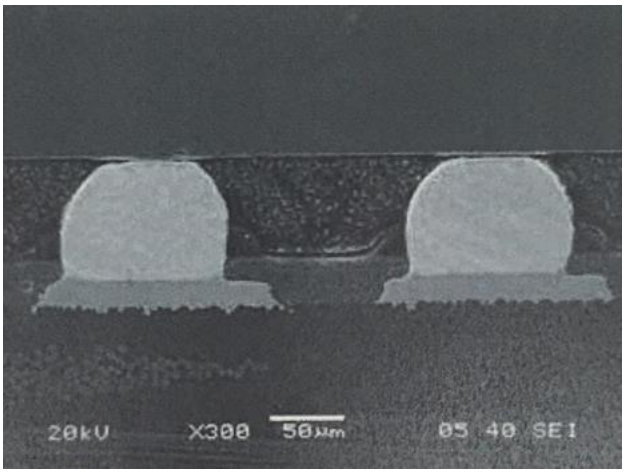

Fig. 1.3 Debonding from the end of adhesive joint of Chip Scale Package [9]

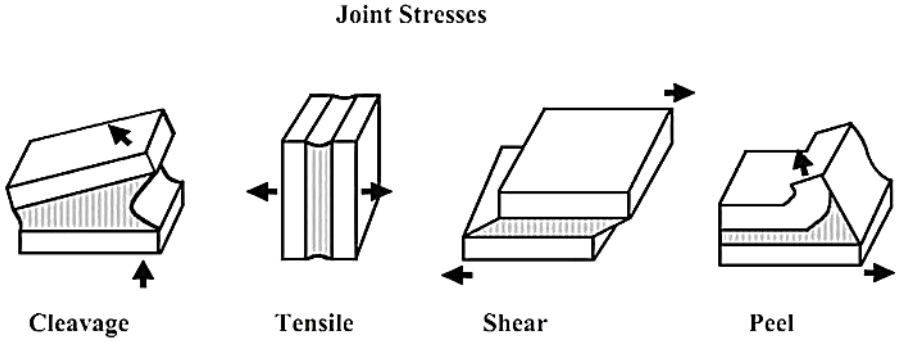

Fig. 1.4 Several forms of composite material interface failure

Fig. 1.4 illustrates several forms of composite material interface failure. The

reliability evaluations based on fracture mechanics on the interface problems composites win quite a lot of attentions. The strength analysis and the failure criteria of bonded structures are becoming more and more important.

1.2 Studies in history

For elastic fracture mechanics concepts on the debonding strength evaluation between dissimilar materials, Williams [10] was the first to determine the characteristic oscillating stress singularity at the crack tip in the elastic interfacial crack problem. Then, elastic solutions around the interface crack tip to specific problems were discussed by Erdogan [11, 12], England [13], and Rice and Sih [14]. Bogy [15] revealed that the stresses at the free end of interface go to infinity (stress singularity) in elastic bi-material planes. This explained why the failures of the bonded structures mostly initiate from the interface end in the engineering.

From the view of linear elastic theory, the stress singularity occurring at the end of interface is an important feature for the bi-material composites. The intersection point of the free boundary and interface is the singular point of elastic stress, which is also the starting point of interface crack. So far, many studies have been done to evaluate this kind of singularity. For two-dimensional models of dissimilar materials structure, the characteristic equation, which controls the order of singularity, was derived [15-27]. Especially, Dunders et al. proposed two elastic mismatch parameters α, β which can be used to express the singularity of a material combination [21, 22]. The Dunders' parameters α, β are defined as the following equation.

$$\alpha = \frac{G_1(\kappa_2+1)-G_2(\kappa_1+1)}{G_1(\kappa_2+1)+G_2(\kappa_1+1)} \qquad \beta = \frac{G_1(\kappa_2-1)-G_2(\kappa_1-1)}{G_1(\kappa_2+1)+G_2(\kappa_1+1)}$$

$$\kappa_j = \begin{cases} \dfrac{3-\nu_j}{1+\nu_j}\left(plane\ stress\right) \\ 3-4\nu_j\left(plane\ strain\right) \end{cases} \left(j=1,2\right)$$

Here, G_j and v_j denote shear modulus and Poisson's ratio for material j in the bonded structure, respectively. The SIFs for the aforementioned problem in plane strain or plane stress are only determined by these problems. Thus these parameters are very important for the later research of biomaterial problems. Bogy et al. made great efforts on the research of singular index λ [15-20], which is the root of the following equation.

$$\left[\sin^2\left(\frac{\pi}{2}\lambda\right)-\lambda^2\right]^2\beta^2+2\lambda^2\left[\sin^2\left(\frac{\pi}{2}\lambda\right)-\lambda^2\right]\alpha\beta+\lambda^2\left[\lambda^2-1\right]\alpha^2+\frac{\sin^2\left(\lambda\pi\right)}{4}=0$$

To understand the existence of singularity at the end of interface or the intensity of singularity is very important for the engineering design. However, there are still confusions about the singular stress field around the interface end [28, 29], strength evaluation method and the evaluation parameters have not been established. Particularly, the present research usually limited with plane problem, the axi-symmetrical problems and three-dimensional problems are also not so clear. And there are only few researches on strength evaluation for these cases.

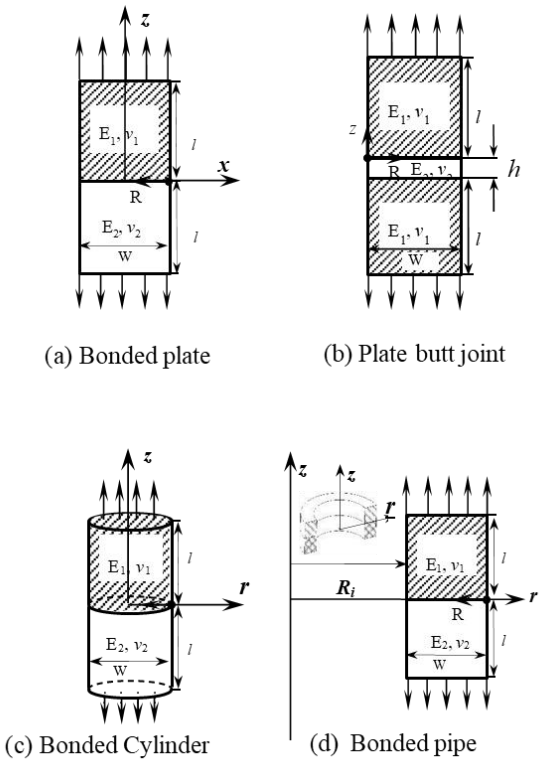

Fig. 1.5 Several types of bonded structure

Recently, some researchers proposed the method for accurately calculating the intensity of the singular stress field for the butt joints (Fig. 1.5(b)) and the single lap joints [39, 40], and reported that the debonding strengths of the adhesive joints can be expressed with $K_\sigma = K_{\sigma c}$ [39, 41, 42], where K_σ is the intensity of singular stress field, $K_{\sigma c}$ is the critical value of the K_σ. Because the K_σ is suitable for evaluating the adhesive strength of the bonded structure, it is expected that it becomes possible to calculate the K_σ of the various bonded structures easily. Moreover, the intensity of singular stress field (ISSF) was discussed for axi-symmetrical bonded structures, bonded cylinder (Fig. 1.5(c)) and pipe (Fig. 1.5(d)) under arbitrary material combination [43].

1.3 Research purposes

The bonded plate (Fig. 1.5 (a)) is actually a special plate butt joint (Fig. 1.5(b)) with very large adhesive thickness $h/W \geq 1$. Similarly, the bonded cylinder (Fig. 1.5 (c)) can be regarded as a special cylindrical butt joint (Fig. 1.6(a)) with very large adhesive thickness $h/W \geq 1$. Previous studies have indicated that the normalized ISSF decreases with decreasing the adhesive thickness under tension [44] and under bending [40, 45]. For large adhesive thickness h, the normalized ISSF becomes constant, and therefore can be estimated easily for any material combination. However, for small adhesive thickness h, which is necessary for evaluating normal adhesive layers, the normalized ISSF decreases with decreasing h and does not become constant.

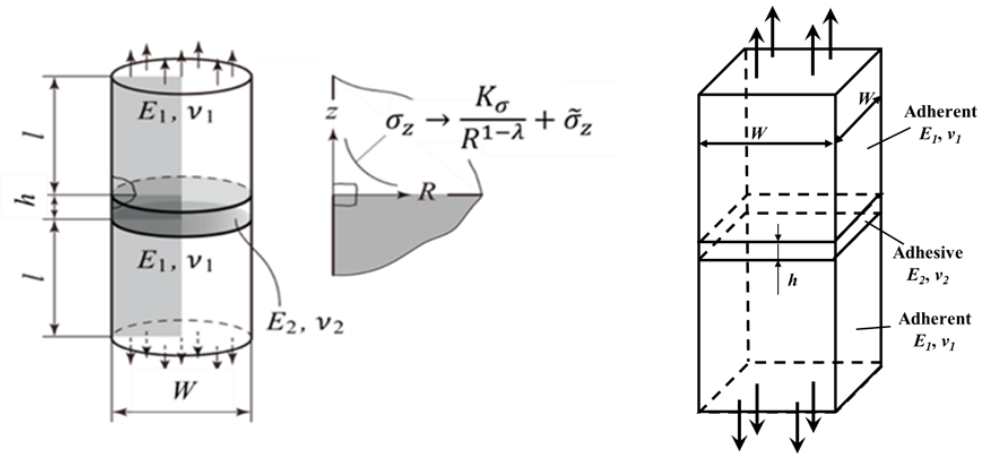

(a) Cylindrical butt joint (b) Three-dimensional butt joint

Fig. 1.6 Cylindrical and three-dimensional butt joint

Two-dimensional plate butt joint (Fig. 1.5(b)) is the simplification of three-dimensional butt joint (Fig. 1.6(b)). Two-dimensional and three-dimensional

butt joints are not completely same. So far, many studies on two-dimensional joints have been carried out theoretically and experimentally, however, the stress distribution of three-dimensional joint is not so clear as that of two-dimensional joint.

In this research, the ISSF variations are clarified over the entire adhesive thickness range for plate and cylindrical butt joints. An effective mesh-independent technique is applied to obtaining the ISSFs under arbitrary material combinations. The result of cylindrical butt joint are compared with that of plate butt joint and the difference is elaborated. The adhesive strength of three-dimensional butt joint is studied in terms of the intensity of singular stress on the interface outer edge. The relation between two-dimensional and three-dimensional butt joints are discussed. The limitation of two-dimensional model is explained. In reality, no corner can be perfectly sharp, a manufactured sharp corner will always present a small fillet radius. Therefore, a fillet is considered instead of the vertex. The ISSF distributions on the fillet arc are investigated and the effect of fillet radius on the ISSF will be discussed.

1.4 Overview of chapters

Adhesive joints are widely used in numerous industrial sectors, such as automobile, shipbuilding and aeronautics. However, as is known that there is stress singularity at the end of interface for different materials, which may result in the failure of the joint. The intensity of singular stress field (ISSF) has already been discussed for bonded plate under arbitrary material combination, while few studies are available for the ISSF of butt joints in axi-symmetrical and three-dimensional problems, and no results with varying material combination. Thus this research concentrated on the analysis of ISSFs of axi-symmetrical and three-dimensional butt

joint problems.

FEM is not suitable for the solution of bi-material problems due to the mesh dependence of singular stress near the end of interface. However FEM is still useful in the analysis of singular stress problems since FEM error can be eliminated in proportional method proposed by Nisitani [46]. This method can accurately obtain the ISSFs of bonded structure as long as the solution of reference problem is accurate enough. The reference problem has already been analytically solved by body force method [47]. This research will extend this method to the axi-symmetrical and three-dimensional butt joint problems.

This thesis is composed of total 5 chapters and organized as follows.

Chapter 1 gives an introduction of composites and bonded structures applied to aviation industry, microelectronic packaging, and steel process equipment. With the extensive application of the technology, structural failure problems are emerging, which requires further study. Then, the issues of the research on singularity in the bonded structures are reviewed, and it is found that there are only few papers focused on the ISSF for axi-symmetrical and three-dimensional butt joint problems. Then, the research purpose of this thesis is introduced, focusing on the analysis of ISSF for axi-symmetrical and three-dimensional butt joints.

In Chapter 2, the ISSF variations are clarified over the entire adhesive thickness range for plate butt joint. An effective mesh-independent technique is applied to obtaining the ISSFs under arbitrary material combinations. The bonded plate, which has been solved by the body force method, is used as the reference solution to eliminate FEM error.

In Chapter 3, the ISSF variations are clarified over the entire adhesive thickness range for cylindrical butt joint. The results are calculated by changing the material

combination systematically under the space of Dundurs' parameters. The result of cylindrical butt joint is compared with that of plate butt joint and the difference is elaborated. The non-singular stresses caused by the circumferential strain are contained in the FEM stresses at the interface end. The accurate method is used for calculating the ISSF from the ratio of the stress obtained by subtracting the non-singular stress to the stress of the plate butt joint adopted as the reference solution. The ISSF of axi-symmetrical problem cannot be governed by the Dunders' parameters, therefore, the maximum and minimum values of the ISSFs are considered and shown in tables and charts in the space of Dundurs' parameters.

In Chapter 4, the adhesive strength of three-dimensional butt joint is studied in terms of the intensity of singular stress on the interface outer edge. The interface stress distributions of three-dimensional butt joint are obtained by using different mesh sizes. It is found that the singularity occurs on the interface outer edges. The stress distributions on the interface outer edge of three-dimensional butt joint are investigated by using the ratios of singular stresses. The adhesive strength on the interface outer edge can be evaluated by the constant critical ISSF as $K_{\sigma c}^{3D}$=const. The ISSF at interface vertex cannot yet be obtained, fillet is considered instead of the vertex. The ISSF distributions on the fillet arc were investigated. The effect of fillet radius on the ISSF was discussed. When the fillet radius $r/W \geq 0.0005$, the adhesive strength can be evaluated by using the ISSF at the middle point of the interface outer edge.

In Chapter 5, main conclusions of this study are summarized for axi-symmetrical and three-dimensional butt joints.

1.5 Reference of Chapter 1

[1] AMD. Designing With Ball Grid Array Packages [online] Available from https://www.jlab.org/accel/eecad/pdf/044bgapackages.pdf

[2] 柳澤誠一:航空機の構造接着とシーリング技術，工業材料，43-10 (1995), 118-125.

[3] 柳澤誠一:航空・宇宙分野への応用，接着，46-12 (2002), 540-546.

[4] J. M. Anglin: Aircraft Applications, Engineered Materials Handbook Volume I Composites, ASM International (1987), 801.

[5] J. Mcguire and R. Varanasi : Boeing Structural Design and Technology Improvements, SAMPEJ., 38-3(2002) 51-57.

[6] Hinrichsen: A 380-Flagship Aircraft for the New Century, SAMPEJ., 38-3 (2002), 8-12.

[7] 酒井康行: 超大型旅客機 A 380 の構造材料技術，日本複合材料学会誌，29-5(2003)，171-176.

[8] 平野英樹，新版複合材料技術総覧，産業技術サービスセンター，(2011), pp.155-177.

[9] Zhao, R., Ji, Q., Carson, G, Todd, M. and Shi, Cx, 2007, Flux and underfill compatibility in a lead-free environment. [online] Available from http://electroiq.com/blog/2007/08/flux-and-underfill-compatibility-in-a-lead-free-environment

[10] Williams, M.L., The stress around a fault or crack in dissimilar media. Bull. Seismol. Soc. America, 49 (1995), 199-208.

[11] Erdogan, F., Stress distribution in non-homogeneous elastic plane with cracks. Trans. ASME., Series E, J. Appl. Mech., 30 (1963), 232-236.

[12] Erdogan, F., Stress distribution in bonded dissimilar materials with cracks. Trans. ASME., Series E, J. Appl. Mech., 32 (1965), 403-410.

[13] England, A.H., A crack between dissimilar media. Trans. ASME., Series E, J. Appl. Mech., 32 (1965), 400-402.

[14] Rice, J.R. and Sih, G.C., Plane problems of cracks in dissimilar media. Trans. ASME., Series E, J. Appl. Mech., 32 (1965), 418-423.

[15] Bogy, D. B., Edge Bonded Dissimilar Orthogonal Elastic Wedges under Normal and Shear Loadings, Journal of Applied Mechanics, 35 (1968), 146-154.

[16] Bogy, D. B., On the Problem of Edge Bonded Elastic Quarter Planes Loaded at Boundary, Journal of Solids and Structures, 6 (1970), 1287-1313.

[17] Bogy, D.B., Two Edge Bonded Elastic Wedges of Different Materials and Wedge Angles under Surface Tractions, Journal of Applied Mechanics, 38 (1971), 377-386.

[18] Bogy, D. B., The Plane Solution for Joined Dissimilar Elastic Semistrips under Tensions, Journal of Applied Mechanics, 42 (1975), 93-98.

[19] Bogy, D. B. , On the Problems of a Loaded Crack Terminating at a Material Interface, Body, D. B. , Edge Bonded Dissimilar Orthogonal Elastic Wedges under Normal and Shear Loadings, Journal of Applied Mechanics, 35 (1968), 146-154.

[20] Bogy, D. B., The Plane Elastostatic Solution for a Symmetric Loaded Crack in a Strip Composite, Int. J. Engng. Sci., 11 (1973), 985-966.

[21] Dunders, J., Discussion of edge bonded dissimilar orthogonal elastic wedges under normal and shear loading, Journal of Applied Mechanics, 36 (1969) 650-652.

[22] Dunders, J., Effect of Elastic Constants on Stress in a Composite under Plane

Deformations, Journal of Composite Materials, 1 (1967), 310.

[23] Hein, V. L., Erdogan, F., Stress Singularity in a Two Materials Wedge, Journal of Fracture Mechanics, 7 (1971), 317-329.

[24] Comninou, M., Dunders, J., A Closed Crack Tip Terminating at an Interface, Journal of Applied Mechanics, 46 (1979), 97-100.

[25] Lin, K.Y., Mar, J. W. , Finite Element Analysis of Stress Intensity Factors for Cracks at a Bimaterial Interface, Journal of Fracture, 12-4 (1976), 521-531.

[26] Williams, M. L., The Stress around a Fault or Crack in Dissimilar Media. Bulletin of the Seismological Society of America, 49-2 (1959), 199-204.

[27] Williams, M. L., Stress Singularities Resulting from Various Boundary Conditions in Angular Corners of Plates in Extension, Trans, of ASME, 74 (1952), 526-528.

[28] 服部敏雄，坂田荘司等，応力特異場パラメータを用いた接着界面強度評価，日本機械学会論文集 A, 54-499 (1988), 597-603.

[29] 服部敏雄，応力特異場パラメータを用いた接着継手の強度評価，日本機械学会論文集 A, 56-523 (1990)，618-623.

[30] Williams, M. L., Journal of Applied Mechanics, Trans. ASME, 24-1 (1957), 109.

[31] Irwin, G. R., Handbuch der Physik, 6 (1988), 551, Spring-Verlag.

[32] Erdogan, F., Stress Distribution in a Nonhomogeneous Elastic Plane with Cracks, Journal of Applied Mechanics, 30 (1963), 232-238.

[33] Erdogan, F., Stress Distribution in Bonded Dissimilar Materials with Cracks, Journal of Applied Mechanics, 32 (1965), 403-411.

[34] Erdogan, F., Stress Distribution in Bonded Dissimilar Materials Containing Circular or Ring-shaped Cavities, Journal of Applied Mechanics, 32 (1965),

829-836.

[35] England, A. H., A Crack between Dissiliar Media, Journal of Applied Mechanics, 32 (1965), 400-407.

[36] Sih, G. C. , Rice, J. R., The Bending of Plates of Dissiliar Materials with Cracks, Journal of Applied Mechanics, 31 (1964), 477-483.

[37] Rice, J.R., Sih, G. C., Plane Problems of Cracks in Dissiliar Media, Journal of Applied Mechanics, 32 (1965), 418-423.

[38] Muskhelishvili, N. I., Some Basic Problems of Mathmatical Therory of Elasticity, 4th. ed (1963), Noordhoff.

[39] Miyazaki, T., Noda, N. -A., Li, R., Uchikoba, T., Sano, Y., Debonding criterion for single lap joints from the intensity of singular stress field, Journal of the Japan Institute of Electronics Packaging, 16-2 (2013), 143 - 151(in Japanese).

[40] Zhang, Y., Noda, N. -A., Wu, P., Duan, M., Corrigendum to “A mesh-independent technique to evaluate stress singularities in adhesive joints”, International Journal of Adhesion and Adhesives, 60-774 (2015), 130.

[41] Miyazaki, T., Noda, N. -A., Uchikoba, T., Li, R., Sano, Y., Proposal of a Convenient and Accurate Method for Evaluation of Debonding Strength, Transactions of the Society of Automative Engineers of Japan, 45-5 (2014), 895 - 901 (in Japanese).

[42] Noda, N. -A., Miyazaki, T., Uchikoba, T., Li, R., Sano, Y., Takase, Y., Debonding strength evaluation in terms of the intensity of singular stress at the interface corner with and without fictitious crack, International Journal of Adhesion and Adhesives, 61 (2015), 46 - 64.

[43] Miyazaki, T., Noda, N.A., Ren, F., Wang, Z., Sano, Y., Iida, K., Analysis of intensity of singular stress field for bonded cylinder and bonded pipe in

comparison with bonded plate, International Journal of Adhesion and Adhesives, 77 (2017), 118-137.

[44] Zhang, Y., Noda, N.A., Takaishi, K.T., Lan, X., Effect of Adhesive Thickness on the Interface of Singular Stress at the Adhesive Dissimilar Joint. Transactions of the Japan Society of Mechanical Engineers Series A, 77 (2011), 360-372.

[45] Zhang, Y., Noda, N.A, Wu, P.Z, Duan, M.L., A Mesh-Independent Technique to Evaluate Stress Singularities in Adhesive Joints, International Journal of Adhesion & Adhesives, 57 (2015), 105-117.

[46] Teranishi T, Nisitani H. Determination of highly accurate values of stress intensity factor in a plate of arbitrary form by FEM. Trans JSME., 65 (1999), 2032-2037.

[47] Chen, D.H., Nishitani, H. Intensity of singular stress field near the interface edge point of a bonded strip. Trans. JSME., 59 (1993), 2682-2686.

Chapter 2 Analysis on intensity of singular stress for plate butt joint in comparison with bonded plate

2.1 Introduction

Adhesive joints are widely used in numerous industrial sectors, such as automobile, shipbuilding and aeronautics [1-3]. Compared with the other traditional joints, adhesive joints have advantages of light weight, low cost and easy to process. However, different material properties cause singular stress at the interface end, which may lead to debonding failure in structures [4-12]. The bonded strength can be expressed in terms of the intensity of the singular stress field (ISSF). The ISSF K_σ and the normalized ISSF F_σ can be determined from the interface stress as shown in Eq. (2.1) [13, 14] by using the local polar coordinate (r, θ) indicated in Fig. 2.1 (a), (b).

$$K_\sigma = \lim_{r\to 0}\left[r^{1-\lambda} \times \sigma_\theta(r)\big|_{\theta=\pi/2} \right], \quad F_\sigma = \frac{K_\sigma}{\sigma W^{1-\lambda}} \tag{2.1}$$

Fig. 2.2(a) shows the adhesive joint strength for plate butt joint expressed as the critical remote tensile stress σ_c [15]. It is known that the debonding stress increases with decreasing the adhesive thickness [15-19]. In Ref. [19], the effect of joint component mechanical properties and adhesive layer thickness on stress concentration

was discussed for a bonded cylindrical specimen. In Ref. [7-9] the ISSF is considered under arbitrary material combinations for h/W=0.1 and 0.001. Previous studies have indicated that the normalized ISSF decreases with decreasing the adhesive thickness as shown in Fig. 2.2(b) under tension [7] and under bending [8, 9]. From the critical remote tensile stress shown in Fig. 2.2(a), (b), the critical ISSF can be calculated when the debonding occurs. As shown in Fig. 2.3, the debonding strength can be expressed as a constant value of ISSF [12, 20].

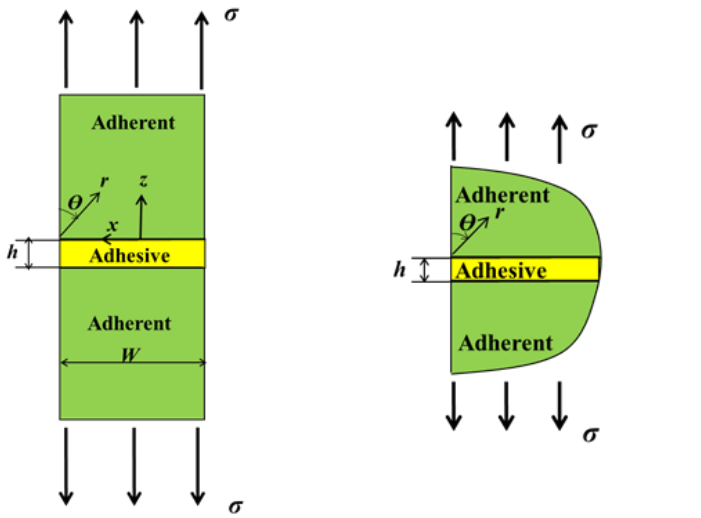

(a) Plate butt joint (b) Semi-infinite butt joint

Fig. 2.1 Adhesive butt joints (Fig. 2.1(b) is equivalent to Fig. 2.1(a) when $h/W \leq 0.01$ in Fig. 2.1(a))

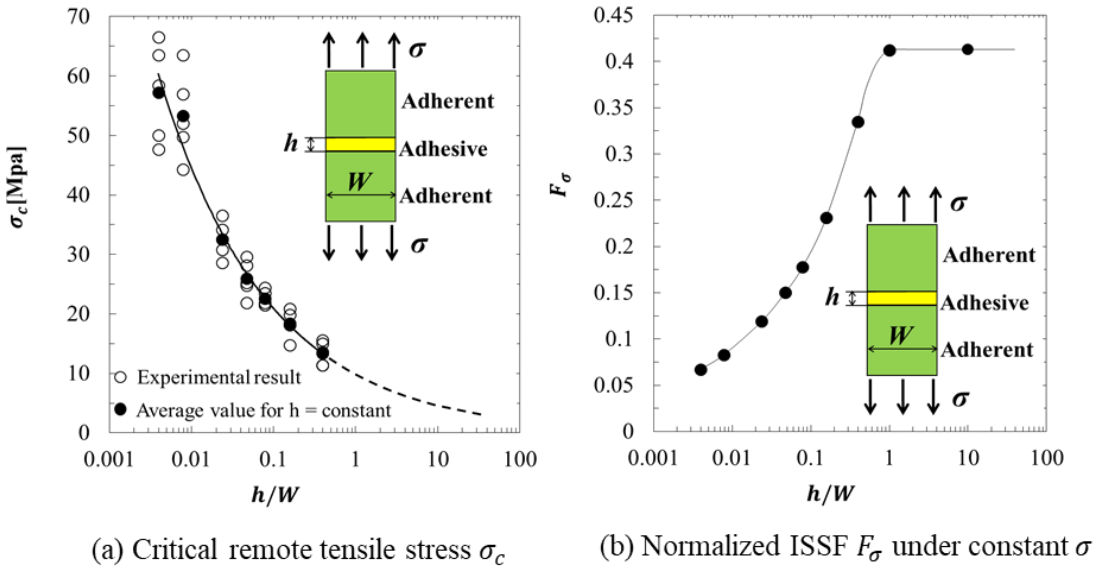

(a) Critical remote tensile stress σ_c (b) Normalized ISSF F_σ under constant σ

Fig. 2.2 Relationship between critical remote tensile stress σ_c, normalized ISSF F_σ and adhesive thickness h

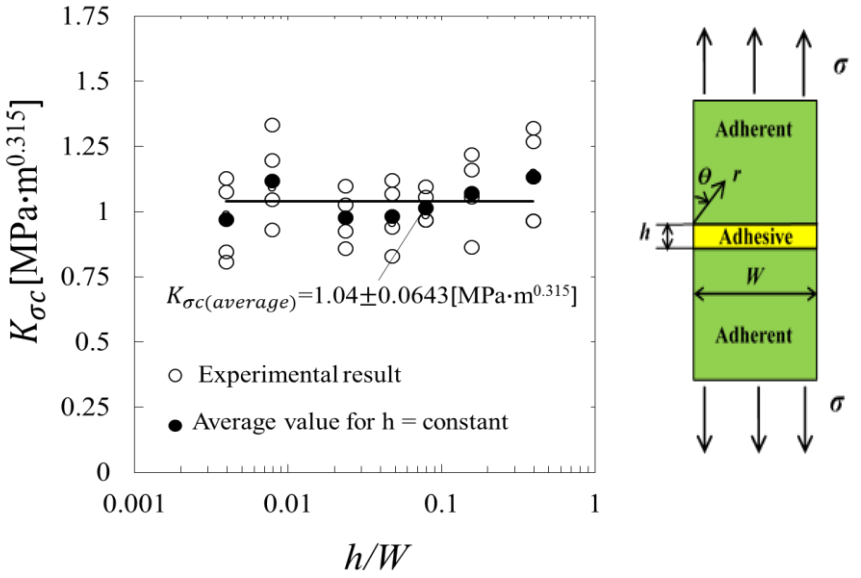

Fig. 2.3 Relationship between $K_{\sigma c}$ and h

From the above discussion, it is seen that the solution for ISSF shown in Fig. 2.2(b) is quite useful for evaluating the adhesive strength. For large adhesive

thickness h, the normalized ISSF F_σ becomes constant as shown in Fig. 2.2(b), and therefore can be estimated easily for any material combination (see Appendix A [14]). However, for small adhesive thickness h, which is necessary for evaluating normal adhesive layers, the normalized ISSF F_σ decreases with decreasing h and does not become constant. In this study, therefore, the ISSF vs. h relation will be clarified mainly focusing on the small adhesive thickness. The aim of this research is to provide the solutions of ISSFs for evaluating the adhesive joint strength. In this study, arbitrary material combinations will be considered for the future use of adhesive joint in wide engineering fields.

2.2 Mesh-independent technique to evaluate the ISSF of plate butt joint

In this section, a mesh-independent technique will be explained for the readers to understand how to obtain accurate ISSFs although similar methods have been used in [9, 12, 20]. Considering a plate butt joint as shown in Fig. 2.1(a) is considered, when the adhesive thickness h is significantly less than the adhesive width W ($h/W \to 0$), the solution may be regarded as a semi-infinite plate butt joint as shown in Fig. 2.1(b). It is known that the interface stress σ_{ij} ($ij=rr, r\theta, \theta\theta$) at the edge can be expressed in the form $\sigma_{ij} \propto 1/r^{1-\lambda}$ when $\alpha(\alpha-2\beta)>0$. Notations α and β denote Dundurs' parameters [21] expressed by Poisson's ratio v and shear modulus G, and notation λ denotes the singular index at the interface expressed as the root of the following equations [22, 23].

$$\left[\sin^2\left(\frac{\pi}{2}\lambda\right)-\lambda^2\right]^2\beta^2+2\lambda^2\left[\sin^2\left(\frac{\pi}{2}\lambda\right)-\lambda^2\right]\alpha\beta+\lambda^2\left[\lambda^2-1\right]\alpha^2+\frac{\sin^2(\lambda\pi)}{4}=0 \qquad (2.2)$$

$$\alpha = \frac{G_1(\kappa_2+1)-G_2(\kappa_1+1)}{G_1(\kappa_2+1)+G_2(\kappa_1+1)} \qquad \beta = \frac{G_1(\kappa_2-1)-G_2(\kappa_1-1)}{G_1(\kappa_2+1)+G_2(\kappa_1+1)} \tag{2.3}$$

$$\kappa_j = \begin{cases} \dfrac{3-\nu_j}{1+\nu_j}\,(plane\ stress) \\ 3-4\nu_j\ (plane\ strain) \end{cases} (j=1,2) \tag{2.4}$$

The singular index λ for different material combinations are shown in Table 2.1.

The ISSF K_σ at the adhesive dissimilar joint end is defined from the real interface stress σ_z^{real} as shown in Eq. (2.5).

$$ISSF\ K_\sigma = \lim_{r\to 0}\left[r^{1-\lambda}\sigma_z^{real}(r)\right],\ \text{but}\ \ ISSF\ K_\sigma \neq \lim_{r\to 0}\left[r^{1-\lambda}\sigma_z^{FEM}(r)\right] \tag{2.5}$$

The ISSF cannot be easily determined by FEM since real interface singular stress σ_z^{real} is different from the FEM stress σ_z^{FEM}, which is largely depending on the mesh size. In the previous papers [8, 9, 12], therefore, the FEM stress ratio $\sigma_z^{FEM} / \sigma_{z(\mathrm{Re}f)}^{FEM}$ was considered by using a reference problem which has been solved very accurately in the previous study. It should be noted that the FEM stress ratio of the unknown and reference problems is independent of the mesh size if the same FEM mesh is applied. This is because the FEM errors of two problems are nearly the same. As the reference solution, a simply bonded plate can be used since the ISSF has been analysed very accurately by using the body force method [14] (see Appendix A). Since the FEM stress ratio and the reference solution are very accurate, the new results also can be obtained very accurately.

Table 2.1 Singular index λ for different material combinations

α	β=-0.4	β=-0.3	β=-0.2	β=-0.1	β=0	β=0.1	β=0.2	β=0.3	β=0.4
-1	0.8073	0.7205	0.6646	0.6247	0.5946				
-0.95	0.8536	0.7576	0.6975	0.6550	0.6232				
-0.9	0.9008	0.7941	0.7295	0.6845	0.6511				
-0.8	1.0000	0.8655	0.7916	0.7415	0.7048				
-0.7	1.1174	0.9348	0.8510	0.7961	0.7564				
-0.6		1.0000	0.9071	0.8480	0.8060	0.7746			
-0.5		1.0558	0.9580	0.8966	0.8532	0.8210			
-0.4		1.0913	1.0000	0.9403	0.8974	0.8655			
-0.3		1.0964	1.0276	0.9761	0.9371	0.9075			
-0.2		1.0756	1.0360	1.0000	0.9699	0.9457	0.9269		
-0.1			1.0251	1.0083	0.9921	0.9777	0.9659		
0			1.0000	1.0000	1.0000	1.0000	1.0000		
0.1			0.9269	0.9777	0.9921	1.0083	1.0251		
0.2			0.9659	0.9457	0.9699	1.0000	1.0360	1.0756	
0.3				0.9075	0.9371	0.9761	1.0276	1.0964	
0.4				0.8655	0.8974	0.9403	1.0000	1.0913	
0.5				0.8210	0.8532	0.8966	0.9580	1.0558	
0.6				0.7746	0.8060	0.8480	0.9071	1.0000	
0.7					0.7564	0.7961	0.8510	0.9348	1.1174
0.8					0.7048	0.7415	0.7916	0.8655	1.0000
0.9					0.6511	0.6845	0.7295	0.7941	0.9008
0.95					0.6232	0.6550	0.6975	0.7576	0.8536
1					0.5946	0.6247	0.6646	0.7205	0.8073

Red: λ<1; Black: λ=1; Green: λ>1

In this study, the ISSF of a simply bonded plate will be used as the reference problem, as is shown in Eq. (2.6).

$$\frac{K_\sigma}{K_{\sigma(\mathrm{Ref.})}} = \lim_{r\to 0}\frac{\left[r^{1-\lambda}\sigma_z^{real}\right]}{\left[r^{1-\lambda}\sigma_{z(\mathrm{Ref.})}^{real}\right]} = \lim_{r\to 0}\frac{\sigma_z^{FEM}}{\sigma_{z(\mathrm{Ref.})}^{FEM}} \tag{2.6}$$

Here, the subscript (Ref.) denotes the ISSF or the stress for reference problem.

The finite element analysis is carried out for the butt joints by using the commercial software ANSYS 16.2. Fig. 2.4(a), (b) show the FEM mesh for the butt joint when h/W=0.001 and the bonded plate (h/W=1). Because of symmetry, quarter models are considered for analysis. The finite-element mesh consists of two-dimensional four-node element named PLANE42 and finer subdivisions are used around the interface end. As shown in Fig. 2.4(b), the same mesh division pattern is used to eliminate FEM error. The total number of elements will be larger if the adhesive layer is thin, even though each case has same mesh division at the interface end. In this work, the total number of elements is 196794 when h/W=0.001, and 5120 when h/W=1. Table 2.2 shows an example of stress ratio for the butt joint over the bonded plate by using the mesh in Fig. 2.4 with different minimum mesh sizes e_{min}. In Table 2.2 it should be noted that $\sigma_z^{mat1}=\sigma_z^{mat2}$, $\tau_{xz}^{mat1}=\tau_{xz}^{mat2}$, but $\sigma_x^{mat1}\neq\sigma_x^{mat2}$, $\sigma_y^{mat1}\neq\sigma_y^{mat2}$ at the interface. Here σ_{ij}^{mat1} denotes the stress for material 1 and σ_{ij}^{mat2} denotes the stress for material 2.

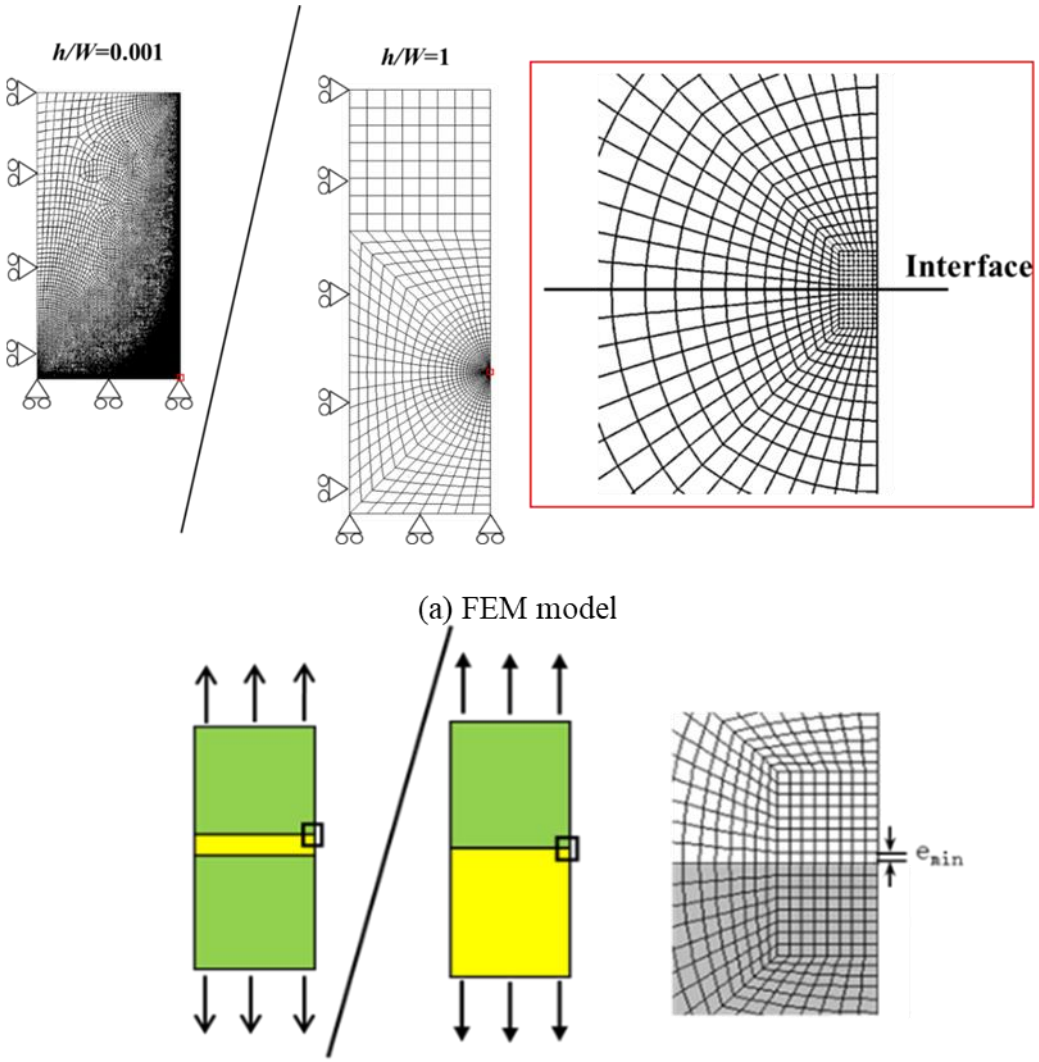

Fig. 2.4 FEM mesh for the plate butt joint (h/W=0.001) and bonded plate (h/W=1)

As shown in Table 2.2, all the stress components ratios $\sigma_{ij}^{P}/\sigma_{ij}^{REF}$ are continuous across the interface and coincide with each other. The results are independent of the element size when the mesh independent technique is employed by using the same FEM mesh pattern.

Table 2.2 Mesh-independent FEM stress ratio $\sigma^P_{ij0,FEM}/\sigma^{REF}_{ij0,FEM}$ when E_1=1000,ν_1=0.23, E_2=105.06,ν_2=0.32,h/W=0.001

	$\sigma^P_{x0,FEM}/\sigma^{REF}_{x0,FEM}$		$\sigma^P_{z0,FEM}/\sigma^{REF}_{z0,FEM}$		$\sigma^P_{y0,FEM}/\sigma^{REF}_{y0,FEM}$		$\tau^P_{xz,FEM}/\tau^{REF}_{xz,FEM}$	
Material	Mat.1	Mat.2	Mat.1	Mat.2	Mat.1	Mat.2	Mat.1	Mat.2
e_{min} =2.5^{-15}	0.3604	0.3603	0.3604		0.3604	0.3604	0.3603	
e_{min} =2.5^{-18}	0.3604	0.3604	0.3604		0.3604	0.3604	0.3603	

2.3 Effect of adhesive thickness on the ISSF for plate butt joint

In the previous papers [7-9, 20] for the plate butt joint as shown in Fig. 2.1(a), the normalized ISSF F^P_σ was defined in Eq. (2.7).

$$F^P_\sigma = K^P_\sigma / \sigma W^{1-\lambda} \tag{2.7}$$

In Eq. (2.7), the ISSF K^P_σ is normalized in terms of the remote tensile stress σ and the plate width W. The ISSF is controlled by the width W. Namely, if W becomes larger, the ISSF becomes larger.

However, if the adhesive thickness h is small, the width W does not affect the ISSF K^P_σ anymore. Considering a small adhesive thickness butt joint as shown in Fig. 2.1(b), the butt joint has two singular points at the two interface ends. If h becomes smaller, the interaction between two interface ends becomes larger. Therefore, the ISSF is controlled by h instead of W, the ISSF K^P_σ should be normalized by h instead of W. In other words, for small h, the butt joint in Fig. 2.1(a) can be regarded in a

semi-infinite plate as shown in Fig. 2.1(b). In this case, the ISSF K_σ^P in Fig. 2.1(b) should be normalized in terms of the remote tensile stress σ and the adhesive thickness h as shown in Eq. (2.8).

$$F_\sigma^{P*} = K_\sigma^P / \sigma h^{1-\lambda} \tag{2.8}$$

Table 2.3 F_σ^P and $F_\sigma^P / F_\sigma^P|_{h/W\to\infty}$ of butt joint with varying adhesive thickness

F_σ^P						
h/W \ (α,β)	(0.3,0)	(0.4,-0.1)	(0.4,0)	(0.4,0.1)	(0.5,-0.1)	(0.5,0)
0.001	0.416	0.152	0.275	0.490	0.095	0.173
0.002	0.435	0.167	0.295	0.511	0.107	0.191
0.005	0.462	0.188	0.324	0.540	0.126	0.219
0.01	0.484	0.208	0.349	0.563	0.144	0.244
0.05	0.545	0.267	0.421	0.627	0.199	0.316
0.1	0.582	0.306	0.464	0.662	0.236	0.361
0.5	0.745	0.538	0.659	0.787	0.473	0.573
1	0.794	0.612	0.716	0.821	0.548	0.633
10	0.796	0.615	0.718	0.822	0.551	0.635
→∞	0.796	0.615	0.718	0.822	0.551	0.635
$F_\sigma^P / F_\sigma^P\|_{h/W\to\infty}$						
h/W \ (α,β)	(0.3,0)	(0.4,-0.1)	(0.4,0)	(0.4,0.1)	(0.5,-0.1)	(0.5,0)
0.001	0.523	0.247	0.383	0.596	0.172	0.272
0.002	0.546	0.272	0.411	0.622	0.194	0.301
0.005	0.580	0.306	0.451	0.657	0.229	0.345
0.01	0.608	0.338	0.486	0.685	0.261	0.384
0.05	0.685	0.434	0.586	0.763	0.361	0.498
0.1	0.731	0.498	0.646	0.805	0.428	0.569
0.5	0.936	0.875	0.918	0.957	0.858	0.902
1	0.997	0.995	0.997	0.999	0.995	0.997
10	1.000	1.000	1.000	1.000	1.000	1.000
→∞	1.000	1.000	1.000	1.000	1.000	1.000

Table 2.3 shows F_σ^P values and normalized values of $F_\sigma^P/F_\sigma^P|_{h/W\to\infty}$ and Fig. 2.5 shows F_σ^P vs. h/W relation for several material combinations. As shown in Table 2.3 and Fig. 2.5, when $h/W \geq 1$, the normalized ISSFs F_σ^P are always the same. This is due

to Saint'-Venant's Principle stating that the effects of two different but statically equivalent loads are the same at sufficiently large distances from load, that is, $h/W \geq 1$. As shown in Table 2.3, the normalized ISSF F_σ^P has the same value in the range $h/W \geq 1$ since the thickness effect can be negligible.

Table 2.4 F_σ^{P*} and $F_\sigma^{P*}/F_\sigma^{P*}|_{h/W\to 0}$ of butt joint with varying adhesive thickness

F_σ^{P*}						
h/W \ (α,β)	(0.3,0)	(0.4,-0.1)	(0.4,0)	(0.4,0.1)	(0.5,-0.1)	(0.5,0)
→0	0.643	0.384	0.558	0.740	0.326	0.476
0.001	0.643	0.384	0.558	0.740	0.326	0.476
0.002	0.643	0.384	0.558	0.740	0.326	0.476
0.005	0.644	0.384	0.558	0.740	0.327	0.477
0.01	0.646	0.386	0.560	0.742	0.328	0.479
0.05	0.658	0.399	0.572	0.750	0.340	0.491
0.1	0.672	0.417	0.588	0.759	0.357	0.507
0.5	0.778	0.590	0.707	0.821	0.536	0.634
1	0.794	0.612	0.716	0.821	0.548	0.633
10	0.689	0.451	0.567	0.716	0.365	0.453
$F_\sigma^{P*}/F_\sigma^{P*}\|_{h/W\to 0}$						
h/W \ (α,β)	(0.3,0)	(0.4,-0.1)	(0.4,0)	(0.4,0.1)	(0.5,-0.1)	(0.5,0)
→0	1.000	1.000	1.000	1.000	1.000	1.000
0.001	1.000	1.000	1.000	1.000	1.000	1.000
0.002	1.000	1.000	1.000	1.000	1.000	1.000
0.005	1.002	1.000	1.000	1.000	1.003	1.002
0.01	1.005	1.005	1.004	1.003	1.006	1.006
0.05	1.023	1.039	1.025	1.014	1.043	1.032
0.1	1.045	1.086	1.054	1.026	1.095	1.065
0.5	1.210	1.536	1.267	1.109	1.644	1.332
1	1.235	1.594	1.283	1.109	1.681	1.330
10	1.072	1.174	1.016	0.968	1.120	0.952

Table 2.4 shows F_σ^{P*} values and Fig. 2.6 shows F_σ^{P*} vs. h/W relation. It is seen that when the adhesive thickness is small, the F_σ^{P*} value becomes constant. The plate butt joint in Fig. 2.1(a) can be regarded in a semi-infinite plate as shown in Fig. 2.1(b) when the relative adhesive thickness $h/W \leq 0.01$. From Fig. 2.5 and Fig. 2.6, it is found that $F_\sigma^{P*}=K_\sigma^P/\sigma h^{1-\lambda}$ is more suitable for small h cases. As shown in Table 2.4, the

normalized ISSF F_σ^{P*} has almost the same value in the range $h/W \leq 0.01$ within 0.6% deviation and in the range $h/W \leq 0.1$ within 10% deviation since the width effect is small.

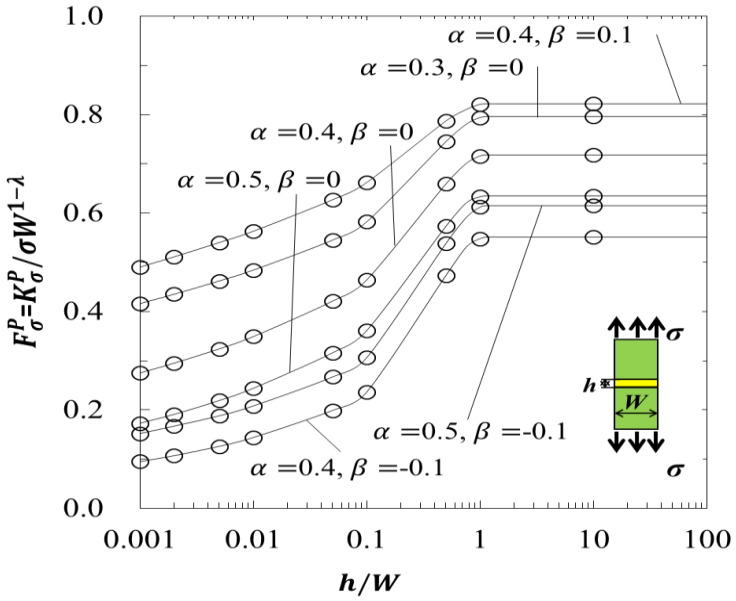

Fig. 2.5. F_σ^P is constant when $h/W \geq 1.0$

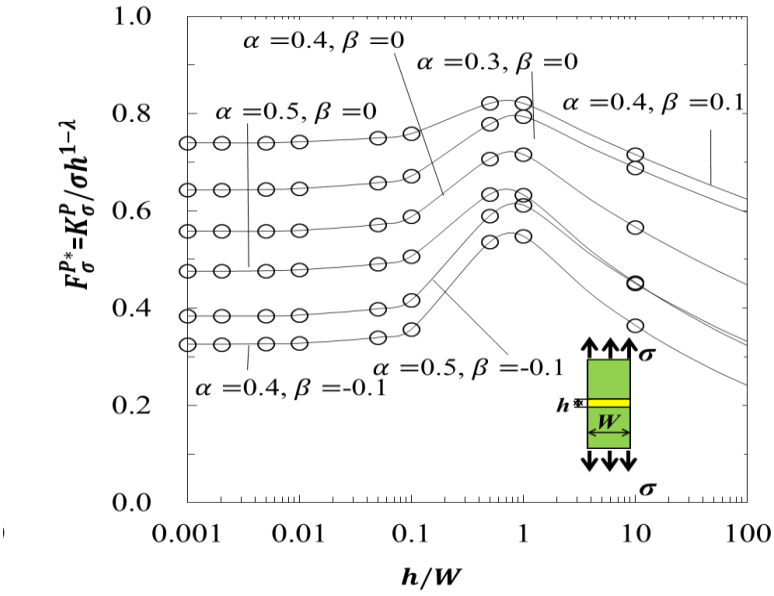

Fig. 2.6. F_σ^{P*} is constant when $h/W \leq 0.01$

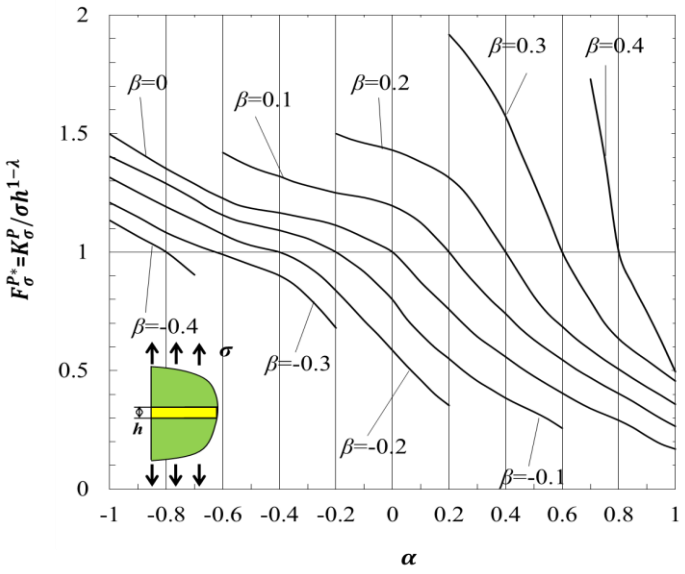

Fig. 2.7 Normalized ISSF F_σ^{P*} of a semi-infinite butt joint in Fig. 2.1(b) ($h/W \leqq 0.01$)

Table 2.5 Normalized ISSF $F_\sigma^{P*} = K_\sigma^P/\sigma h^{1-\lambda}$ of a semi-infinite butt joint in Fig. 2.1(b)

	β=-0.4	β=-0.3	β=-0.2	β=-0.1	β=0	β=0.1	β=0.2	β=0.3	β=0.4
α=-1	1.134	1.209	1.315	1.404	1.498				
α=-0.9	1.066	1.148	1.252	1.347	1.424				
α=-0.8	1.000	1.082	1.191	1.289	1.352				
α=-0.7	0.904	1.032	1.134	1.223	1.288				
α=-0.6		1.000	1.075	1.156	1.227	1.420			
α=-0.5		0.946	1.028	1.119	1.185	1.360			
α=-0.4		0.901	1.000	1.092	1.166	1.320			
α=-0.3		0.812	0.940	1.057	1.142	1.280			
α=-0.2		0.680	0.837	1.000	1.113	1.250	1.500		
α=-0.1			0.710	0.916	1.061	1.230	1.460		
α=0			0.585	0.799	1.000	1.195	1.430		
α=0.1			0.460	0.654	0.873	1.124	1.380		
α=0.2			0.353	0.550	0.758	1.000	1.314	1.918	
α=0.3				0.456	0.643	0.858	1.181	1.769	
α=0.4				0.384	0.558	0.740	1.000	1.572	
α=0.5				0.326	0.476	0.630	0.813	1.293	
α=0.6				0.257	0.405	0.546	0.686	1.000	
α=0.7					0.340	0.470	0.588	0.794	1.730
α=0.8					0.290	0.403	0.506	0.634	1.000
α=0.9					0.223	0.333	0.430	0.543	0.746
α=1					0.169	0.265	0.358	0.456	0.495

Table 2.5 and Fig. 2.7 show the normalized ISSFs F_σ^{P*} under arbitrary material combinations when $h/W \leq 0.01$. Since the solution for bonded plate ($h/W \geq 1$) is indicated in Appendix A, the accurate results can be obtained by the interpolation in the range for $0.01 \leq h/W \leq 1.0$ under arbitrary material combination.

2.4 Experimental evaluation of debonding strength of plate butt join

In this chapter, the adhesively bonded specimens used by Suzuki [15] in Fig. 2.2(a) are analyzed where the adherents S35C are bonded with adhesive epoxy resin. The elastic parameters of the adherent and adhesives are tabulated in Table 2.6. The experimental strength value σ_c is the maximum value of the average axial stress σ_z^∞ obtained by dividing the tensile load by the area of the specimen cross section normal to the load. The load–strain relations are all linear up to the breaking point, which shows that brittle fracture occurred [15]. The fracture was initiated near the adherent surface of either one of the corners of the adhesion plane [15].

Fig. 2.8 shows the experimental tensile adhesive strength with different adhesive thicknesses. The bond strength increases gradually with decreasing adhesive thickness. Fig. 2.9 shows the ISSFs $F_\sigma^P = K_\sigma^P / (\sigma_z^\infty W^{1-\lambda})$ and $F_\sigma^{P*} = K_\sigma^P / (\sigma_z^\infty h^{1-\lambda})$ for the experimental specimens. In Fig. 2.9 F_σ^P and F_σ^{P*} increase with increasing the adhesive thickness. However, F_σ^{P*} is almost constant when h is small. It is seen that F_σ^{P*} can be used conveniently to evaluate the adhesive strength. Fig. 2.10 shows the critical ISSF at $\sigma_z^\infty = \sigma_c$, $K_{\sigma c} = K_\sigma^P \big|_{\sigma_z^\infty = \sigma_c}$. The $K_{\sigma c}$ values are almost constant independent of the adhesive thickness. It can be confirmed that the ISSF can be used for evaluating the debonding strength.

Table 2.6 Material properties of experimental specimens

Combination			Young's modulus E [GPa]	Poisson's ratio ν	α	β	λ
A	Adherent	Medium carbon steel S35C	210	0.30	0.969	0.199	0.685
	Adhesive	Epoxy resin A	3.14	0.37			
B	Adherent	Medium carbon steel S35C	210	0.30	0.978	0.188	0.674
	Adhesive	Epoxy resin B	2.16	0.38			

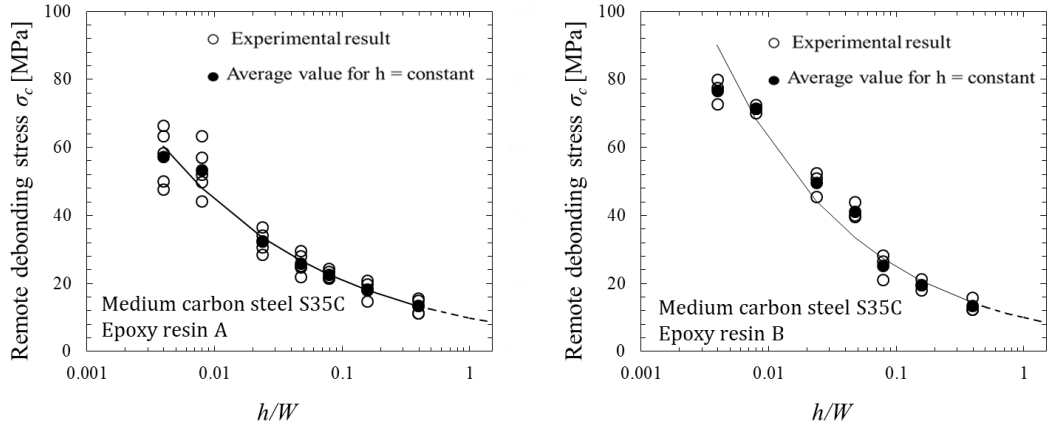

Fig. 2.8 Experimental remote debonding stress σ_c of plate butt joint

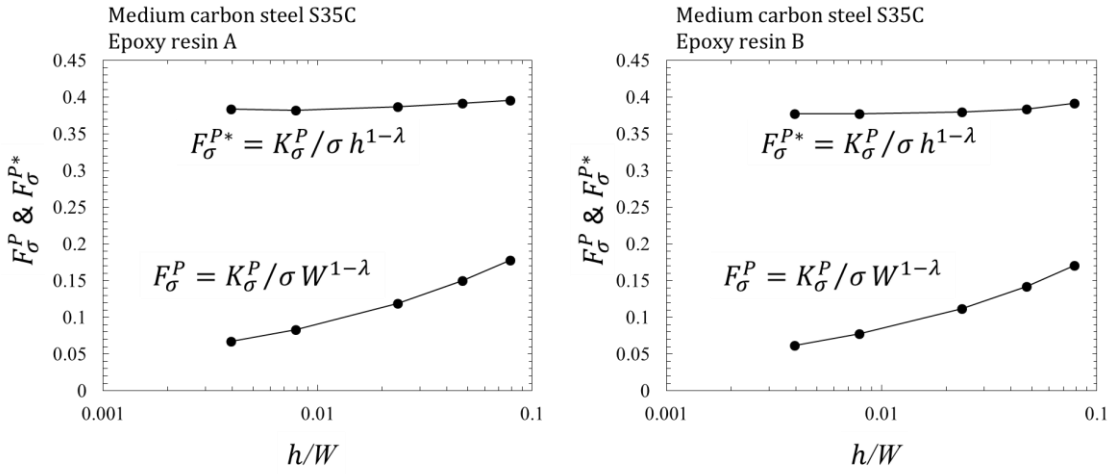

Fig. 2.9 ISSF of experimental specimen

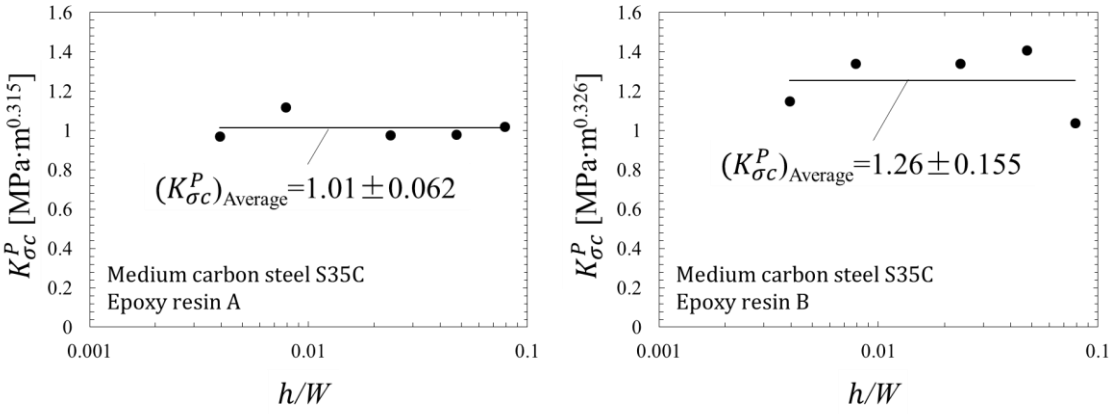

Fig. 2.10 Critical ISSF of experimental specimen

2.5 Conclusion

In this chapter, the ISSF variations were clarified over the entire adhesive thickness range for plate butt joint. An effective mesh-independent technique was applied to obtaining the ISSFs under arbitrary material combinations. The bonded plate, which has been solved by the body force method, was used as the reference solution to eliminate FEM error.

For the plate butt joints, the ISSF $F_{\sigma}^{P*}=K_{\sigma}^{P}/\sigma h^{1-\lambda}$ normalized by adhesive thickness h becomes constant with decreasing adhesive thickness when $h/W\leq 0.01$. In this case, the adhesive joint can be regarded in a semi-infinite plate. If the adhesive layer is thin, F_{σ}^{P*} is more suitable because the variation is smaller than the variation of $F_{\sigma}^{P}=K_{\sigma}^{P}/\sigma W^{1-\lambda}$. To improve the interface strength, thin adhesive layers are desirable.

For a certain value β, it is found that F_{σ}^{P*} decreases with increasing α. Since the solution for case of $h/W\geq 1.0$ was shown in the Appendix A, the accurate results can be obtained by the interpolation also in the range of $0.01\leq h/W\leq 1.0$.

2.6 Reference of Chapter 2

[1] Barnes, T.A., Pashby, I.R., Joining techniques for aluminium spaceframes used in automobiles: part II – adhesive bonding and mechanical fasteners. J. Mater. Process. Technol., 99 (2000), 72-79.

[2] Higgins, A., Adhesive bonding of aircraft structures. Int. J. Adhes. Adhes., 20 (2000), 367-376.

[3] Petrie, E.M., Adhesives for the assembly of aircraft structures and components: decades of performance improvement, with the new applications of the horizon. Metal Finish, 106 (2008), 26-31.

[4] Qian Z, Akisanya, A.R., An experimental investigation of failure initiation in bonded joints. Acta Mater, 46 (1998), 4895-4904.

[5] Akisanya, A.R., Meng C.S., Initiation of fracture at the interface corner of bi-material joints. J Mech Phys Solids, 51 (2003), 27-46.

[6] Mintzas, A, Nowell, D., Validation of an Hcr -based fracture initiation criterion for adhesively bonded joints. Eng Fract Mech, 80 (2012), 13-27.

[7] Zhang, Y., Noda, N.A., Takaishi, K.T., Lan, X., Effect of Adhesive Thickness on the Interface of Singular Stress at the Adhesive Dissimilar Joint. Trans. JSME. A., 77 (2011), 360-372.

[8] Zhang, Y., Noda, N.A, Wu, P.Z, Duan, M.L., A Mesh-Independent Technique to Evaluate Stress Singularities in Adhesive Joints, Int. J. Adhes. Adhes., 57 (2015), 105-117.

[9] Zhang, Y., Noda, N.A., Wu, P. and Duan, M., Corrigendum to "A mesh-independent technique to evaluate stress singularities in adhesive joints". Int. J. Adhes. Adhes., 60 (2015), 130.

[10] Miyazaki, T., Noda, N.A., Li, R., Uchikoba, T., Sano, Y., Debonding criterion for single lap joints from the intensity of singular stress field. Transactions of The Japan Institute of Electronics Packaging, 16 (2013), 143-151. [in Japanese].

[11] Miyazaki, T., Noda N.A., Uchikoba, T., Li, R., Sano, Y., Proposal of a convenient and accurate method for evaluation of debonding strength. Trans. Soc. Autom. Eng. Jpn., 45 (2014), 895-901. [in Japanese].

[12] Noda, N.A., Miyazaki, T., Li, R., Uchikoba, T., Sano, Y., Takase, Y., Debonding Strength Evaluation in Terms of the Intensity of Singular Stress at the corner with and without fictitious crack, Int. J. Adhes. Adhes., 61 (2015), 46-64.

[13] Chen, D.H., Nisitani, H., Intensity of singular stress field near the interface edge point of a bonded strip. Trans. JSME., 59 (1993), 2682-2686.

[14] Noda, N.A, Shirao, R., Li, J., Sugimoto, J.S., Intensity of Singular Stress at the End of a Fiber under Pull-out Force, International Journal of Solids and Structures, 44 (2007), 4472-4491.

[15] Suzuki, Y., Adhesive Tensile Strengths of Scarf and Butt Joints of Steel Plates, Trans. JSME. A., 53 (1987), 514-522.

[16] Arenas, J., Narbon, J.J., Alia, C., Optimum adhesive thickness in structural adhesives joints using statistical techniques based on Weibull distribution, Int. J. Adhes. Adhes., 30 (2010), 160-165.

[17] Afendi, M., Teramoto, T., Bakri, H.B., Strength prediction of epoxy adhesively bonded scarf joints of dissimilar adherends, Int. J. Adhes. Adhes., 31 (2011), 402-411.

[18] Hunston, D., Miyagi, Z., Schultheisz, C., Zaghi, S., The sandwich bending specimen for characterizing adhesive properties, Mechanics of Time-Dependent Materials, 7 (2003), 71-88.

[19] Neves, A.A., Courinho, E., Poitevin, A., Influence of joint component mechanical properties and adhesive layer thickness on stress distribution in micro-tensile bond strength specimens, Dental Materials, 25 (2009), 4-12.

[20] Noda, N.A., Miyazaki, T., Uchikoba, T., Li, R., Sano, Y., Takase, Y., Convenient Debonding Strength Evaluation Based on the Intensity of Singular Stress for Adhesive Joints. Transactions of the Japan Institute of Electronics Packaging, 17 (2014), 132-142 (in Japanese).

[21] Dundurs, J., Discussion of edge-bonded dissimilar orthotropic elastic wedges under normal and shear loading. J. Appl. Mech., 36 (1969), 650-652.

[22] Bogy, D.B., Edge-Bonded Dissimilar Orthogonal Elastic Wedges under Normal and Shear Loading, J. Appl. Mech., 35 (1968), 460-466.

[23] Bogy, D.B., Two Edge-Bonded Elastic Wedges of Different and Wedge Angles under Surface Tractions, J. Appl. Mech., 38 (1971), 377-386.

Chapter 3 Analysis on intensity of singular stress for cylindrical butt joint in comparison with plate butt joint

3.1 Introduction

The intensity of singular stress for plate butt joint (Fig. 3.1(a)) under arbitrary material combinations has been investigated in Chapter 2. Thus in this chapter, the intensity of singular stress for the axi-symmetrical problem, cylindrical butt joint (Fig. 3.1(b)), will be considered as well in comparison with plate butt joint (Fig. 3.1(a)).

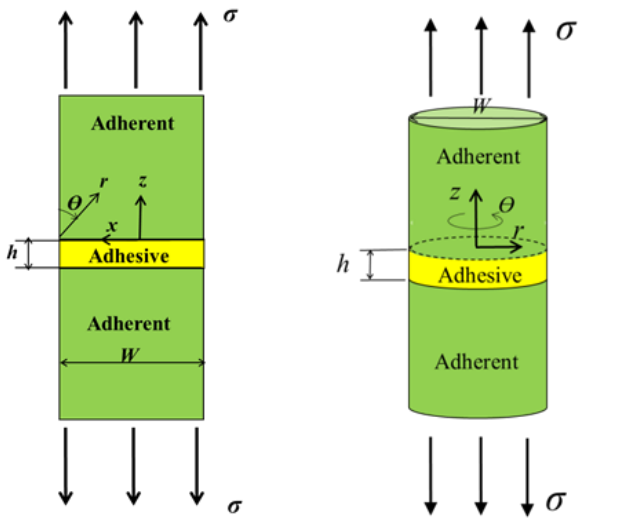

(a) Plate butt joint (b) Cylinder butt joint

Fig. 3.1 Plate and cylindrical butt joints

In this chapter, the intensity of singular stress on the interface outer edge (interface end) of cylindrical butt joint will be investigated, the difference between cylindrical butt joint and plate butt joint will be discussed.

3.2 Mesh-independent technique to evaluate the ISSF of cylindrical butt joint

In this section, the mesh-independent technique will be explained for the readers to understand how to obtain accurate ISSFs for cylindrical butt joints although the similar method was used to analyze bonded cylinder and bonded pipe in Ref [1]. The ISSF of a semi-infinite butt joint K_σ^P has been analyzed in the previous chapter. To obtain the ISSF of cylindrical butt joint K_σ^C, K_σ^P can be used as the reference solution. Table 3.1 shows an example of stress ratio for the cylindrical butt joint in Fig. 3.1(b) over the plate butt joint in Fig. 3.1(a). Different from Table 2.2, the ratios of stress components are not always consistent with each other even though the same FE mesh is applied. It should be noted that the value of $\sigma_{\theta 0,FEM}^C/\sigma_{y0,FEM}^P$ is quite different from the other stress ratios. Therefore, we have to consider the mesh-independent technique for axial-symmetric problems in some special aspects.

Table 3.1 Ratio of $\sigma_{ij0,FEM}^C/\sigma_{ij0,FEM}^P$ (E_1=1000,ν_1=0.23, E_2=105.06,ν_2=0.32,h/W=0.001)

	$\sigma_{r0,FEM}^C/\sigma_{x0,FEM}^P$		$\sigma_{z0,FEM}^C/\sigma_{z0,FEM}^P$		$\sigma_{\theta 0,FEM}^C/\sigma_{y0,FEM}^P$		$\tau_{rz,FEM}^C/\tau_{xz,FEM}^P$	
Material	Mat. 1	Mat. 2	Mat. 1	Mat. 2	Mat. 1	Mat. 2	Mat. 1	Mat. 2
$e_{\min}$ =2.5^{-15}	0.9937	0.9937	0.9955		0.5679	0.9745	0.9937	
e_{min} =2.5^{-18}	0.9937	0.9937	0.9949		0.7187	0.9813	0.9937	

The difference between Table 2.2 and Table 3.1 can be explained in the following way. For the plane strain problem as shown in Fig. 3.1(a), the strain in the *y*

direction is zero. While for the axi-symmetrical problem as shown in Fig. 3.1(b), the strain in the θ direction on the outer cylinder surface is expressed as $\varepsilon_\theta=u_r/(W/2)$ [2], which can lead to non-zero stresses [1, 3]. Then the stress of the unknown problem shown in Fig. 3.1(b) should be expressed as:

$$\sigma_j^C=\frac{K_{\sigma_j}^C}{R^{1-\lambda}}+\tilde{\sigma}_j^C=\hat{\sigma}_j^C+\tilde{\sigma}_j^C\ (j=r,z,\theta),\quad \tau_{rz}^C=\frac{K_{\tau_{xy}}^C}{R^{1-\lambda}}+\tilde{\tau}_{rz}^C=\hat{\tau}_{rz}^C+\tilde{\tau}_{rz}^C. \tag{3.1}$$

where R is the local distance from the axisymmetrical interface end.

In Eq. (3.1), the first terms $\hat{\sigma}_j^C$ and $\hat{\sigma}_{rz}^C$ denote singular stress and the second terms $\tilde{\sigma}_j^C$ and $\tilde{\tau}_{rz}^C$ denote non-singular stress [3-5] as

$$\left(\tilde{\sigma}_{r0}^C\right)^{\text{mat1}},\left(\tilde{\sigma}_{z0}^C\right)^{\text{mat1}},\left(\tilde{\sigma}_{\theta0}^C\right)^{\text{mat1}},\left(\tilde{\tau}_{rz}^C\right)^{\text{mat1}}\ \text{ in material 1;}$$

$$\left(\tilde{\sigma}_{r0}^C\right)^{\text{mat2}},\left(\tilde{\sigma}_{z0}^C\right)^{\text{mat2}},\left(\tilde{\sigma}_{\theta0}^C\right)^{\text{mat2}},\left(\tilde{\tau}_{rz}^C\right)^{\text{mat2}}\ \text{ in material 2.}$$

These eight stress components should satisfy the boundary conditions for bonded interface and free edge of the outer surface as well as the compatibility condition. As a result, they are reduced to the following equations.

$$\left(\tilde{\sigma}_{r0}^C\right)^{\text{mat1}}=\left(\tilde{\sigma}_{r0}^C\right)^{\text{mat2}}=\left(\tilde{\tau}_{rz}^C\right)^{\text{mat1}}=\left(\tilde{\tau}_{rz}^C\right)^{\text{mat2}}=0 \tag{3.2}$$

$$\left(\tilde{\sigma}_{z0}^C\right)^{\text{mat1}}=\left(\tilde{\sigma}_{z0}^C\right)^{\text{mat2}}=\tilde{\sigma}_{z0}^C \tag{3.3}$$

$$\left(\tilde{\varepsilon}_{\theta0}^C\right)^{\text{mat1}}=\left(\tilde{\varepsilon}_{\theta0}^C\right)^{\text{mat2}}=\tilde{\varepsilon}_{\theta0}^C \tag{3.4}$$

$$\left(\tilde{\varepsilon}_{r0}^C\right)^{\text{mat1}}=\left(\tilde{\varepsilon}_{r0}^C\right)^{\text{mat2}}=\tilde{\varepsilon}_{r0}^C \tag{3.5}$$

By substituting Eqs. (3.2), (3.3) into Eq. (3.4), we have

$$\left(\tilde{\varepsilon}_{\theta 0}^{C}\right)^{\text{mat1}}-\left(\tilde{\varepsilon}_{\theta 0}^{C}\right)^{\text{mat2}}=\frac{1}{E_1}\left[\left(\tilde{\sigma}_{\theta 0}^{C}\right)^{\text{mat1}}-\nu_1\left(\tilde{\sigma}_{z0}^{C}\right)^{\text{mat1}}\right]-\frac{1}{E_2}\left[\left(\tilde{\sigma}_{\theta 0}^{C}\right)^{\text{mat2}}-\nu_2\left(\tilde{\sigma}_{z0}^{C}\right)^{\text{mat2}}\right]=0.$$

Thus

$$\left(\frac{\nu_1}{E_1}-\frac{\nu_2}{E_2}\right)\tilde{\sigma}_{z0}^{C}=\frac{\left(\tilde{\varepsilon}_{\theta 0}^{C}\right)^{\text{mat1}}}{E_1}-\frac{\left(\tilde{\varepsilon}_{\theta 0}^{C}\right)^{\text{mat2}}}{E_2} \tag{3.6}$$

Similarly, for Eq. (3.5), we have

$$\left(\tilde{\varepsilon}_{r0}^{C}\right)^{\text{mat1}}-\left(\tilde{\varepsilon}_{r0}^{C}\right)^{\text{mat2}}=\frac{1}{E_1}\left[\left(\tilde{\sigma}_{r0}^{C}\right)^{\text{mat1}}-\nu_1\left(\tilde{\sigma}_{z0}^{C}\right)^{\text{mat1}}\right]-\frac{1}{E_2}\left[\left(\tilde{\sigma}_{\theta 0}^{C}\right)^{\text{mat2}}-\nu_2\left(\tilde{\sigma}_{z0}^{C}\right)^{\text{mat2}}\right]=0.$$

Substitute Eq. (3.6) into the above equation, we have

$$\frac{\left(\tilde{\sigma}_{\theta 0}^{C}\right)^{\text{mat1}}}{\left(\tilde{\sigma}_{\theta 0}^{C}\right)^{\text{mat2}}}=\frac{1+\nu_2}{1+\nu_1}\cdot\frac{E_1}{E_2}. \tag{3.7}$$

From Eq. (3.6) and Eq. (3.7) we can obtain

$$\frac{\left(\tilde{\sigma}_{\theta 0}^{C}\right)^{\text{mat1}}}{\tilde{\sigma}_{z0}^{C}}=-\frac{\nu_1-\dfrac{E_1}{E_2}\nu_2}{\dfrac{\nu_1-\nu_2}{1+\nu_2}}. \tag{3.8}$$

And

$$\frac{\left(\tilde{\sigma}_{\theta 0}^{C}\right)^{\text{mat2}}}{\tilde{\sigma}_{z0}^{C}}=-\frac{\nu_2-\frac{E_2}{E_1}\nu_1}{\frac{\nu_2-\nu_1}{1+\nu_2}}. \tag{3.9}$$

For axis symmetric problem under cylindrical coordinate system, there is

$$\begin{cases}\varepsilon_r=\dfrac{\partial u_r}{\partial r}\\ \varepsilon_\theta=\dfrac{u_r}{r}\\ \gamma_{rz}=\dfrac{\partial u_r}{\partial z}+\dfrac{\partial u_z}{\partial r}\end{cases} \tag{3.10}$$

Recall Eq. (3.4) we can obtain:

$$\begin{aligned}&\left(\tilde{\varepsilon}_{\theta 0}^{C}\right)^{\text{mat1}}=\left(\tilde{\varepsilon}_{\theta 0}^{C}\right)^{\text{mat2}}=\tilde{\varepsilon}_{\theta 0}^{C}=\varepsilon_\theta=\frac{u_r}{r}\\ &=\frac{1}{E_1}\left\{\left(\tilde{\sigma}_{\theta 0}^{C}\right)^{\text{mat1}}-\nu_1\left[\left(\tilde{\sigma}_{r0}^{C}\right)^{\text{mat1}}+\left(\tilde{\sigma}_{z0}^{C}\right)^{\text{mat1}}\right]\right\}\\ &=-\frac{\left(1+\nu_1\right)\nu_1E_2-\left(1+\nu_2\right)\nu_2E_1}{\left(\nu_1-\nu_2\right)E_1E_2}\tilde{\sigma}_{z0}^{C}\end{aligned}$$

Thus

$$\begin{aligned}&\left(\tilde{\sigma}_{z0}^{C}\right)^{\text{mat1}}=\left(\tilde{\sigma}_{z0}^{C}\right)^{\text{mat2}}=\tilde{\sigma}_{z0}^{C}\\ &=-\frac{\left(\nu_1-\nu_2\right)E_1E_2}{\left(1+\nu_1\right)\nu_1E_2-\left(1+\nu_2\right)\nu_2E_1}\frac{u_r}{r}\\ &=-\frac{\left(\nu_1-\nu_2\right)E_1E_2}{\left(1+\nu_1\right)\nu_1E_2-\left(1+\nu_2\right)\nu_2E_1}\frac{u_{r0}^{C}}{(W/2)}\end{aligned} \tag{3.11}$$

Substituting Eq. (3.11) into Eqs. (3.8), (3.9) gives

$$\left(\tilde{\sigma}_{\theta 0}^{C}\right)^{\text{mat1}} = \frac{\left(1+\nu_2\right)\left(\nu_1 E_2 - \nu_2 E_1\right)E_1}{\left(1+\nu_1\right)\nu_1 E_2 - \left(1+\nu_2\right)\nu_2 E_1}\frac{u_{r0}^{C}}{(W/2)} \tag{3.12}$$

$$\left(\tilde{\sigma}_{\theta 0}^{C}\right)^{\text{mat2}} = \frac{\left(1+\nu_1\right)\left(\nu_1 E_2 - \nu_2 E_1\right)E_2}{\left(1+\nu_1\right)\nu_1 E_2 - \left(1+\nu_2\right)\nu_2 E_1}\frac{u_{r0}^{C}}{(W/2)} \tag{3.13}$$

And recall Eq. (3.2)

$$\left(\tilde{\sigma}_{r0}^{C}\right)^{\text{mat1}} = \left(\tilde{\sigma}_{r0}^{C}\right)^{\text{mat2}} = \left(\tilde{\tau}_{rz}^{C}\right)^{\text{mat1}} = \left(\tilde{\tau}_{rz}^{C}\right)^{\text{mat2}} = 0 \tag{3.14}$$

The validity of Eqs. (3.11)-(3.14) to express non-singular stress components will be discussed in Tables 3.2, 3.3, 3.4. By using the material combination shown in Table 3.1, Table 3.2 shows the radial displacement at the interface end, u_{r0}^{C}, and the non-singular stresses which are obtained from Eqs. (3.11), (3.12), (3.13) and (3.14). Here, displacement u_{r0}^{C} is independent of the element size. Table 3.3 shows the singular stresses by subtracting the non-singular stresses in Table 3.2 from the stresses at the interface end. Table 4.4 shows the ratios of the singular stresses at the interface end of cylindrical butt joint to those of plate butt joint. It is found that the ratio 0.9937 is independent of the element size $e_{\min}$. Since the ratios of singular stress components are consistent with each other, the validity of Eqs. (3.11)-(3.14) is confirmed. From the comparison between Table 3.1 and Table 3.4, it is seen that $\sigma_{r0,FEM}^{C}$ and $\tau_{rz,FEM}^{C}$ do not have the non-singular stresses because $\tilde{\sigma}_{r0,FEM}^{C} = \tilde{\tau}_{rz0,FEM}^{C} = 0$. The correct ISSF ratio can be calculated from $\sigma_{r0,FEM}^{C}$ and $\tau_{rz,FEM}^{C}$ easily since the subtraction process is not necessary.

Table 3.2 Non-singular stresses of cylindrical butt joint

e_{min}	$\tilde{\sigma}^C_{r0,FEM}$		$\tilde{\sigma}^C_{z0,FEM}$		$\tilde{\sigma}^C_{\theta 0,FEM}$		$\tilde{\tau}^C_{rz0,FEM}$		u^C_{r0}
	Mat.1	Mat.2	Mat.1	Mat.2	Mat.1	Mat.2	Mat.1	Mat.2	
2.5^{-15}	0.0000	0.0000	0.0065		-0.2616	-0.0255	0.0000		-0.00013153
2.5^{-18}	0.0000	0.0000	0.0065		-0.2616	-0.0255	0.0000		-0.00013154

Table 3.3 Singular stresses of cylindrical butt joint

e_{min}	$\sigma^C_{r0,FEM} - \tilde{\sigma}^C_{r0,FEM}$		$\sigma^C_{z0,FEM} - \tilde{\sigma}^C_{z0,FEM}$		$\sigma^C_{\theta 0,FEM} - \tilde{\sigma}^C_{\theta 0,FEM}$		$\tau^C_{rz0,FEM} - \tilde{\tau}^C_{rz0,FEM}$	
	Mat.1	Mat.2	Mat.1	Mat.2	Mat.1	Mat.2	Mat.1	Mat.2
2.5^{-15}	-1.5377	0.9911	4.1917		0.6104	1.3238	0.2144	
2.5^{-18}	-2.3816	1.5356	6.4919		0.9454	2.0503	0.3323	

Table 3.4 The ratios of singular stresses at the interface end of the cylindrical butt joint and the plate butt joint

e_{min}	$\dfrac{\sigma^C_{r0,FEM} - \tilde{\sigma}^C_{r0,FEM}}{\sigma^P_{x0,FEM}}$		$\dfrac{\sigma^C_{z0,FEM} - \tilde{\sigma}^C_{z0,FEM}}{\sigma^P_{z0,FEM}}$		$\dfrac{\sigma^C_{\theta 0,FEM} - \tilde{\sigma}^C_{\theta 0,FEM}}{\sigma^P_{y0,FEM}}$		$\dfrac{\tau^C_{rz0,FEM} - \tilde{\tau}^C_{rz0,FEM}}{\tau^P_{xz0,FEM}}$	
	Mat.1	Mat.2	Mat.1	Mat.2	Mat.1	Mat.2	Mat.1	Mat.2
2.5^{-15}	0.9937	0.9937	0.9937		0.9937	0.9937	0.9937	
2.5^{-18}	0.9937	0.9937	0.9937		0.9937	0.9937	0.9937	

3.3 Difference of singularity between cylindrical butt joint and plate butt joint

For plane stress and plane strain problems, Dundurs' parameters (α, β) fully control the solution and results. Under fixed (α, β), therefore, the ISSFs are always the same for plane problems. However, since the cylindrical butt joint is axi-symmetrical, (α, β) cannot totally control the ISSFs.

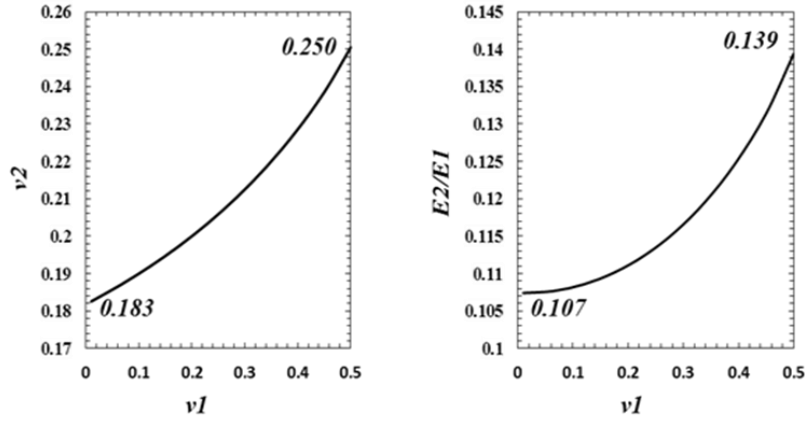

(a) (b)

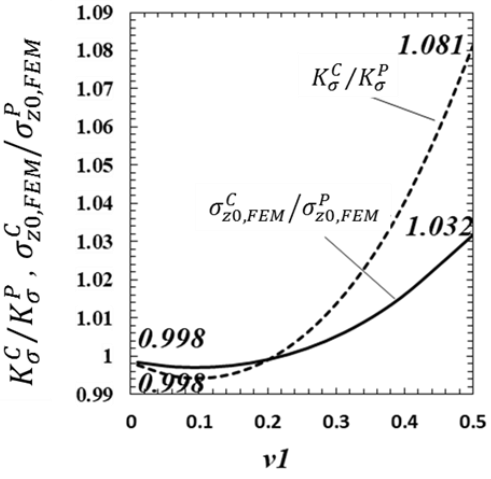

(c)

Fig. 3.2 (a) v_2, (b) E_2/E_1, (c) K_σ^C/K_σ^P and $\sigma_{z0,FEM}^C/\sigma_{z0,FEM}^P$ values depending on v_1 under fixed (α, β) = (0.8, 0.3)

Fig. 3.2 shows an example when (α, β) = (0.8, 0.3). Fig. 3.2(a) and Fig. 3.2(b) show the possible material combinations under (α, β) = (0.8, 0.3). Here, ν_2 and E_2/E_1 are calculated with varying ν_1 from 0 to 0.5. It can be seen that ν_2 changes from 0.183 to 0.250, and E_2/E_1 changes from 0.107 to 0.139. Fig. 3.2(c) shows $K_\sigma^C/K_\sigma^P=[\sigma_{z0,FEM}^C-\tilde{\sigma}_{z0,FEM}^C]/\sigma_{z0,FEM}^P$ and $\sigma_{z0,FEM}^C/\sigma_{z0,FEM}^P$ calculated with varying ν_1 from 0 to 0.5. It is seen that K_σ^C/K_σ^P changes from 0.998 to 1.081, and $\sigma_{z0,FEM}^C/\sigma_{z0,FEM}^P$ changes from 0.998 to 1.032. Different from plane problems, K_σ^C/K_σ^P and $\sigma_{z0,FEM}^C/\sigma_{z0,FEM}^P$ are not constants under fixed (α, β). Therefore, in this study the maximum and minimum values will be focused to evaluate the strength of cylindrical butt joint.

3.4 Effect of adhesive thickness on the ISSF for cylindrical butt joint

For several material combinations, Table 3.5 shows normalized ISSF F_σ^C defined in Eq. (3.15). And Fig. 3.3 shows F_σ^C vs. h/W relation.

$$F_\sigma^C=K_\sigma^C/\sigma W^{1-\lambda}. \tag{3.15}$$

As shown in Fig. 3.3 when adhesive thickness h is large, the normalized ISSF F_σ^C always becomes constant. In Table 3.5, the normalized ISSF F_σ^C has the same value in the range $h/W\geq 1$ since the thickness effect can be negligible.

Table 3.6 shows normalized ISSF F_σ^{C*} values defined in Eq. (3.16). And Fig.3.4 shows F_σ^{C*} vs. h/W relation.

$$F_\sigma^{C*}=K_\sigma^C/\sigma h^{1-\lambda}. \tag{3.16}$$

Table 3.5 F_σ^C and $F_\sigma^C/F_\sigma^C|_{h/W\to\infty}$ of cylindrical butt joint by varying adhesive thickness

F_σ^C				
Mat / *h/W*	E_1=1000 ν_1=0.23 E_2=535.963 ν_2=0.239	E_1=1000 ν_1=0.23 E_2=339.392 ν_2=0.189	E_1=1000 ν_1=0.23 E_2=413.754 ν_2=0.293	E_1=1000 ν_1=0.23 E_2=312.891 ν_2=0.333
0.001	0.722	0.623	0.478	0.302
0.002	0.734	0.642	0.498	0.324
0.005	0.750	0.667	0.526	0.357
0.01	0.763	0.688	0.549	0.384
0.05	0.798	0.743	0.610	0.459
0.1	0.819	0.774	0.645	0.504
0.5	0.890	0.860	0.762	0.650
1	0.901	0.871	0.779	0.669
10	0.901	0.871	0.779	0.669
→∞	0.901	0.871	0.779	0.669
$F_\sigma^C/F_\sigma^C\|_{h/W\to\infty}$				
Mat / *h/W*	E_1=1000 ν_1=0.23 E_2=535.963 ν_2=0.239	E_1=1000 ν_1=0.23 E_2=339.392 ν_2=0.189	E_1=1000 ν_1=0.23 E_2=413.754 ν_2=0.293	E_1=1000 ν_1=0.23 E_2=312.891 ν_2=0.333
0.001	0.801	0.715	0.614	0.451
0.002	0.815	0.737	0.639	0.484
0.005	0.832	0.766	0.675	0.534
0.01	0.847	0.790	0.705	0.574
0.05	0.886	0.853	0.783	0.686
0.1	0.909	0.889	0.828	0.753
0.5	0.988	0.987	0.978	0.972
1	1.000	1.000	1.000	1.000
10	1.000	1.000	1.000	1.000
→∞	1.000	1.000	1.000	1.000

Table 3.6 F_σ^{C*} and $F_\sigma^{C*}/F_\sigma^{C*}|_{h/W\to 0}$ of cylindrical butt joint with varying adhesive thickness

F_σ^C				
Mat / *h/W*	E_1=1000 ν_1=0.23 E_2=535.963 ν_2=0.239	E_1=1000 ν_1=0.23 E_2=339.392 ν_2=0.189	E_1=1000 ν_1=0.23 E_2=413.754 ν_2=0.293	E_1=1000 ν_1=0.23 E_2=312.891 ν_2=0.333
→0	0.851	0.833	0.722	0.616
0.001	0.851	0.833	0.722	0.616
0.002	0.851	0.833	0.722	0.616
0.005	0.851	0.834	0.722	0.617
0.01	0.852	0.835	0.723	0.618
0.05	0.857	0.843	0.729	0.626
0.1	0.866	0.852	0.741	0.639
0.5	0.905	0.886	0.794	0.699
1	0.901	0.871	0.779	0.669
10	0.853	0.790	0.678	0.527
$F_\sigma^{C*}/F_\sigma^{C*}\|_{h/W\to 0}$				
Mat / *h/W*	E_1=1000 ν_1=0.23 E_2=535.963 ν_2=0.239	E_1=1000 ν_1=0.23 E_2=339.392 ν_2=0.189	E_1=1000 ν_1=0.23 E_2=413.754 ν_2=0.293	E_1=1000 ν_1=0.23 E_2=312.891 ν_2=0.333
→0	1.000	1.000	1.000	1.000
0.001	1.000	1.000	1.000	1.000
0.002	1.000	1.000	1.000	1.000
0.005	1.000	1.001	1.000	1.002
0.01	1.001	1.002	1.001	1.003
0.05	1.007	1.012	1.010	1.016
0.1	1.018	1.023	1.026	1.037
0.5	1.063	1.064	1.100	1.135
1	1.059	1.046	1.079	1.086
10	1.002	0.948	0.939	0.856

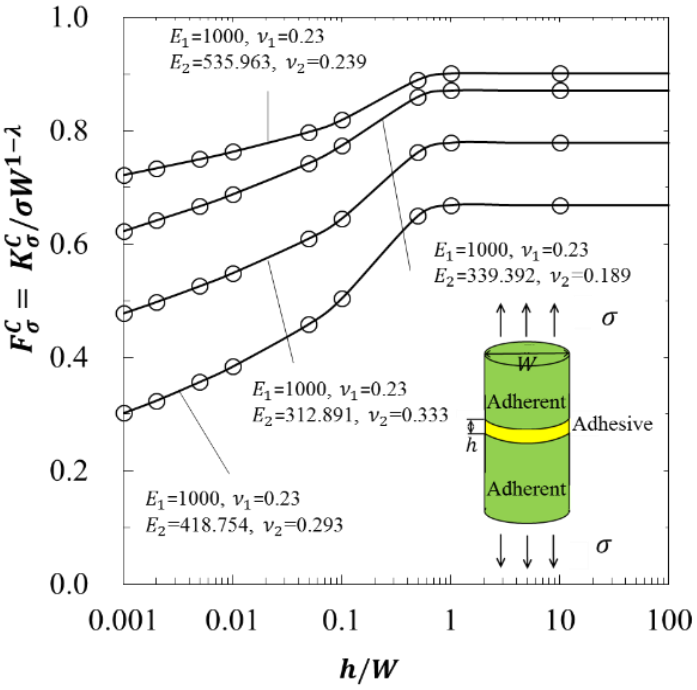

Fig. 3.3 F_σ^C is constant when $h/W \geq 1.0$

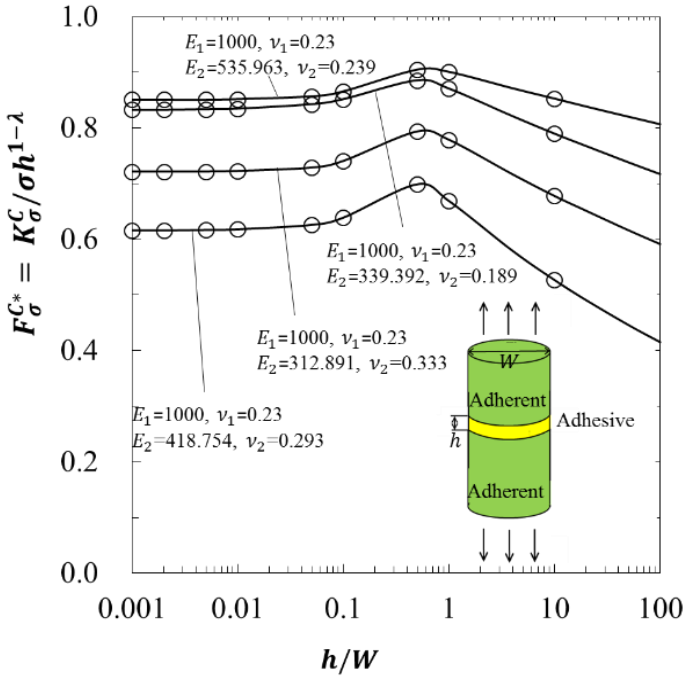

Fig. 3.4 F_σ^{C*} is constant when $h/W \leq 0.01$

It is seen that when the adhesive thickness is small, the F_σ^{C*} value always becomes constant. From Fig. 3.3 and Fig. 3.4, it is found that $F_\sigma^{C*}=K_\sigma^C/\sigma h^{1-\lambda}$ is suitable for evaluating the adhesive strength when adhesive layer is thin. As shown in Table 3.6, the normalized ISSF F_σ^{C*} has almost the same value in the range $h/W \leq 0.01$ within 0.3% deviation and in the range $h/W \leq 0.1$ within 4% deviation since the width effect is small.

3.5 Discussion of suitable prediction for debonding strength

Fig. 3.5 and Fig. 3.6 show the maximum values of K_σ^C/K_σ^P and the $\sigma_{z0,FEM}^C/\sigma_{z0,FEM}^P$ by varying α from -0.2 to 1.0 when β = 0.2 and β = 0.3. Those values were calculated in a similar way as shown in Fig. 3.2. For the bad pair $\alpha(\alpha-2\beta)>0$, the solid line indicates the ISSF ratio K_σ^C/K_σ^P and the broken line indicates the stress ratio $\sigma_{z0,FEM}^C/\sigma_{z0,FEM}^P$. For $\alpha(\alpha-2\beta)>0$, the singular stress appears at the interface end, and therefore K_σ^C/K_σ^P may be useful for evaluating the debonding strength. For the good pair $\alpha(\alpha-2\beta)<0$, the solid line indicates the stress ratio $\left(\sigma_{z0,\,FEM}^C/\sigma_{z0,\,FEM}^P\right)_{max}$. In this case, the singular stress does not appear at the interface end.

It is found that the ISSF ratio $\left(K_\sigma^C\right)_{max}/K_\sigma^P \to \infty$ as $\alpha \to 2\beta$. However, it should be noted that the singular stress field disappears since the singular index $\lambda \to 1$ as $\alpha \to 2\beta$. Therefore, the stress ratio $\left(\sigma_{z0,\,FEM}^C/\sigma_{z0,\,FEM}^P\right)_{max}$ may be useful than the ISSF ratio K_σ^C/K_σ^P around $\alpha=2\beta$.

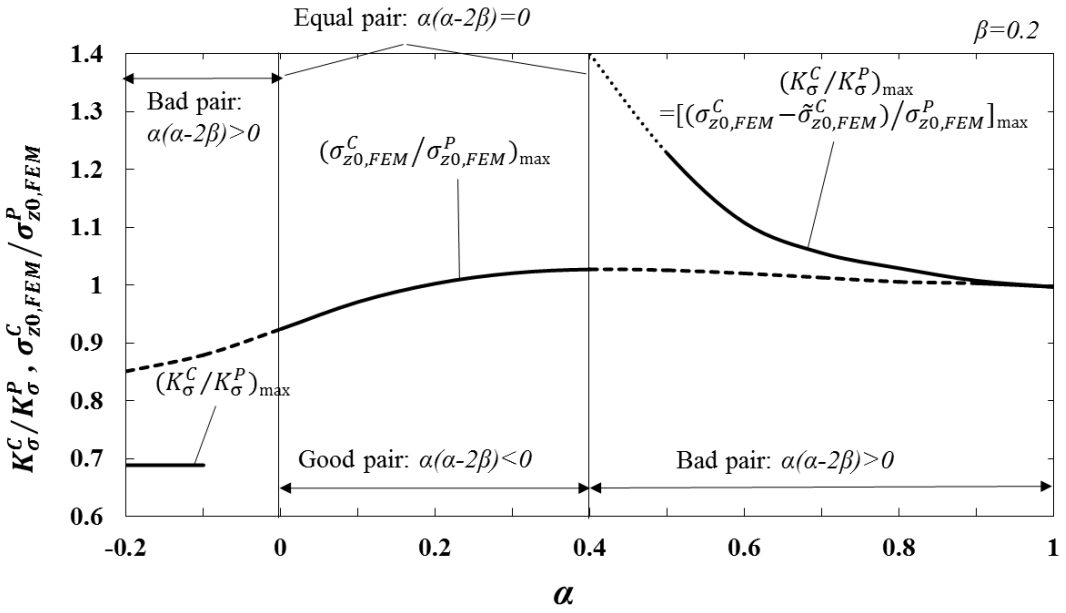

Fig. 3.5 Maximum values of K_σ^C/K_σ^P and $\sigma_{z0,FEM}^C/\sigma_{z0,FEM}^P$ when $\beta = 0.2$

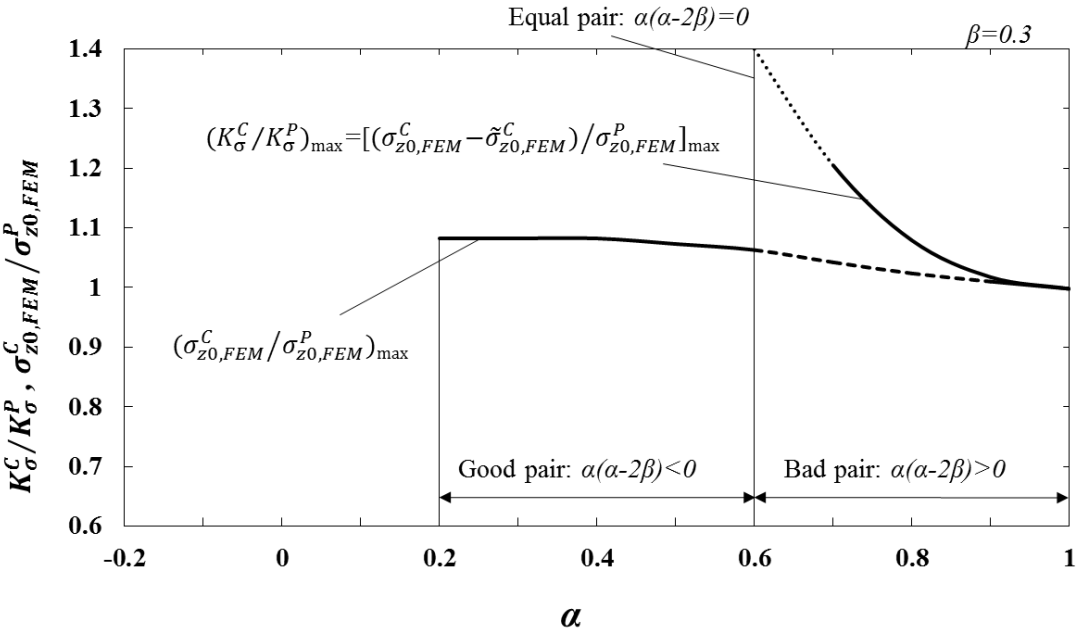

Fig. 3.6 Maximum values of K_σ^C/K_σ^P and $\sigma_{z0,FEM}^C/\sigma_{z0,FEM}^P$ when $\beta = 0.3$

3.6 Analysis results for cylindrical butt joint under arbitrary material combinations

As is discussed in the previous sector, different regions will use different values to evaluate the debonding strength. In this research, both K_σ^C/K_σ^P and $\sigma_{z0,\,FEM}^C/\sigma_{z0,\,FEM}^P$ will be considered, both in maximum and minimum values. Fig. 3.7 and Fig. 3.8 and Tables 3.7 and 3.8 show the maximum and minimum values of K_σ^C/K_σ^P and $\sigma_{z0,\,FEM}^C/\sigma_{z0,\,FEM}^P$ calculated by varying (α, β). As mentioned above, K_σ^C/K_σ^P is used for predicting the debonding strength for bad pairs $\alpha(\alpha\text{-}2\beta)>0$, this is because the stress singularity occurs at the interface end when $\alpha(\alpha\text{-}2\beta)>0$. On the other hand, $\sigma_{z0,\,FEM}^C/\sigma_{z0,\,FEM}^P$ may be used for predicting the debonding strength for good pairs $\alpha(\alpha\text{-}2\beta)\leq 0$. However, when $\alpha\cong 2\beta$, it is not known whether K_σ^C/K_σ^P or $\sigma_{z0,\,FEM}^C/\sigma_{z0,\,FEM}^P$ is suitable for predicting the strength because $\left(K_\sigma^C\right)_{max}/K_\sigma^P$ goes to infinity when $\alpha\rightarrow 2\beta$. Fig. 3.7 and Fig. 3.8 and Tables 3.7 and 3.8 are useful when $h/W\leq 0.01$. Since the solution for the case $h/W\geq 1.0$ was shown in the Appendix B, the accurate results can be obtained by the interpolation also in the range for $0.01\leq h/W\leq 1.0$.

Fig. 3.9 shows the Dundurs' parameters for the several engineering materials [6]. Although $\left(K_\sigma^C\right)_{max}/K_\sigma^P$ in Fig. 3.7 goes to infinity around the equal pair condition, $\left(K_\sigma^C\right)_{max}/K_\sigma^P$ is less than 1.5 for most of the bad pair region $\alpha(\alpha\text{-}2k\beta)\geq 0$, $k=1.0-0.61(\beta^2-0.25)$ as indicated in Fig. 3.9.

Table 3.7 Maximum and minimum values of K_σ^C / K_σ^P when $h/W \leq 0.01$

α \ β	-0.4	-0.3	-0.2	-0.1	0	0.1	0.2	0.3	0.4
-1	1.220 0.977	1.102 0.945	0.951 0.838	0.696 0.697	0.615 0.636				
-0.9	1.294 0.986	1.141 0.949	0.991 0.845	0.738 0.703	0.652 0.646				
-0.8		1.187 0.956	1.044 0.855	0.819 0.722	0.720 0.670				
-0.7		1.260 0.978	1.121 0.875	0.906 0.748	0.779 0.709				
-0.6			1.258 0.889	0.988 0.771	0.829 0.737	0.650 0.684			
-0.5			1.364 0.902	1.043 0.791	0.887 0.758	0.687 0.704			
-0.4				1.108 0.811	0.919 0.776	0.708 0.721			
-0.3				1.153 0.834	0.938 0.796	0.736 0.736			
-0.2					0.952 0.825	0.779 0.749	0.688 0.658		
-0.1					0.962 0.861	0.795 0.763	0.698 0.683		
0			0.987 0.961	0.989 0.895		0.803 0.775	0.710 0.698		
0.1			0.987 0.972	0.990 0.914	0.991 0.924				
0.2			0.987 0.981	0.991 0.938	0.992 0.942				
0.3				0.992 0.951	0.993 0.954	1.153 0.971			
0.4				0.992 0.960	0.994 0.965	1.052 0.972			
0.5				0.993 0.966	0.994 0.973	1.022 0.977	1.228 0.988		
0.6				0.994 0.970	0.995 0.980	1.010 0.982	1.108 0.987		
0.7					0.994 0.985	1.003 0.986	1.056 0.989	1.205 0.994	
0.8					0.995 0.987	1.000 0.990	1.029 0.992	1.079 0.995	
0.9					0.996 0.989	1.000 0.995	1.008 0.996	1.018 0.997	1.091 0.999
1					0.996 0.991	0.996 0.996	0.997 0.997	0.998 0.998	1.000 1.000

Upper: maximum value, lower: minimum value

Table 3.8 Maximum and minimum values of $\sigma^{C}_{z0,FEM}/\sigma^{P}_{z0,FEM}$ when $h/W \le 0.01$

α \ β	-0.4	-0.3	-0.2	-0.1	0	0.1	0.2	0.3	0.4
-1	1.001 1.001	0.966 0.966	0.922 0.922	0.856 0.856	0.815 0.815				
-0.9	1.032 1.016	0.988 0.974	0.937 0.931	0.879 0.874	0.832 0.830				
-0.8	1.085 1.035	1.011 0.983	0.968 0.942	0.896 0.891	0.844 0.841				
-0.7	1.136 1.047	1.052 0.993	0.996 0.956	0.934 0.911	0.861 0.853				
-0.6		1.103 1.001	1.037 0.969	0.992 0.925	0.890 0.864	0.826 0.826			
-0.5		1.131 1.013	1.075 0.987	1.025 0.947	0.921 0.876	0.831 0.831			
-0.4		1.143 1.021	1.095 1.000	1.044 0.963	0.952 0.889	0.846 0.846			
-0.3		1.134 1.024	1.101 1.004	1.044 0.982	0.973 0.909	0.866 0.866			
-0.2		1.121 1.024	1.087 1.006	1.043 1.000	0.987 0.949	0.901 0.901	0.861 0.861		
-0.1			1.065 1.005	1.039 1.001	0.995 0.983	0.939 0.929	0.879 0.879		
0			1.045 1.003	1.032 1.001	1.000 1.000	0.966 0.965	0.924 0.924		
0.1			1.029 1.003	1.020 1.000	1.004 1.000	0.992 0.986	0.971 0.971		
0.2			1.003 1.003	1.003 0.998	1.002 0.999	1.000 0.998	1.003 0.989	1.082 1.010	
0.3				1.000 0.996	0.999 0.997	1.004 0.999	1.021 0.996	1.082 1.009	
0.4				0.996 0.995	0.997 0.994	1.006 0.996	1.027 0.997	1.082 1.008	
0.5				0.996 0.994	0.996 0.992	1.005 0.994	1.026 0.998	1.073 1.006	
0.6				0.995 0.993	0.996 0.991	1.004 0.992	1.020 0.996	1.063 1.000	
0.7					0.995 0.991	1.001 0.992	1.013 0.994	1.042 0.998	1.085 1.001
0.8					0.995 0.991	1.000 0.993	1.006 0.995	1.024 0.997	1.054 1.000
0.9					0.995 0.991	1.000 0.996	1.003 0.997	1.010 0.998	1.025 1.000
1					0.996 0.991	0.996 0.996	0.997 0.997	0.998 0.998	1.000 1.000

Upper: maximum value, lower: minimum value

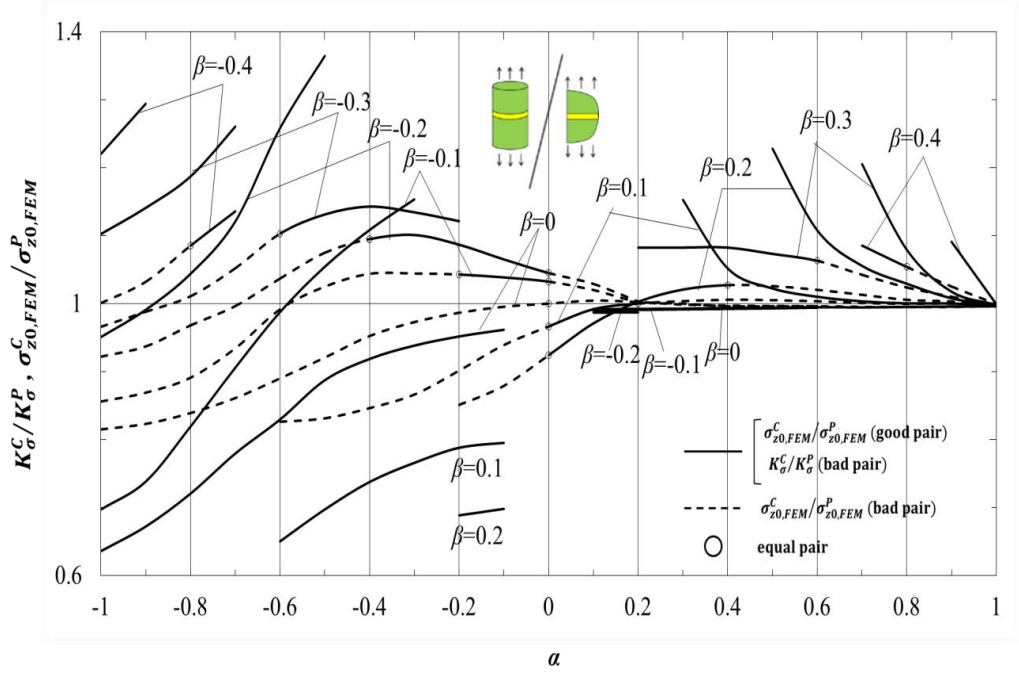

Fig. 3.7 Maximum value of K_σ^C/K_σ^P and $\sigma_{z0,FEM}^C/\sigma_{z0,FEM}^P$ when h/W≤0.01

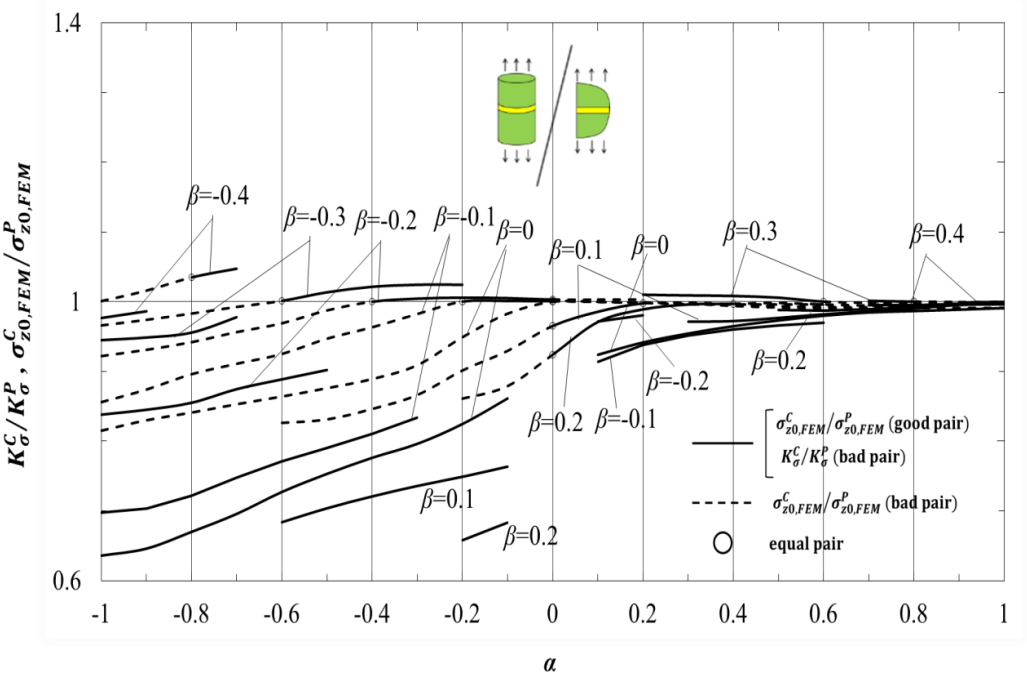

Fig. 3.8 Minimum value of K_σ^C/K_σ^P and $\sigma_{z0,FEM}^C/\sigma_{z0,FEM}^P$ when h/W≤0.01

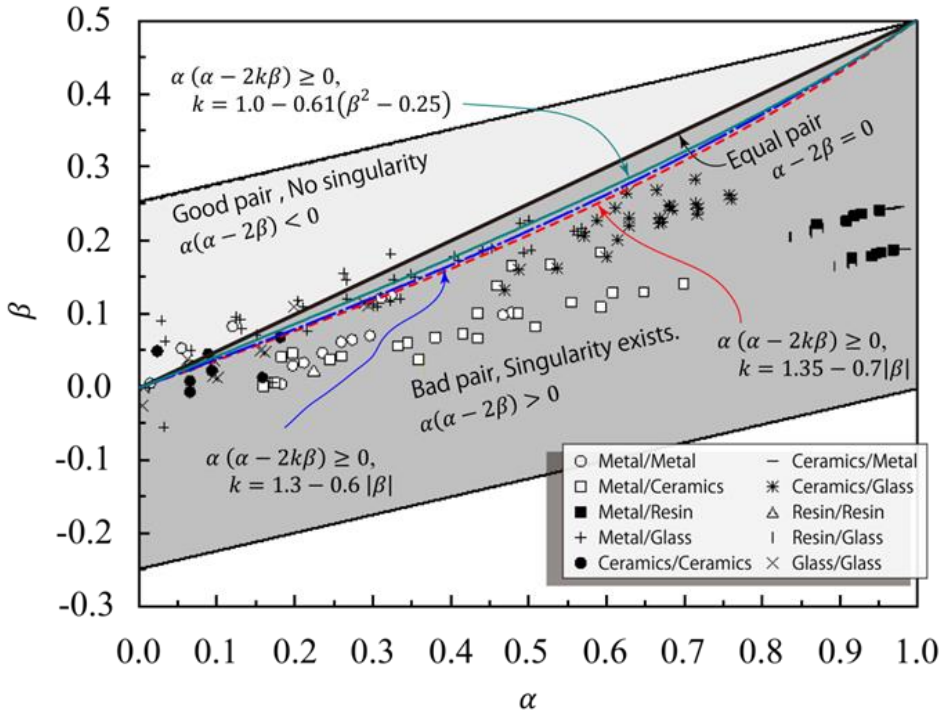

Fig. 3.9 Dundurs' parameters for the several engineering materials

Fig. 3.9 also shows that almost all (α, β) of engineering materials are distributed in $0 \leq |\beta| \leq 0.3$ [1], therefore, the stress ratio $\sigma^{C}_{z0,\,FEM}/\sigma^{P}_{z0,\,FEM}$ can be discussed in this range. It should be noted that the stress ratio $\left(\sigma^{C}_{z0,\,FEM}/\sigma^{P}_{z0,\,FEM}\right)_{\max}$ is always finite in this range. Comparing Fig. 3.7 with Fig. 3.8, it is found that the value of $\sigma^{C}_{z0,\,FEM}/\sigma^{P}_{z0,\,FEM}$ varies depending on (α, β) but the value of $\left(\sigma^{C}_{z0,\,FEM}/\sigma^{P}_{z0,\,FEM}\right)_{\max}$ is in the small range for most of good pairs in $\alpha\,(\alpha\text{-}2\beta)<0$ and $0 \leq |\beta| \leq 0.3$. Also, the difference between $\left(\sigma^{C}_{z0,\,FEM}/\sigma^{P}_{z0,\,FEM}\right)_{\max}$ and $\left(\sigma^{C}_{z0,\,FEM}/\sigma^{P}_{z0,\,FEM}\right)_{\min}$ is small in this region. The value range and the maximum and minimum value difference can be expressed in Eq. (3.16).

$$0.971 \leq \left(\frac{\sigma_{z0,\,FEM}^{C}}{\sigma_{y0,\,FEM}^{P}}\right)_{max} \leq 1.143\,, \quad \frac{\left(\frac{\sigma_{z0,\,FEM}^{C}}{\sigma_{y0,\,FEM}^{P}}\right)_{max} - \left(\frac{\sigma_{z0,\,FEM}^{C}}{\sigma_{y0,\,FEM}^{P}}\right)_{min}}{\left(\frac{\sigma_{z0,\,FEM}^{C}}{\sigma_{y0,\,FEM}^{P}}\right)_{max} + \left(\frac{\sigma_{z0,\,FEM}^{C}}{\sigma_{y0,\,FEM}^{P}}\right)_{min}} \leq 0.1\,, \tag{3.16}$$

when $0 \leq |\beta| \leq 0.3$ and $\alpha\,(\alpha - 2\beta) < 0$

The difference between $\left(\sigma_{z0,\,FEM}^{C}/\sigma_{z0,\,FEM}^{P}\right)_{\max}$ and $\left(\sigma_{z0,\,FEM}^{C}/\sigma_{z0,\,FEM}^{P}\right)_{\min}$ is less than 10% in Eq. (3.16), and therefore, Dundurs' parameters can almost control the results and be used for axi-symmetrical bonded structures.

Since $\left(K_{\sigma}^{C}\right)_{max}/K_{\sigma}^{P}$ goes to infinity when $\alpha \rightarrow 2\beta$, it is not clear whether $K_{\sigma}^{C}/K_{\sigma}^{P}$ or $\sigma_{z0,\,FEM}^{C}/\sigma_{z0,\,FEM}^{P}$ is suitable for predicting the strength at present.

3.7 Experimental evaluation of debonding strength of cylindrical butt joint

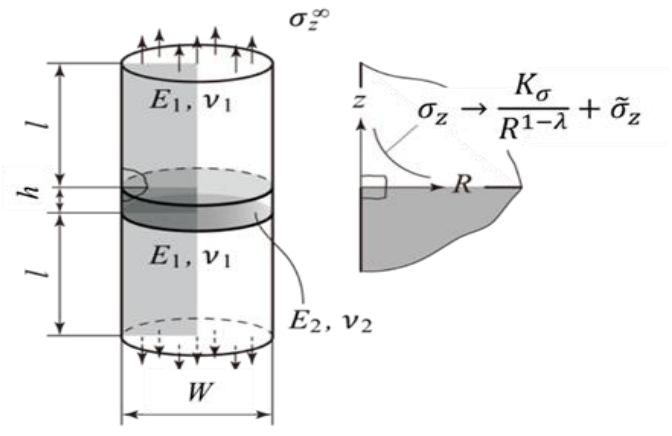

Fig. 3.10 Schematic illustration of cylindrical butt joint

The debonding strength of the cylindrical butt joints was studied experimentally by several researchers [7]. Fig. 3.10 shows the schematic illustration of the specimens. In this experiment of Naito et al [7], the adherent is aluminum alloy 5052-H34 (Young's modulus E_1 = 69.6GPa, Poisson's ratio ν_1 = 0.33) and the adhesive is polyimide (E_2 = 3.77GPa, ν_2 = 0.342). Table 3.9 shows Dundurs' parameters (α, β) and singular index λ. The length of the adherent l is 38.1 mm and the adhesive thickness t is varied from 0.2mm to 0.6mm.

Table 3.9 Dundurs' parameters (α, β) and order of singular index λ of cylindrical butt joint (aluminum/polyimide)

Materials	Adherend		Adhesive		Dundurs' parameter		Singular index
	E_1 [GPa]	ν_1	E_2 [GPa]	ν_2	α	β	λ
Aluminum/Polyimide	69.9	0.33	3.77	0.342	0.8963	0.2145	0.7398

Fig. 3.11 shows the tensile strength σ_c which increases with increasing the adhesive thickness. In the experiment, the fracture was initiated at the axisymmetric interface end between the adhesive and the adherent. Fig. 3.12 shows the dimensionless of ISSFs for the cylindrical butt joint specimens $F_\sigma^C = K_\sigma^C/(\sigma_z^\infty W^{1-\lambda})$ and $F_\sigma^{C*} = K_\sigma^C/(\sigma_z^\infty h^{1-\lambda})$. In Fig. 3.12 F_σ^C and F_σ^{C*} increase with increasing the adhesive thickness. However, F_σ^{C*} is almost constant when h is small. F_σ^{C*} can be used conveniently to evaluate the adhesive strength for small h cases. Fig. 3.13 shows the critical ISSF at $\sigma_z^\infty = \sigma_c$, $K_{\sigma c} = K_\sigma^C\,|_{\sigma_z^\infty = \sigma_c}$. The $K_{\sigma c}$ values are almost constant

independent of the adhesive thickness. It can be confirmed that the ISSF can be used for evaluating the debonding strength.

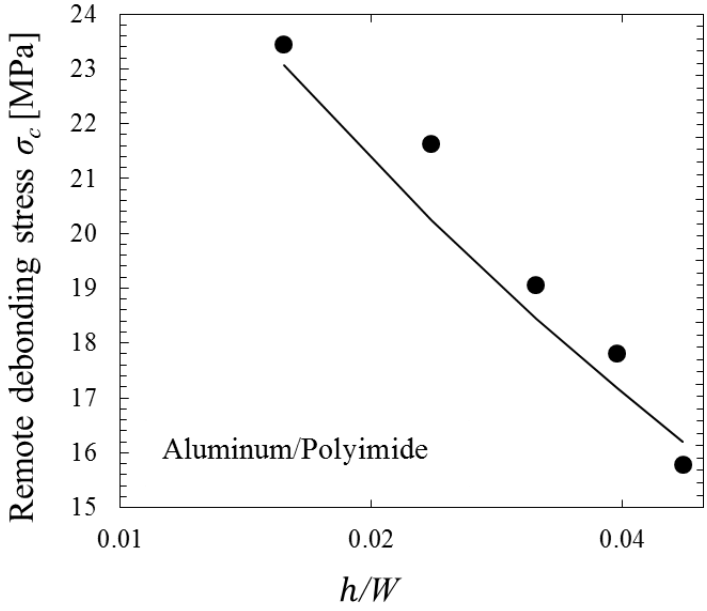

Fig. 3.11 Experimental remote debonding stress σ_c of cylindrical butt joint

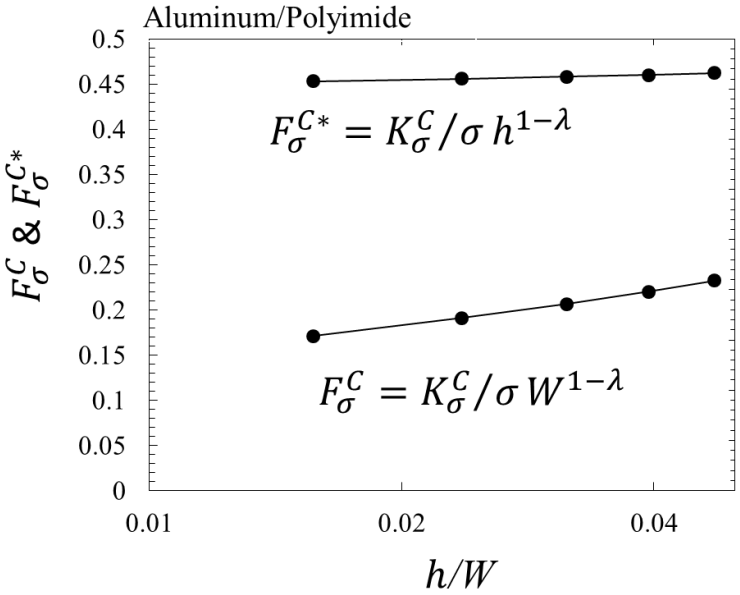

Fig. 3.12 ISSF of experimental cylindrical butt joint specimen

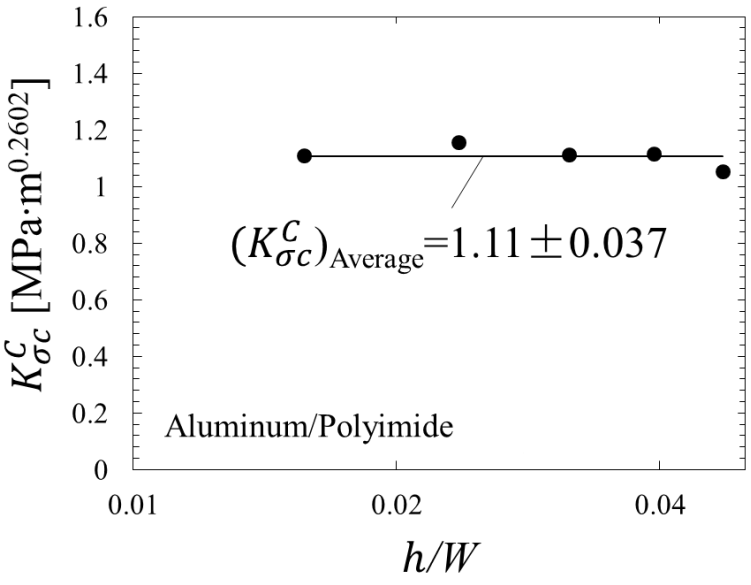

Fig. 3.13 Critical ISSF of experimental cylindrical butt joint specimen

3.8 Conclusion

In this chapter, the ISSF variations were clarified over the entire adhesive thickness range for cylindrical butt joint. The results were calculated by changing the material combination systematically under (α, β) space. The result of cylindrical butt joint has been compared with that of plate butt joint and the difference was elaborated. After that, the maximum and minimum values of $K_{\sigma}^{C}/K_{\sigma}^{P}$ and $\sigma_{z0,\,FEM}^{C}/\sigma_{z0,\,FEM}^{P}$ are shown in tables and charts in the space of Dundurs' parameters.

For the cylindrical butt joint, the circumferential strain at the interface end, ε_{r0}^{C}, is not influenced by the stress singularity because ε_{r0}^{C} is obtained from the radial displacement u_{r0}^{C} and the cylinder radius. It was found that the non-singular stresses caused by the ε_{r0}^{C} are contained in the FEM stresses at the interface end. The accurate

method was used for calculating the ISSF from the ratio of the stress obtained by subtracting the non-singular stress to the stress of the plate butt joint adopted as the reference solution. The stress-free boundary condition causes the non-singular stresses $\tilde{\sigma}^{C}_{r0,FEM} = \tilde{\tau}^{C}_{rz0,FEM} = 0$. The ISSF can be calculated easily without subtraction process of the non-singular stresses when the radial stress $\sigma^{C}_{r0,FEM}$ or the shear stress $\tau^{C}_{rz,FEM}$ is used.

For a certain material combination, the ISSF F^{C*}_{σ} normalized by adhesive thickness h becomes constant with decreasing adhesive thickness when $h/W \leq 0.01$. Thin adhesive layer can be used to improve the interface strength of the cylindrical butt joint. Since the ISSFs of the cylindrical butt joint cannot be totally dominated by the Dundurs' parameter α and β, the maximum and minimum values of the $K^{C}_{\sigma}/K^{P}_{\sigma}$ and $\sigma^{C}_{z0,\,FEM}/\sigma^{P}_{z0,\,FEM}$ were shown in the charts and tables for various (α, β). The value $K^{C}_{\sigma}/K^{P}_{\sigma}$ may be useful for predicting the debonding strength under the bad pairs $\alpha(\alpha\text{-}2\beta)>0$. On the other side, the $\sigma^{C}_{z0,\,FEM}/\sigma^{P}_{z0,\,FEM}$ may be more important for predicting the debonding strength under the good pairs $\alpha(\alpha\text{-}2\beta)\leq 0$. Since the solution for $h/W \geq 1.0$ was shown in the Appendix B, the accurate results can be obtained by the interpolation also in the range for $0.01 \leq h/W \leq 1.0$.

$\left(K^{C}_{\sigma}\right)_{max}/K^{P}_{\sigma}$ is less than 1.5 for most of the bad pair region. The difference between $\left(\sigma^{C}_{z0,\,FEM}/\sigma^{P}_{z0,\,FEM}\right)_{\max}$ and $\left(\sigma^{C}_{z0,\,FEM}/\sigma^{P}_{z0,\,FEM}\right)_{\min}$ is less than 10%. Dundurs' parameters α and β can almost control the results and be used for axi-symmetrical bonded structures.

3.9 Reference of Chapter 3

[1] Miyazaki, T., Noda, N.A., Ren, F., Wang, Z., Sano, Y., Iida, K., Analysis of intensity of singular stress field for bonded cylinder and bonded pipe in comparison with bonded plate, Int. J. Adhes. Adhes., 77 (2017), 118-137.

[2] Timoshenko, S.P., Goodier,J.N., Theory of elasticity. Third Edition NewYork: McGrawHill, pp. 380, 1970.

[3] Li, Y.L., Hu, S.Y., Munz, D., Yang, Y.Y., Asymptotic description of the stress field around the bond edge of a cylindrical joint, Archive of Applied Mechanics, 68 (1998), 552 -565.

[4] Hu, Q., Sato, Y., Watanabe, K., Dependence of stress state on elastic constants in axisymmetric dissimilar materials. Trans. Jpn. Soc. Mech. Eng. Ser. A., 65 (1999), 1010-1017. [in Japanese].

[5] Hu, Q., Watanabe, K., A study on fundamental properties of elastic parameters related to stress field for dissimilar materials. Trans. Jpn. Soc. Mech. Eng. Ser. A., 69(2003), 594-601. [in Japanese].

[6] Yuuki, R., Mechanics of Interface, first ed. Baifuukann, Tokyo, 1992 [in Japanese].

[7] Naito, K., Onta, M., Kogo, Y., The effect of adhesive thickness on tensile and shear strength of polyimide adhesive, Int. J. Adhes. Adhes., 36 (2012), 77 -85.

Chapter 4 Analysis on intensity of singular stress on the interface outer edge of three-dimensional butt joint

4.1 Introduction

So far, many studies on two-dimensional joints have been carried out theoretically and experimentally. In Chapter 2 and 3, the ISSF of butt joint was studied by using two-dimensional butt joint model, the ISSF variations were clarified over the entire adhesive thickness range for plate and cylindrical butt joints, and we found that the debonding strength can be expressed as a constant value of critical ISSF. However, the stress distribution of three-dimensional joint is not so clear as that of two-dimensional joint.

Suzuki [1] discussed the experimental adhesive strength when S35CJIS medium carbon steel plates are bonded by epoxy resin. Suzuki's experimental specimens were analyzed by using two-dimensional butt joint model in Chapter 2. Furthermore Akisanya and Meng [2] discussed the experimental adhesive strength for the butt joints with rectangular cross section. In this chapter, the adhesively bonded specimens used by Suzuki and Akisanya [1, 2] will be analyzed by using three-dimensional butt joint model to study the intensity of the singular stress field on the interface outer edge of three-dimensional butt joint.

4.2 Stress distribution on the interface outer edge

Fig. 4.1 shows the three-dimensional butt joint model. Because of the symmetry, the three-dimensional butt joint in Fig. 4.1(a) can be simplified into a one-eighth model as is shown in Fig. 4.1(b). The symmetry planes are *x*-*z* plane, *y*-*z* plane, and plane z=-0.5h. The symmetry planes are fixed in the normal direction. In the calculation, the width W=1 and the stress applying to the z direction σ=1. Fig. 4.1(c) shows the two-dimensional plane strain butt joint model. The mesh details are shown in Fig. 4.2. Submodeling for the interface outer edge is used to reduce the number of elements. The finely meshed submodel in Fig. 4.2(a) is a small part near the interface outer edge. Displacements calculated on the cut boundary of the coarse model in Fig. 5(b) are specified as boundary conditions for the submodel.

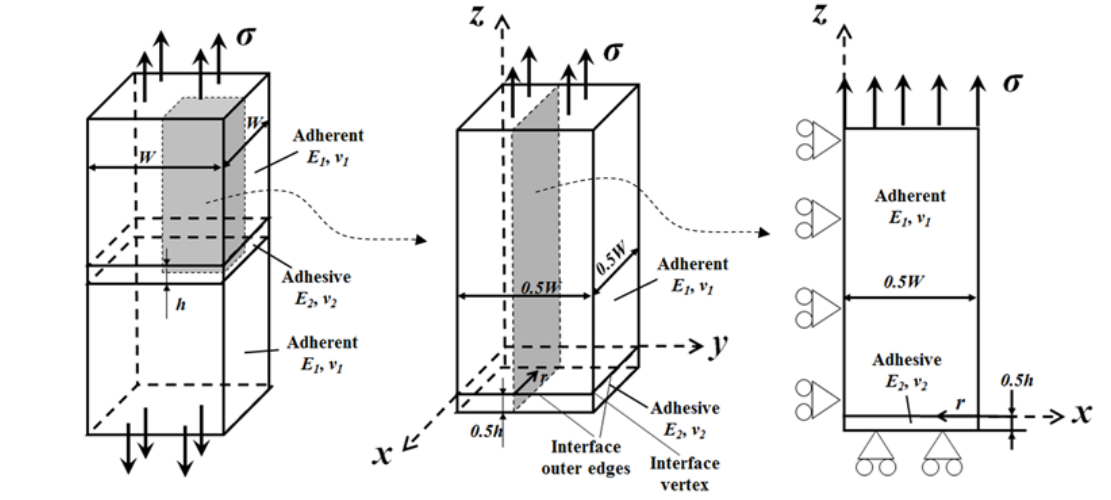

(a) Three-dimensional butt joint

(b) One-eighth model for three-dimensional butt joint

(c) Two-dimensional butt joint model

Fig. 4.1 Three-dimensional and two-dimensional butt joint models

Fig. 4.3 shows an example of the interface stress distributions in three-dimensional butt joint when h/W=0.1 with different mesh sizes. Here, one of the adhesively bonded specimens used by Suzuki [1] is considered where the adherent S35C is bonded with adhesive epoxy resin. The elastic properties of the materials are Young's modulus E=210GPa and Poisson's ratio v=0.3 for S35C, and E=3.14GPa and v=0.37 for epoxy resin. From Fig. 4.3, in the interior area of the interface where $0 \leq x, y < 0.45$, the same values of stress $|\sigma_z - 1| < 0.002$ are obtained by using different mesh sizes. However, the values of stress near the interface outer edges are quite different when different meshes are applied. The stress decreases at first and then increases rapidly close to the interface outer edges. The singularity occurs on the interface outer edges. Therefore, the stress distribution on the outer edge of interface in the three-dimensional joint will be focused on in this study.

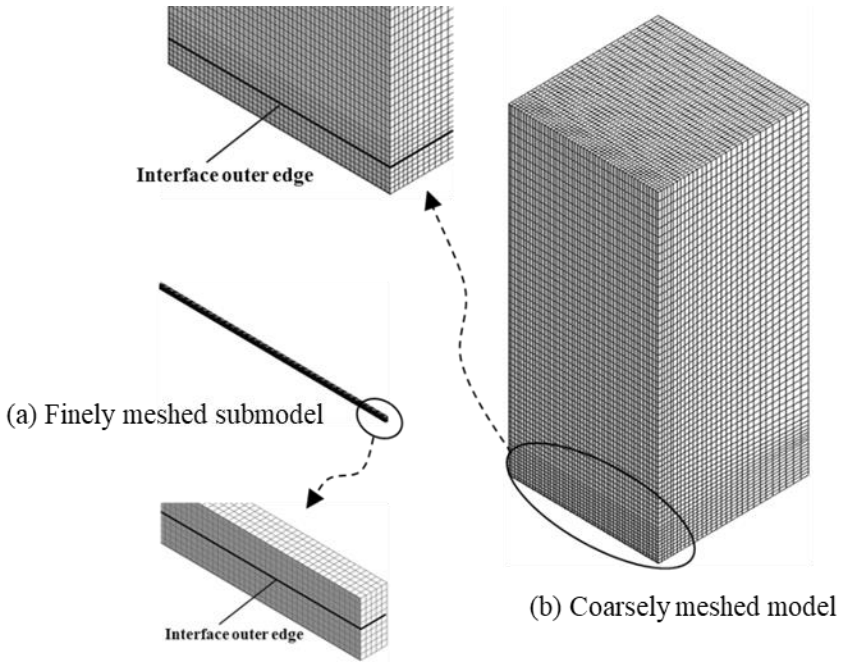

Fig. 4.2 Mesh details

In the one-eighth model in Fig. 4.1(b), there are two interface outer edges, one is

parallel to the x axis and another is perpendicular to the y axis. Considering one of two edges is enough because of the symmetry. We choose the edge which is parallel to the y axis to study. For convenience, the y coordinate value is used to describe the position on the edge, y=0.5 means the point at the end of the edge, the interface vertex. Table 4.1 shows the stress distributions obtained by FEM on the interface outer edge in three-dimensional butt joint when h/W=0.01 and h/W≥1. It can be seen from Table 4.1 that the stresses $\sigma_{z,h/W=0.01}^{3D,FEM}$ and $\sigma_{z,h/W\geq 1}^{3D,FEM}$ vary depending on the finite element mesh size but the ratio of the stress $\sigma_{z,h/W=0.01}^{3D,FEM}/\sigma_{z,h/W\geq 1}^{3D,FEM}$ is independent of the mesh size. Furthermore, the ratio of the stress $\sigma_{z,h/W=0.01}^{3D,FEM}/\sigma_{z,h/W\geq 1}^{3D,FEM}$ tends to be a constant away from the interface vertex (when y<0.447).

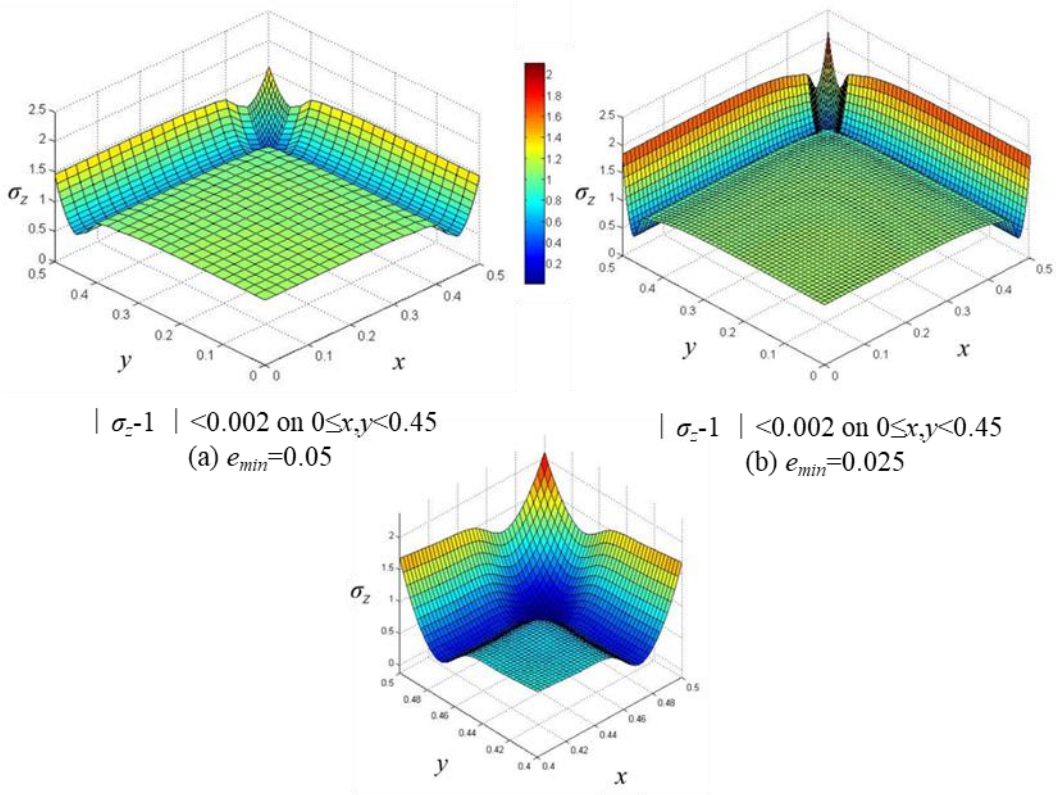

| σ_z-1 | <0.002 on 0≤x,y<0.45
(a) e_{min}=0.05

| σ_z-1 | <0.002 on 0≤x,y<0.45
(b) e_{min}=0.025

(c) Detail of x,y=0.4~0.5

Fig. 4.3 Interface stress distribution of three-dimensional butt joint (E_1=210GPa, ν_1=0.3, E_2=3.14GPa, ν_2=0.37)

Table 4.1 Stress distributions for three-dimensional joint under tension obtained by different mesh sizes when h/W=0.01 and h/W≥1

(E_1=210GPa, ν_1=0.3, E_2=3.14GPa, ν_2=0.37)

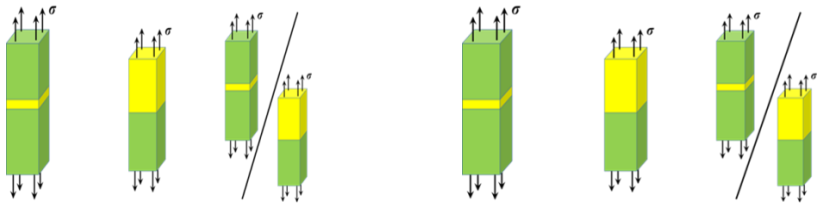

y	Smallest mesh size e_{min}=1/3200 around the edge			Smallest mesh size e_{min}=1/12800 around the edge		
	$\sigma_{z,h/W=0.01}^{3D,FEM}$	$\sigma_{z,h/W\geq1}^{3D,FEM}$	$\frac{\sigma_{z,h/W=0.01}^{3D,FEM}}{\sigma_{z,h/W\geq1}^{3D,\mathrm{FEM}}}$	$\sigma_{z,h/W=0.01}^{3D,FEM}$	$\sigma_{z,h/W\geq1}^{3D,FEM}$	$\frac{\sigma_{z,h/W=0.01}^{3D,FEM}}{\sigma_{z,h/W\geq1}^{3D,\mathrm{FEM}}}$
0	3.282	13.006	0.252	4.941	19.540	0.253
0.053	3.282	12.991	0.253	4.939	19.513	0.253
0.105	3.283	12.978	0.253	4.939	19.498	0.253
0.158	3.284	12.956	0.253	4.941	19.471	0.254
0.211	3.285	12.931	0.254	4.942	19.418	0.255
0.263	3.287	12.908	0.255	4.945	19.390	0.255
0.316	3.290	12.900	0.255	4.950	19.382	0.255
0.368	3.294	12.944	0.254	4.957	19.444	0.255
0.421	3.303	13.129	0.252	4.970	19.718	0.252
0.447	3.311	13.374	0.248	4.982	20.082	0.248
0.474	3.302	13.933	0.237	4.968	20.931	0.237
0.5	4.483	31.002	0.145	7.538	52.086	0.145

Table 4.2 The ratios of stress components at y=0

	$\frac{\sigma_{x,h/W=0.01}^{3D,FEM}}{\sigma_{x,h/W\geq1}^{3D,\mathrm{FEM}}}$		$\frac{\sigma_{y,h/W=0.01}^{3D,FEM}}{\sigma_{y,h/W\geq1}^{3D,\mathrm{FEM}}}$		$\frac{\sigma_{z,h/W=0.01}^{3D,FEM}}{\sigma_{z,h/W\geq1}^{3D,\mathrm{FEM}}}$	
Material	Mat. 1	Mat. 2	Mat. 1	Mat. 2	Mat. 1	Mat. 2
e_{min}=1/3200	0.253	0.253	0.138	0.252	0.252	0.252
e_{min}=1/12800	0.253	0.253	0.196	0.253	0.253	0.253

Now we pick a point on the interface outer edge to investigate. Table 4.2 shows the ratios of stress components at y=0. The ratio $\sigma_{y,h/W=0.01}^{3D,FEM}/\sigma_{y,h/W\geq1}^{3D,FEM}$ is quite different

from that of other stress components even though the same FE mesh is applied. This is the nature of three-dimensional problem. As is mentioned in Chapter 3, for the two-dimensional plain strain problem in Fig. 4.1(c), the strain of *y* direction is zero. While for the three-dimensional problem as shown in Fig. 4.1(a) and Fig. 4.1(b), the strain of *y* direction ε_y in the interface can lead to non-zero stresses [3], and then the stress in the interface of three-dimensional problem is expressed as:

$$\sigma_j^{3D} = \frac{K_{\sigma_j}^{3D}}{r^{1-\lambda}} + \tilde{\sigma}_j^{3D} = \hat{\sigma}_j^{3D} + \tilde{\sigma}_j^{3D} \left(j = x, \mathrm{y}, \mathrm{z} \right) \tag{4.1}$$

where *r* is the perpendicular distance from the outer edge of the interface.

In the outer edge of the interface, the first terms, $\hat{\sigma}_j^{3D}$, is called singular stress, and the second term in Eq. (4.1), called non-singular stress, have the expressions as

$$\left(\tilde{\sigma}_x^{3D}\right)^{\mathrm{mat1}}, \left(\tilde{\sigma}_y^{3D}\right)^{\mathrm{mat1}}, \left(\tilde{\sigma}_z^{3D}\right)^{\mathrm{mat1}} \quad \text{in material 1;}$$

$$\left(\tilde{\sigma}_x^{3D}\right)^{\mathrm{mat2}}, \left(\tilde{\sigma}_y^{3D}\right)^{\mathrm{mat2}}, \left(\tilde{\sigma}_z^{3D}\right)^{\mathrm{mat2}} \quad \text{in material 2.}$$

The non-singular stresses are obtained as follows [4],

$$\left(\tilde{\sigma}_z^{3D}\right)^{\mathrm{mat1}} = \left(\tilde{\sigma}_z^{3D}\right)^{\mathrm{mat2}} = \tilde{\sigma}_z^{3D} = -\frac{\left(\nu_1 - \nu_2\right) E_1 E_2}{\left(1+\nu_1\right)\nu_1 E_2 - \left(1+\nu_2\right)\nu_2 E_1} \varepsilon_y \tag{4.2}$$

$$\left(\tilde{\sigma}_y^{3D}\right)^{\mathrm{mat1}} = \frac{\left(1+\nu_2\right)\left(\nu_1 E_2 - \nu_2 E_1\right) E_1}{\left(1+\nu_1\right)\nu_1 E_2 - \left(1+\nu_2\right)\nu_2 E_1} \varepsilon_y \tag{4.3}$$

$$\left(\tilde{\sigma}_y^{3D}\right)^{\mathrm{mat2}} = \frac{\left(1+\nu_1\right)\left(\nu_1 E_2 - \nu_2 E_1\right) E_2}{\left(1+\nu_1\right)\nu_1 E_2 - \left(1+\nu_2\right)\nu_2 E_1} \varepsilon_y \tag{4.4}$$

$$\left(\tilde{\sigma}_x^{3D}\right)^{\text{mat1}} = \left(\tilde{\sigma}_x^{3D}\right)^{\text{mat2}} = 0 \tag{4.5}$$

Table 4.3 shows the ratios of singular stresses at y=0. It is found that the ratios are independent of the element size e_{min}. According to Eq. (4.5), the ratio of the singular stress field can be calculated easily when $\sigma_x^{3D,FEM}$ is used. Now the mesh-independent calculation method for three-dimensional joint is shown as follow,

$$\begin{aligned} \frac{F_\sigma^{3D}}{F_{\sigma,REF}^{3D}} &= \frac{\sigma_z^{3D,FEM} - \tilde{\sigma}_z^{3D}}{\sigma_{z,REF}^{3D,FEM} - \tilde{\sigma}_{z,REF}^{3D}} \qquad \left(reference\ \ is\ \ 3D\right) \\ \frac{F_\sigma^{3D}}{F_{\sigma,REF}^{2D}} &= \frac{\sigma_z^{3D,FEM} - \tilde{\sigma}_z^{3D}}{\sigma_{z,REF}^{2D,FEM}} \qquad \left(reference\ \ is\ \ 2D\right) \end{aligned} \tag{4.6}$$

Table 4.3 The ratios of singular stress components at y=0

	$\frac{\sigma_{x,h/W=0.01}^{3D,FEM} - \tilde{\sigma}_{x,h/W=0.01}^{3D}}{\sigma_{x,h/W\geq1}^{3D,\text{FEM}} - \tilde{\sigma}_{x,h/W\geq1}^{3D}}$		$\frac{\sigma_{y,h/W=0.01}^{3D,FEM} - \tilde{\sigma}_{y,h/W=0.01}^{3D}}{\sigma_{y,h/W\geq1}^{3D,\text{FEM}} - \tilde{\sigma}_{y,h/W\geq1}^{3D}}$		$\frac{\sigma_{z,h/W=0.01}^{3D,FEM} - \tilde{\sigma}_{z,h/W=0.01}^{3D}}{\sigma_{z,h/W\geq1}^{3D,\text{FEM}} - \tilde{\sigma}_{z,h/W\geq1}^{3D}}$	
Material	Mat. 1	Mat. 2	Mat. 1	Mat. 2	Mat. 1	Mat. 2
e_{min}=1/3200	0.253	0.253	0.251	0.253	0.252	0.252
e_{min}=1/12800	0.253	0.253	0.252	0.253	0.253	0.253

To obtain the ISSF of three-dimensional joint by using the singular stress ratio, a reference solution to be used in the denominator is necessary as is shown in Eq. (4.6). In Table 4.3, the three-dimensional butt joint when $h/W\geq1$ is the reference. Unfortunately, the ISSF of three-dimensional butt joint when $h/W\geq1$, $F_{\sigma,h/W\geq1}^{3D}$, is not clear so far, the ISSF when h/W=0.01, $F_{\sigma,h/W=0.01}^{3D}$, cannot be obtained although the singular stress ratios can be gotten. The ISSF $F_{\sigma,h/W\geqslant1}^{2D}$ for bonded plate (see

Appendix A), which was used as the reference in Chapter 2, is a good choice to be the reference. However, if the reference problem in the denominator is a two-dimensional plain strain problem without the strain of y direction, the ratios of stresses cannot be accurate close to the interface vertex. Table 4.4 shows the ratios of singular stresses when bonded plate is the reference. The ratio of singular stress $(\sigma^{3D,FEM}_{z,h/W=0.01}-\tilde{\sigma}^{3D}_{z,h/W=0.01})/\sigma^{2D,FEM}_{z,h/W\geq 1}$ is independent of the mesh size in the range of $0\leq y\leq 0.4995$ on the interface outer edge. In the range of $0.4995\leq y\leq 0.5$, the values of singular stress ratio are higher if smaller mesh is applied, which means that the ISSF value continues to increase as the refinement of mesh. ISSF becomes singular and goes to infinity near the vertex if the reference is two-dimensional.

Table 4.4 The ratios of singular stresses when bonded plate is the reference

y	$\frac{\sigma_{z,h/W=0.01}^{3D,FEM} - \tilde{\sigma}_{z,h/W=0.01}^{3D}}{\sigma_{z,h/W\geq 1}^{2D,\mathrm{FEM}}}$	
	e_{min}=1/3200	e_{min}=1/12800
0	0.219	0.219
0.1053	0.220	0.219
0.2105	0.220	0.219
0.3158	0.220	0.219
0.4211	0.221	0.220
0.4474	0.221	0.221
0.4900	0.202	0.202
0.4950	0.181	0.181
0.4980	0.169	0.169
0.4985	0.170	0.170
0.4990	0.172	0.173
0.4992	0.175	0.175
0.4995	0.179	0.180
0.4996	0.177	0.183
0.4997	0.177	0.188
0.4998	0.193	0.194
0.4999	0.210	0.198
0.5	0.226	0.252

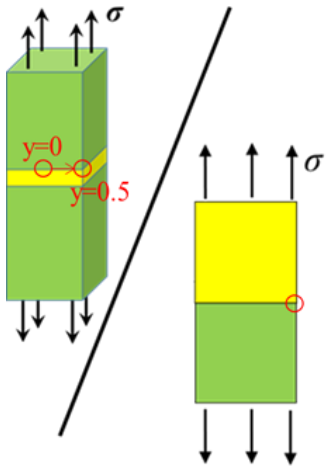

4.3 ISSF distribution and critical ISSF of three-dimensional butt joint

In this section, the adhesively bonded specimens used by Suzuki [1] are analyzed where the adherents S35C are bonded with adhesive epoxy resin. Suzuki's experimental specimens were analyzed by using two-dimensional butt joint model in Chapter 2. The elastic parameters of the adherent and adhesives are tabulated in Table 2.6. The experimental strength value σ_c is the maximum value of average axial stress obtained by dividing the tensile load by the area of the specimen cross section normal to the load. Fig. 2.8 shows the experimental tensile adhesive strength with different adhesive thicknesses.

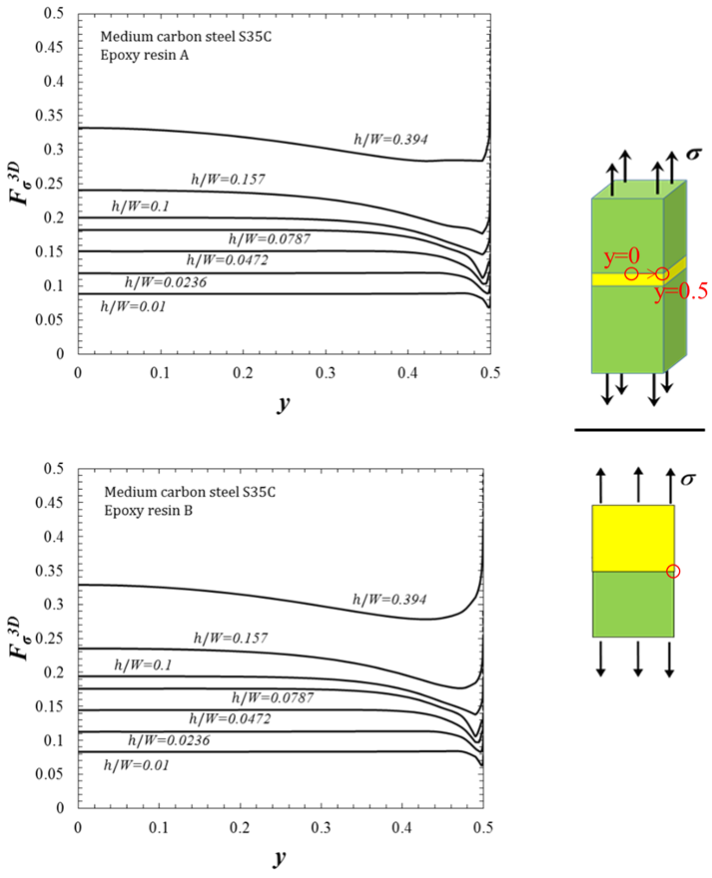

Fig. 4.4 ISSF distribution on the interface outer edge of three-dimensional butt joint

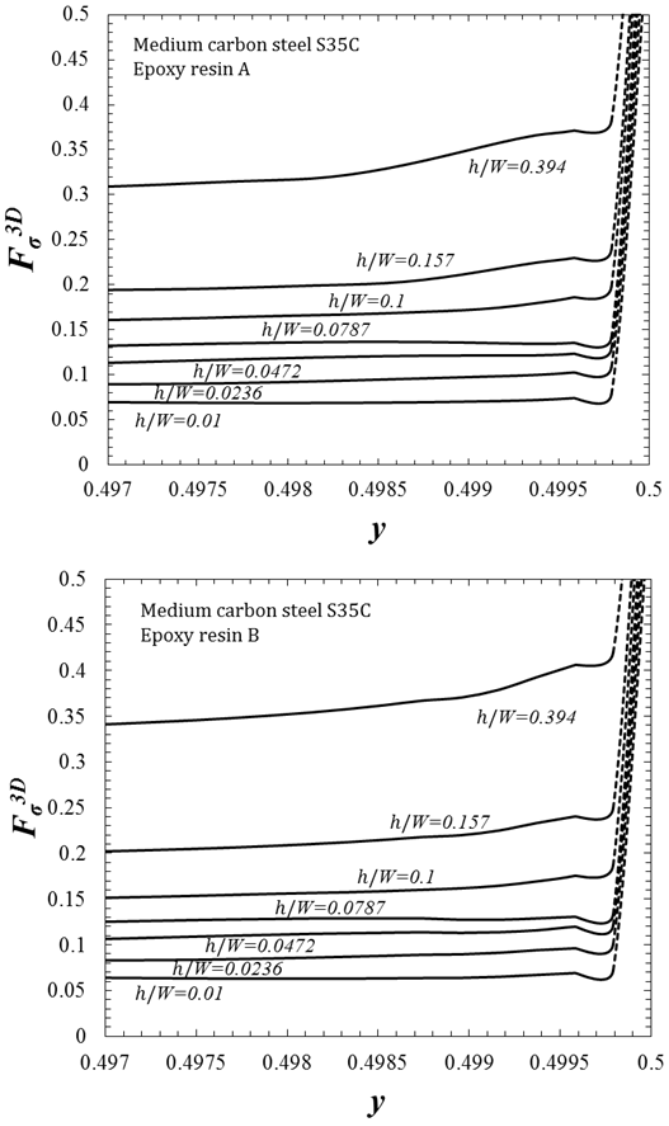

Fig. 4.5 ISSF distribution near the interface vertex

The ISSF distribution on the interface outer edge is obtained by using singular stress ratio according to Eq. (4.6) and shown in Fig. 4.4. The ISSF $F^{2D}_{\sigma,h/W\geq 1}$ for bonded plate (see Appendix A), which has been analyzed accurately by using the body force method in previous research, is used as the reference. The references $F^{2D}_{\sigma,h/W\geq 1}$ are 0.406 and 0.405 for material combination A and B. From Fig. 4.4 it can

be seen that F_{σ}^{3D} decreases with decreasing the adhesive thickness. The values of F_{σ}^{3D} are not accurate near the interface vertex because the reference is two-dimensional, as is explained in Table 4.4. The ISSF details near the interface vertex ($0.497 \leq y \leq 0.5$) are shown in Fig. 4.5. In the range of $0.4995 \leq y \leq 0.5$, ISSFs, which are denoted by dot lines, cannot be calculated, they go to infinity because of the singularity.

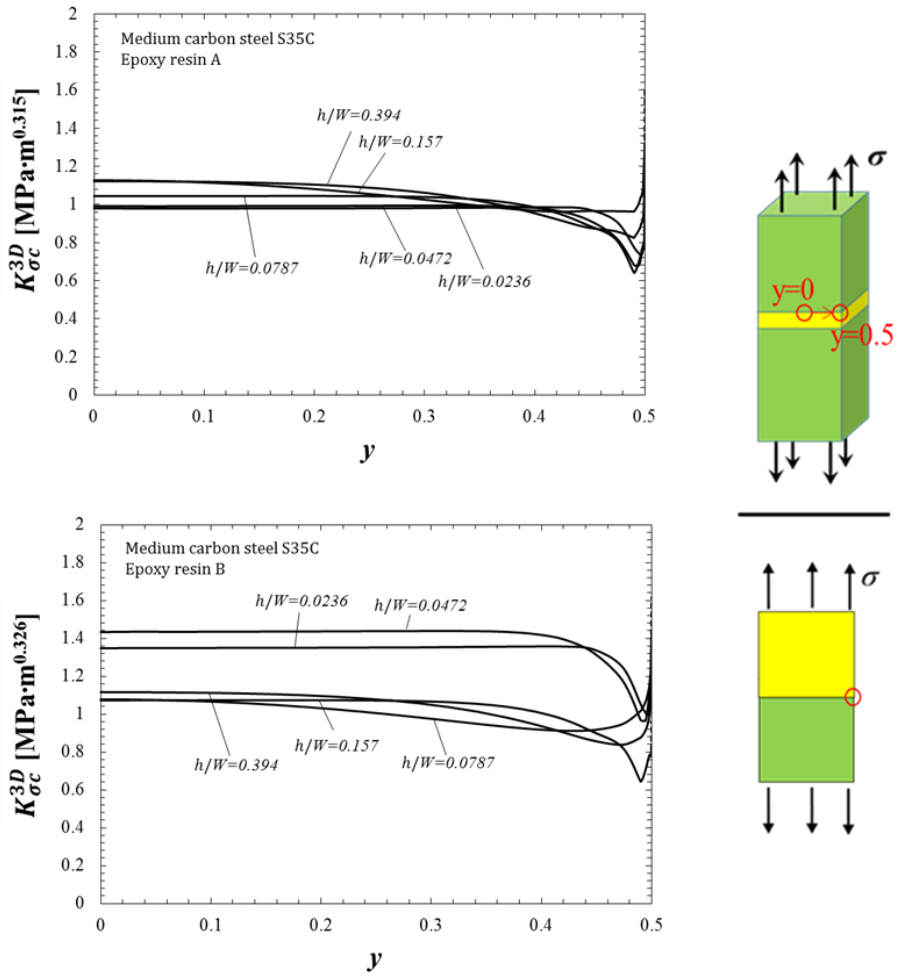

Fig. 4.6 Critical ISSF distribution on the interface outer edge of three-dimensional butt joint

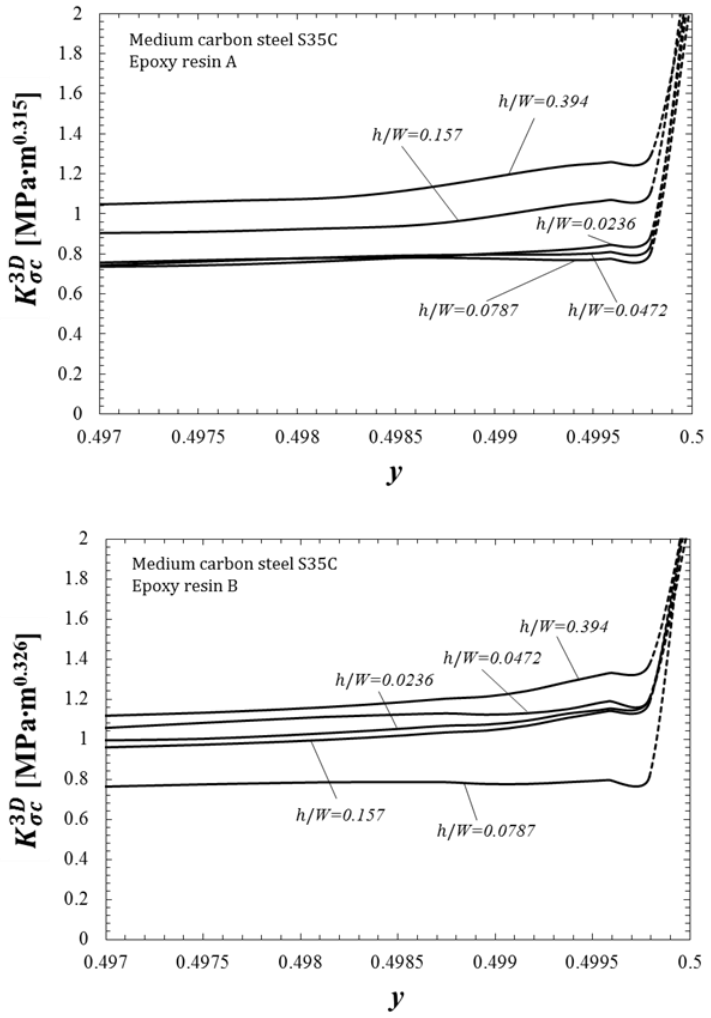

Fig. 4.7 Critical ISSF distribution near the interface vertex

The critical ISSF is expressed as $K_{\sigma c}^{3D}=F_{\sigma}^{3D}\sigma W_{exp}^{1-\lambda}$, W_{exp} is the width of the experimental specimen. Fig. 4.6 shows the distributions of critical ISSF $K_{\sigma c}^{3D}$ on the interface outer edge of three-dimensional butt joint, and Fig. 4.7 shows the critical ISSF details near the interface vertex ($0.497 \leq y \leq 0.5$). The critical ISSFs, which are denoted by dot lines, cannot be calculated, they go to infinity because of the singularity. In Fig. 4.6, the critical ISSF distribution curves are quite similar, So that we pick a point on the interface outer edge to investigate to confirm the coincidence of these curves. Fig. 4.8 shows the $K_{\sigma c}^{3D}$ at the middle point of interface outer edge

(y=0). In Fig. 4.8, the adhesive strength at the middle point of interface outer edge can be evaluated by the constant critical ISSF as $K_{\sigma c}^{3D}$=const. As is mentioned in Chapter 2, Suzuki's experimental specimens were analyzed by using two-dimensional butt joint model in previous study [5, 6]. Comparing with Fig. 2.3, $K_{\sigma c}^{3D}$ at y=0 coincides with the $K_{\sigma c}$ which is obtained by using two-dimensional butt joint model. Moreover, it can be found from the previous results that the ISSF on the interface outer edge have slight changes far away from the vertex, and go to infinity near the vertex. Therefore, on the interface outer edge of three-dimensional butt joint, the ISSF at one point can be obtained accurately by using two-dimensional butt joint model if this point is far enough away from the interface vertex.

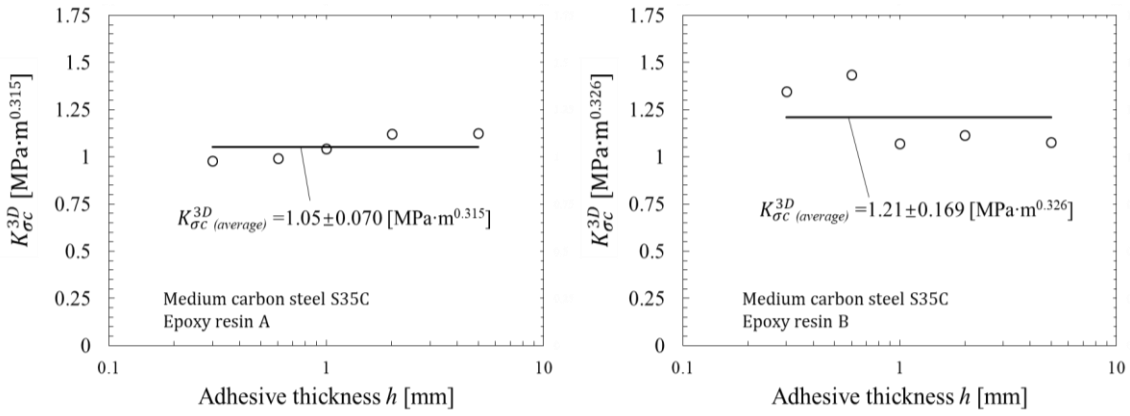

Fig. 4.8 Critical ISSF at y=0

4.4 ISSF distribution and critical ISSF of butt joint with rectangular cross section

The adhesively bonded specimens used by Akisanya and Meng [2] are analyzed in this section and the elastic parameters of the adherent and adhesives are tabulated in Table 4.5. The one-eighth model is used for the analysis as is shown in Fig. 4.9(b). For the butt joint with rectangular cross section, the long and short outer edge of the interface should be discussed respectively. The y coordinate value is used to describe the position on the long edge and the x coordinate value is used to describe the position on the short edge. Both y=15mm and x=5mm mean the point at the interface vertex.

Table 4.5 Material properties of adherent and adhesives

Combination			Young's modulus E [GPa]	Poisson's ratio ν	α	β	λ
C	Adherent	Aluminum	70	0.35	0.94	0.21	0.714
	Adhesive	Araldite	2.1	0.36			
D	Adherent	Brass	90	0.34	0.86	0.15	0.745
	Adhesive	Solder	6.4	0.39			

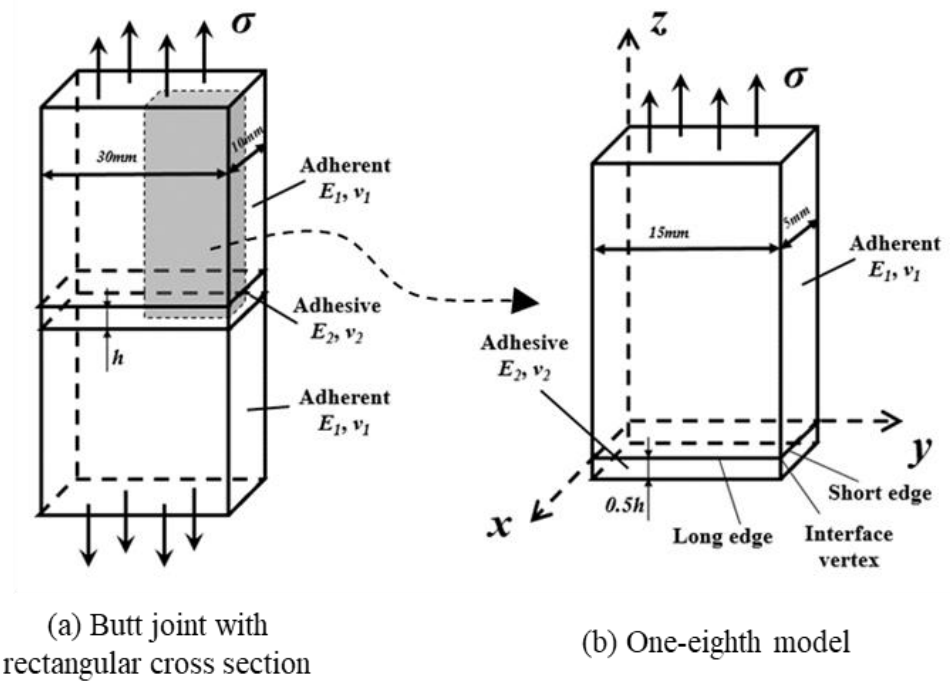

Fig. 4.9 The butt joint with rectangular cross section

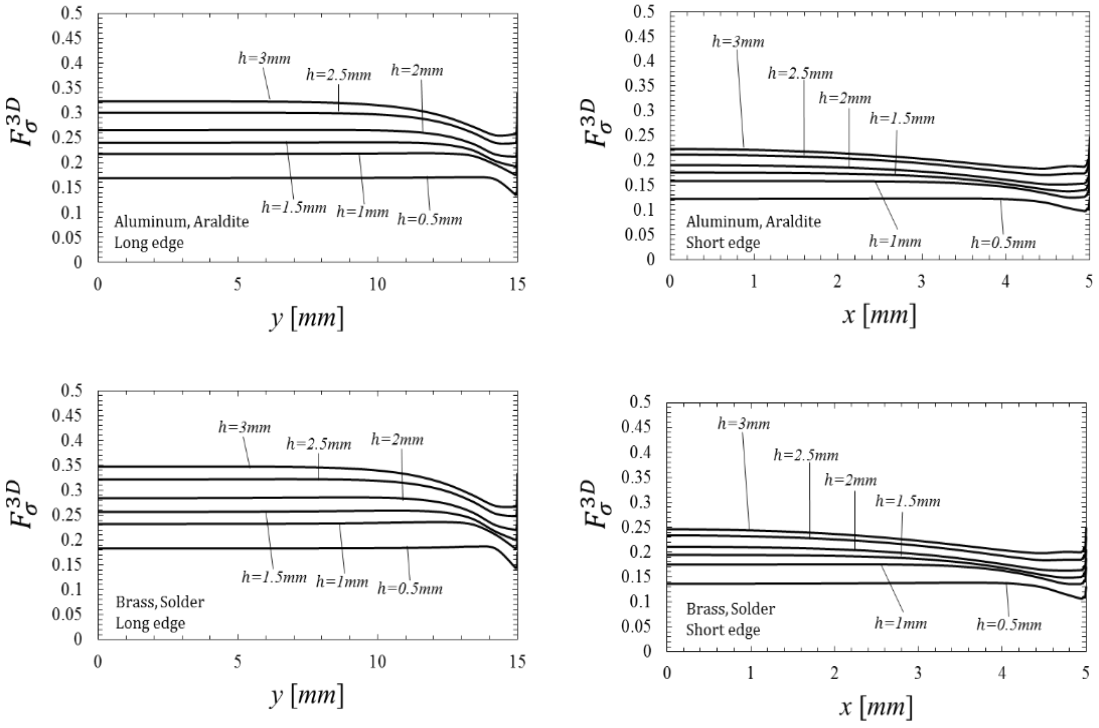

Fig. 4.10 ISSF distributions on the interface outer edges of butt joint with rectangular cross section

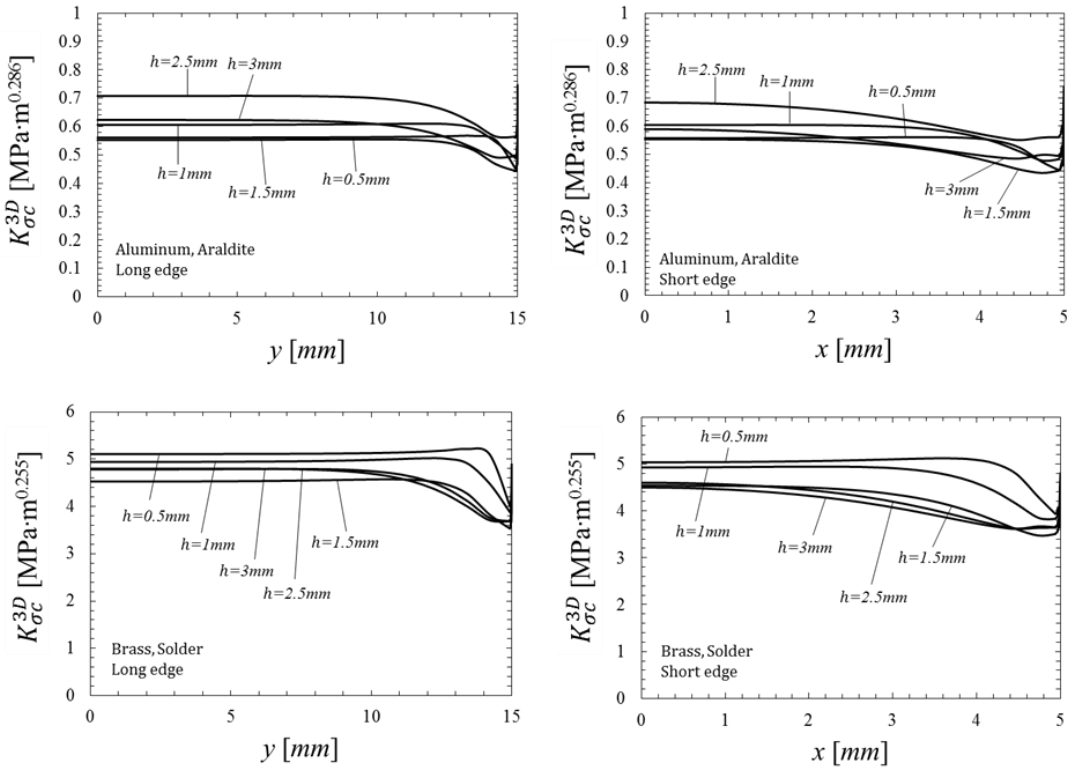

Fig. 4.11 Critical ISSF distributions on the interface outer edges of butt joint with rectangular cross section

The ISSF and critical ISSF of butt joint with rectangular cross section are obtained by using two-dimensional reference and shown in Fig. 4.10, Fig. 4.11 and Fig. 4.12. In Fig. 4.10 and Fig. 4.11, the ISSF and critical ISSF on the interface outer edge have slight changes far away from the vertex, and go to infinity near the vertex. From Fig. 4.12, it is seen that the critical ISSF is almost constant independent of the adhesive thickness.

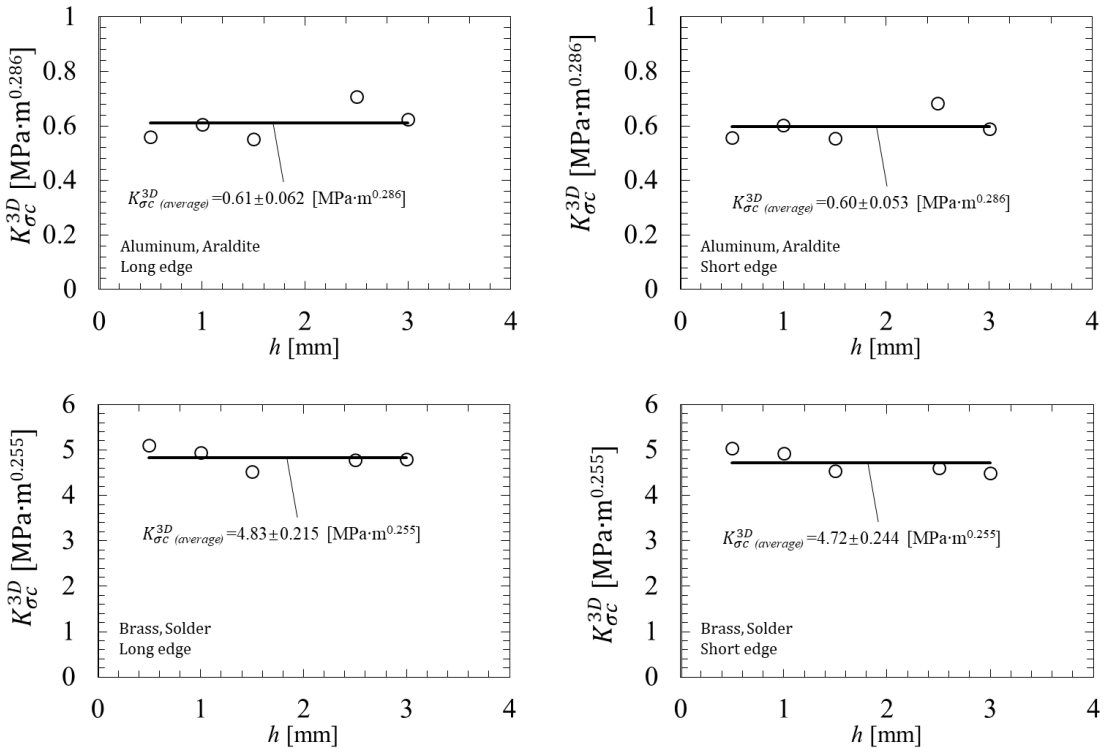

Fig. 4.12 Critical ISSF at x=0 and y=0

4.5 ISSF distribution of fillet corner

In previous discussion, the ISSF distribution on the interface outer edge of three-dimensional butt joint was calculated by using two-dimensional reference. However, the ISSF becomes singular and goes to infinity near the vertex if the reference is two-dimensional. In reality, no corner can be perfectly sharp, a manufactured sharp corner will always present a small fillet radius.

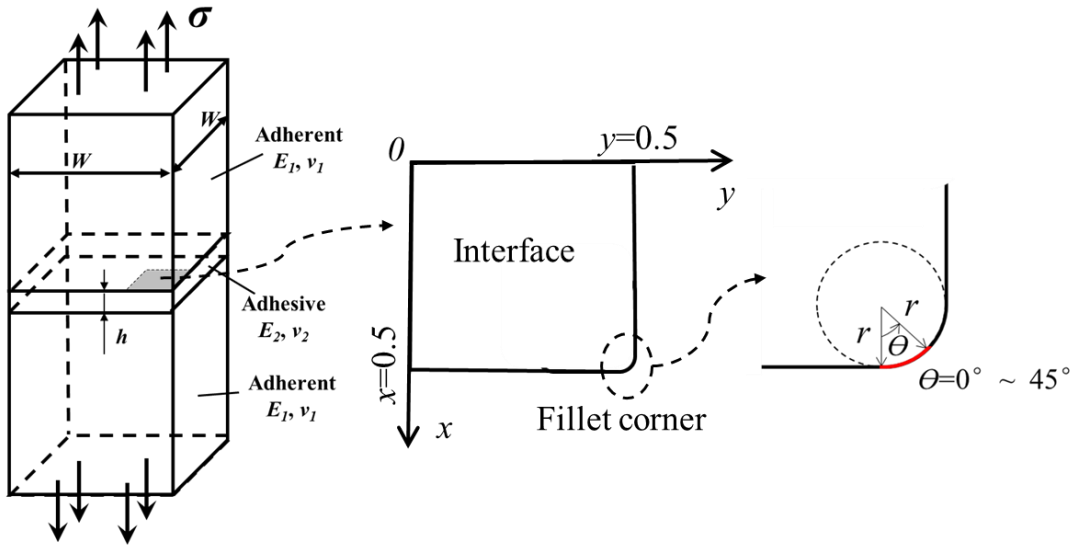

Fig. 4.13 Fillet corner in the interface

Fig. 4.13 shows a three-dimensional butt joint with fillets instead of the interface vertexes. The polar coordinate in the interface is used to describe the position on the fillet as shown in Fig. 4.13, r is the fillet radius. For the examples in this section, the elastic properties of the materials are Young's modulus E=210GPa and Poisson's ratio ν=0.3 for S35C, and E=3.14GPa and ν=0.37 for epoxy resin, same as the material combination A in Suzuki's experiment [1]. The adhesive thickness h/W is 0.01. The bonded plate is still the reference solution.

Table 4.6 shows the singular stress ratios on the fillet with different mesh size, r/W=0.0005 in this case. The non-singular stress on the fillet arc is calculated by using the displacement u_{r0} in the r direction, similarly to cylindrical butt joint. In Table 4.6, the singular stress ratio is independent of the mesh size on the fillet, therefore, the ratio can be used to calculate the ISSF for the fillet.

Table 4.6 Singular stress ratios on the fillet

θ °	$\frac{\sigma_{z,h/W=0.01}^{3D,FEM} - \tilde{\sigma}_{z,h/W=0.01}^{3D}}{\sigma_{z,h/W\geq 1}^{2D,\mathrm{FEM}}}$	
	$e_{min}=10^{-4}$	$e_{min}=5\mathrm{x}10^{-5}$
0	0.193	0.193
5	0.200	0.201
10	0.207	0.207
15	0.211	0.212
20	0.216	0.216
25	0.220	0.220
30	0.222	0.223
35	0.225	0.225
40	0.227	0.226
45	0.229	0.228

Fig. 4.14 shows the ISSF distributions on the interface outer edge when r/W=0 (vertex), r/W=0.0005, r/W=0.001 and r/W=0.01. Four cases have almost the same ISSF distribution on the interface outer edge, the effect of fillet on the ISSF distribution of edge is very small. Fig. 4.15 shows the ISSF distributions near the fillet and on the fillet arc. On the left side in Fig. 4.15, when r/W=0, the ISSF cannot be obtain in the range of $0.4995 \leq y \leq 0.5$; when r/W=0.0005, the fillet arc starts at y=0.4995; when r/W=0.001, the fillet arc starts at y=0.499; when r/W=0.01, the fillet arc starts at y=0.49. The ISSF on the edge decreases near the start point of fillet arc. On the right side in Fig. 4.15, when the fillet radius is small (r/W=0.0005 and r/W=0.001), the ISSF on the fillet arc continues to increase from θ=0° (start point of fillet arc) to θ=45°, and the ISSF is higher when fillet radius is smaller. The maximum ISSF on the fillet arc appears at the point θ=45°. When the fillet radius is large (r/W=0.01), the ISSF on the fillet arc is a constant.

Furthermore, when r/W=0.0005, the ISSF at θ=45° on the fillet arc is 0.089, which is equal to the ISSF at y=0 on the edge. Therefore, when $r/W \geq 0.0005$, the

adhesive strength can be evaluated by using the ISSF at the middle point (y=0) of the interface outer edge.

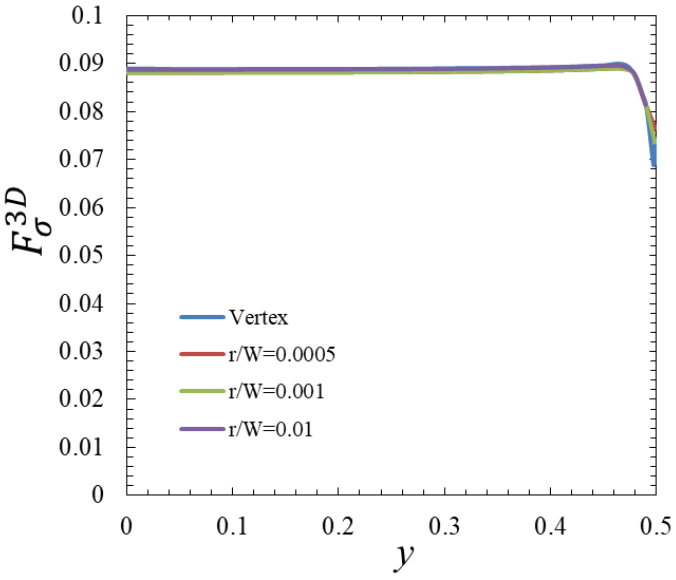

Fig. 4.14 ISSF distribution on the edge of fillet case

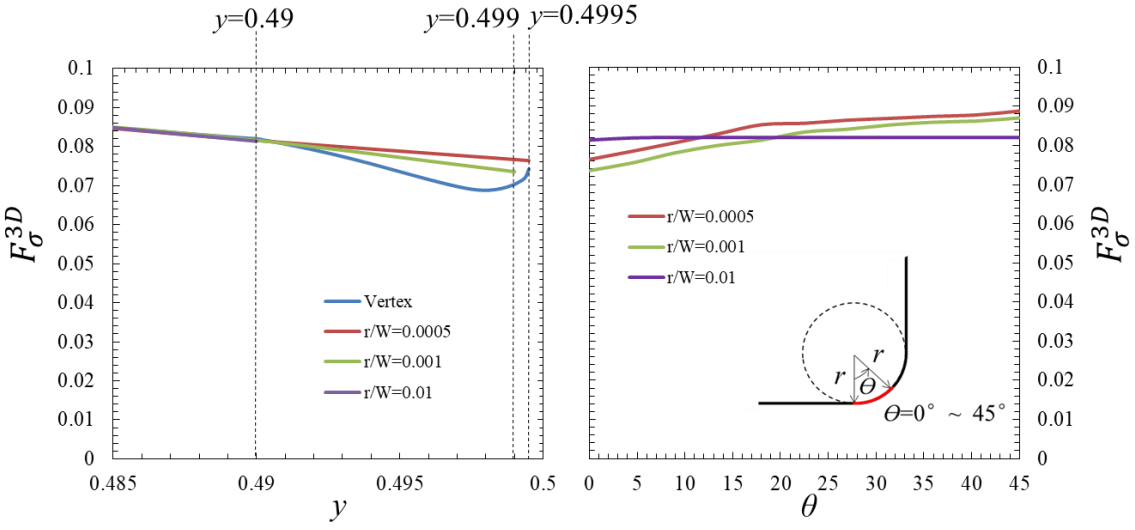

Fig. 4.15 ISSF distribution on the fillet arc

4.6 Conclusion

In this chapter, the adhesive strength of three-dimensional butt joint was studied in terms of the intensity of singular stress on the interface outer edge.

The interface stress distributions of three-dimensional butt joint were obtained by using different mesh sizes. The values of stress are almost same in the interior area of the interface, and quite different close to the interface outer edges. The mash size has an effect only on the stress close to the interface outer edges. The singularity occurs on the interface outer edges.

The stress distributions on the interface outer edge of three-dimensional butt joint were investigated by using the ratios of singular stresses. The ISSF decreases with the decreasing adhesive thickness h. For a fixed adhesive thickness h, the ISSF and critical ISSF have a little change far away from the vertex. The ISSF and critical ISSF become singular and go to infinity near the vertex if the reference is two-dimensional. It was also found that the adhesive strength on the interface outer edge can be evaluated by the constant critical ISSF as $K_{\sigma c}^{3D}$=const. The results at the middle points of interface outer edges coincide with the results obtained by using two-dimensional butt joint model in previous studies. On the interface outer edge of three-dimensional butt joint, the ISSF at one point can be calculated accurately by using two-dimensional butt joint model if this point is far enough away from the interface vertex.

The ISSF at interface vertex cannot yet be obtained, fillet was considered instead of the vertex. When the fillet radius $r/W \geq 0.0005$, the adhesive strength can be evaluated by using the ISSF at the middle point (y=0) of the interface outer edge.

4.7 Reference of Chapter 4

[1] Suzuki Y. Adhesive tensile strengths of scarf and butt joints of steel plates (relation between adhesive layer thicknesses and adhesive strengths of joints). JSME. Int. J., 30 (1987), 1042–51.

[2] Akisanya AR, Meng CS. Initiation of fracture at the interface corner of bi-material joints. Journal of the Mechanics and Physics of Solids, 51 (2003), 27-46.

[3] Li YL, Hu SY, Munz D, Yang YY. Asymtotic description of the stress field around the bond edge of a cylindrical joint. Archive of Applied Mechanics, 68 (1998), 552–565.

[4] Miyazaki T, Noda NA, Sano Y. A comparison of intensities of singular stress field for bonded cylinder under tension and bending. Trans. JSME., 82 (2016), 16-00222.

[5] Noda, N.A., Miyazaki, T., Li, R., Uchikoba, T., Sano, Y., Takase, Y., Debonding Strength Evaluation in Terms of the Intensity of Singular Stress at the corner with and without fictitious crack, Int. J. Adhes. Adhes., 61 (2015), 46-64.

[6] Noda, N.A., Miyazaki, T., Uchikoba, T., Li, R., Sano, Y., Takase, Y., Convenient Debonding Strength Evaluation Based on the Intensity of Singular Stress for Adhesive Joints. Transactions of The Japan Institute of Electronics Packaging, 17 (2014), 132-142.

Chapter 5 Conclusion

Adhesive joints are widely used in numerous industrial sectors, such as automobile, shipbuilding and aeronautics. However, as is known that there is stress singularity at the end of interface for different materials, which may result in the failure of the joint. The intensity of singular stress has already been discussed for bonded plate under arbitrary material combination, while few studies are available for the intensity of butt joints in axi-symmetrical and three-dimensional problems, and no results with varying material combination. Thus this research concentrated on the analysis of ISSFs (intensity of singular stress field) of axi-symmetrical and three-dimensional butt joint problems, which may make a contribution on a general understanding of the strength for the axi-symmetrical and three-dimensional problems. This thesis is concluded as follows.

1. The ISSF variations were clarified over the entire adhesive thickness range for plate butt joint. For the plate butt joint, the ISSF $F_\sigma^{P*}=K_\sigma^P/\sigma h^{1-\lambda}$ normalized by adhesive thickness h becomes constant with decreasing adhesive thickness when $h/W \leq 0.01$. In this case, the adhesive joint can be regarded in a semi-infinite plate. If the adhesive layer is thin, F_σ^{P*} is more suitable because the variation is smaller than the variation of $F_\sigma^P=K_\sigma^P/\sigma W^{1-\lambda}$. To improve the interface strength, thin adhesive layers are desirable.

2. For a certain value β, it is found that F_σ^{P*} decreases with increasing α. Since

the solution for case of $h/W \geq 1.0$ was shown in the Appendix A, the accurate results can be obtained by the interpolation also in the range of $0.01 \leq h/W \leq 1.0$.

3. The ISSF variations were also clarified over the entire adhesive thickness range for cylindrical butt joint. For the cylindrical butt joint, the circumferential strain at the interface end, ε_{r0}^{C}, is not influenced by the stress singularity because ε_{r0}^{C} is obtained from the radial displacement u_{r0}^{C} and the cylinder radius. It was found that the non-singular stresses caused by the ε_{r0}^{C} are contained in the FEM stresses at the interface end. The accurate method was used for calculating the ISSF from the ratio of the stress obtained by subtracting the non-singular stress to the stress of the plate butt joint adopted as the reference solution. The stress-free boundary condition causes the non-singular stresses $\tilde{\sigma}_{r0,FEM}^{C} = \tilde{\tau}_{rz0,FEM}^{C} = 0$. The ISSF can be calculated easily without subtraction process of the non-singular stresses when the radial stress $\sigma_{r0,FEM}^{C}$ or the shear stress $\tau_{rz,FEM}^{C}$ is used.

4. For a certain material combination, the ISSF F_{σ}^{C*} normalized by adhesive thickness h becomes constant with decreasing adhesive thickness when $h/W \leq 0.01$. Thin adhesive layer can be used to improve the interface strength of the cylindrical butt joint. Since the ISSFs of the cylindrical butt joint cannot be totally dominated by the Dundurs' parameter α and β, the maximum and minimum values of the $K_{\sigma}^{C}/K_{\sigma}^{P}$ and $\sigma_{z0,\,FEM}^{C}/\sigma_{z0,\,FEM}^{P}$ were shown in the charts and tables for various (α, β). The value $K_{\sigma}^{C}/K_{\sigma}^{P}$ may be useful for predicting the debonding strength under the bad pairs $\alpha(\alpha\text{-}2\beta)>0$. On the other side, the $\sigma_{z0,\,FEM}^{C}/\sigma_{z0,\,FEM}^{P}$ may be more important for predicting the debonding strength under the good pairs $\alpha(\alpha\text{-}2\beta)\leq 0$. Since the solution for $h/W \geq 1.0$ was shown in the Appendix B, the accurate results can be obtained by the interpolation also in the range for $0.01 \leq h/W \leq 1.0$.

5. $\left(K_\sigma^C\right)_{max}/K_\sigma^P$ is less than 1.5 for most of the bad pair region. The difference between $\left(\sigma_{z0,\,FEM}^C/\sigma_{z0,\,FEM}^P\right)_{\max}$ and $\left(\sigma_{z0,\,FEM}^C/\sigma_{z0,\,FEM}^P\right)_{\min}$ is less than 10%. Dundurs' parameters α and β can almost control the results and be used for axi-symmetrical bonded structures.

6. The interface stress distributions of three-dimensional butt joint were obtained by using different mesh sizes. The values of stress are almost same in the interior area of the interface, and quite different close to the interface outer edges. The mash size has an effect only on the stress close to the interface outer edges. The singularity occurs on the interface outer edges.

7. The stress distributions on the interface outer edge of three-dimensional butt joint were investigated by using the ratios of singular stresses. The ISSF decreases with the decreasing adhesive thickness *h*. For a fixed adhesive thickness *h*, the ISSF and critical ISSF have a little change far away from the vertex. The ISSF and critical ISSF become singular and go to infinity near the vertex if the reference is two-dimensional. It was also found that the adhesive strength on the interface outer edge can be evaluated by the constant critical ISSF as $K_{\sigma c}^{3D}$=const.

8. The results at the middle points of interface outer edges coincide with the results obtained by using two-dimensional butt joint model in previous studies. On the interface outer edge of three-dimensional butt joint, the ISSF at one point can be calculated accurately by using two-dimensional butt joint model if this point is far enough away from the interface vertex.

9. The ISSF at interface vertex cannot yet be obtained, fillet is considered instead of the vertex. When the fillet radius $r/W \geq 0.0005$, the adhesive strength can be evaluated by using the ISSF at the middle point (y=0) of the interface outer edge.

Appendix

Appendix A: ISSF for the bonded plate

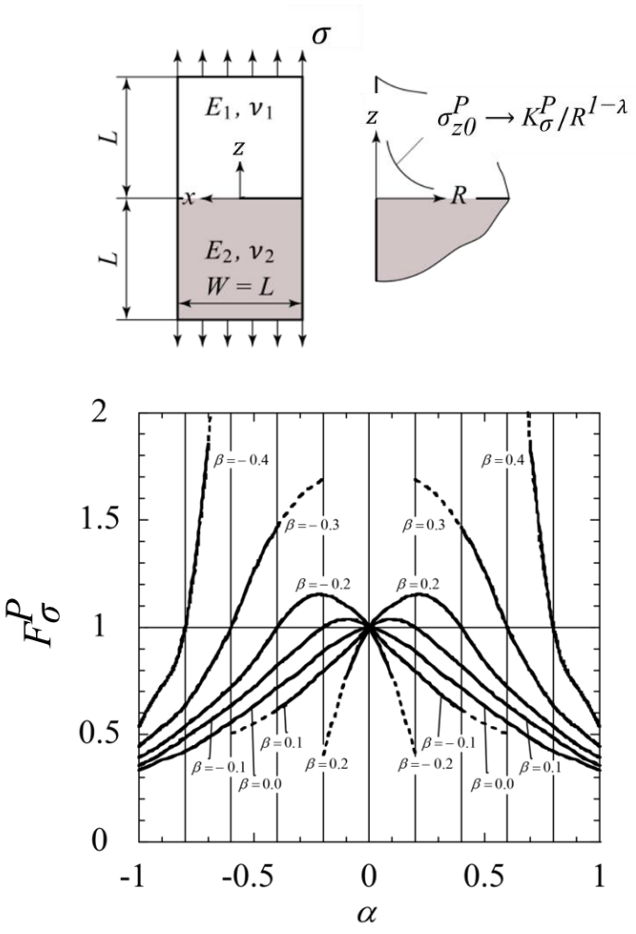

Fig. A1 ISSF for the bonded plate ($h/W \geq 1.0$)

Fig. A1 shows the ISSF F_σ^P for the bonded plate calculated by varying Dundurs' parameter (α, β) [1]. The bonded plate in Fig.A1 can be regarded as a plate butt joint

with a very thick adhesive layer $h/W \geq 1.0$. The F_σ^P values are obtained by the body force method under the bad pair condition of $\alpha(\alpha-2\beta)>0$ [1] and obtained by FEM under the good pair condition of $\alpha(\alpha-2\beta)<0$ [2-5]. Since the solution for thin adhesive layer $h/W \leq 0.01$ is indicated in Table 2.5 and Fig. 2.7 under aribitrary material combination, the accurate results can be obtained by the interpolation also in the range of $0.01 \leq h/W \leq 1.0$.

Table A1 F_σ^P of bonded plate ($h/W \geq 1.0$)

		β								
		-0.4	-0.3	-0.2	-0.1	0.0	0.1	0.2	0.3	0.4
α	-1.00	0.540	0.446	0.395	0.357	0.332	—	—	—	—
	-0.95	0.643	0.491	0.422	0.381	0.349	—	—	—	—
	-0.90	0.726	0.534	0.456	0.412	0.381	—	—	—	—
	-0.80	1.000	0.636	0.538	0.487	0.450	—	—	—	—
	-0.70	1.855	0.800	0.626	0.558	0.486	—	—	—	—
	-0.60	3.291	1.000	0.724	0.638	0.559	0.505	—	—	—
	-0.50	—	1.264	0.842	0.722	0.635	0.551	—	—	—
	-0.40	—	1.467	1.000	0.822	0.718	0.615	—	—	—
	-0.30	—	1.609	1.118	0.913	0.796	0.697	—	—	—
	-0.20	—	1.690	1.153	1.000	0.889	0.797	0.404	—	—
	-0.10	—	—	1.103	1.037	0.955	0.890	0.767	—	—
	0.00	—	—	1.000	1.000	1.000	1.000	1.000	—	—
	0.10	—	—	0.767	0.890	0.955	1.037	1.103	—	—
	0.20	—	—	0.404	0.797	0.889	1.000	1.153	1.690	—
	0.30	—	—	—	0.697	0.796	0.913	1.118	1.609	—
	0.40	—	—	—	0.615	0.718	0.822	1.000	1.467	—
	0.50	—	—	—	0.551	0.635	0.722	0.842	1.264	—
	0.60	—	—	—	0.505	0.559	0.638	0.724	1.000	3.291
	0.70	—	—	—	—	0.486	0.558	0.626	0.800	1.855
	0.80	—	—	—	—	0.450	0.487	0.538	0.636	1.000
	0.90	—	—	—	—	0.381	0.412	0.456	0.534	0.726
	0.95	—	—	—	—	0.349	0.381	0.422 (0.422)	0.491	0.643
	1.00	—	—	—	—	0.332	0.357	0.395	0.446	0.540

Appendix B: ISSF for the bonded cylinder in comparison with the bonded plate

In the previous study [6], the ISSF of bonded cylinder was compared with the ISSF of bonded plate under arbitrary material combination. The bonded cylinder can be regarded as a cylindrical butt joint with a very thick adhesive layer $h/W \geq 1.0$. Fig. B1, Table B1 and B2 show the maximum values and the minimum values of K_σ^C/K_σ^P and $\sigma_{z0,\,FEM}^C/\sigma_{z0,\,FEM}^P$ calculated by varying (α, β).

The solid lines indicate K_σ^C/K_σ^P under $\alpha(\alpha-2\beta)>0$ and $\sigma_{z0,\,FEM}^C/\sigma_{z0,\,FEM}^P$ under $\alpha(\alpha-2\beta)<0$. The dot lines indicate $\sigma_{z0,\,FEM}^C/\sigma_{z0,\,FEM}^P$ under $\alpha(\alpha-2\beta)>0$. The circle marks indicate $\sigma_{z0,\,FEM}^C/\sigma_{z0,\,FEM}^P$ for $\alpha(\alpha-2\beta)=0$.

All K_σ^C/K_σ^P values are distributed between $\left(K_\sigma^C\right)_{max}/K_\sigma^P$ and $\left(K_\sigma^C\right)_{min}/K_\sigma^P$. $\left(K_\sigma^C\right)_{max}/K_\sigma^P$ go to infinity when $\alpha \rightarrow 2\beta$. The solid lines are very important for predicting the debonding strength except for the bad pair condition near $\alpha \cong 2\beta$. There are only 10% differences between $\left(K_\sigma^C\right)_{max}/K_\sigma^P$ and $\left(K_\sigma^C\right)_{min}/K_\sigma^P$ except for the bad pair condition near $\alpha \cong 2\beta$, K_σ^C/K_σ^P and $\sigma_{z0,\,FEM}^C/\sigma_{z0,\,FEM}^P$ can be almost controlled by (α, β). Since the solution for thin adhesive layer $h/W \leq 0.01$ is indicated in Table 3.7, Table 3.8, Fig. 3.7 and Fig. 3.7 under aribitrary material combination, the accurate results can be obtained by the interpolation also in the range of $0.01 \leq h/W \leq 1.0$.

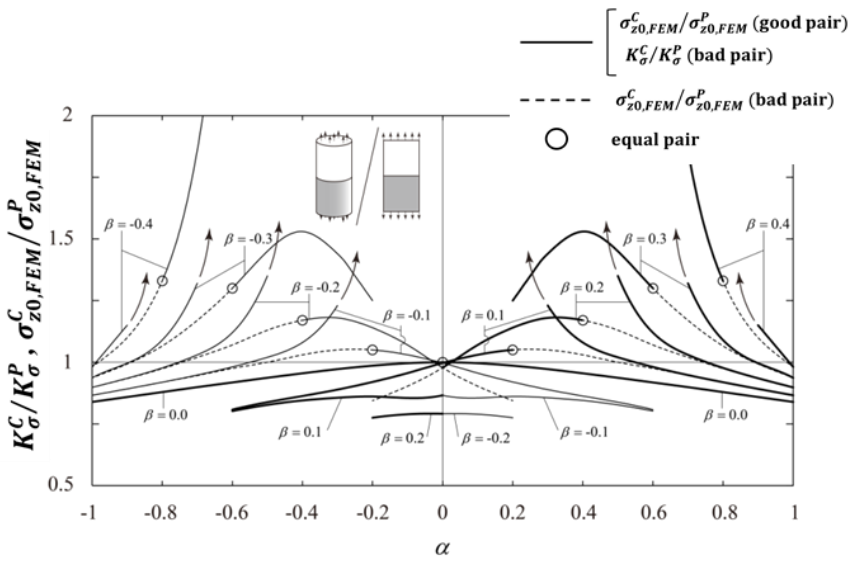

(a) Maximum values

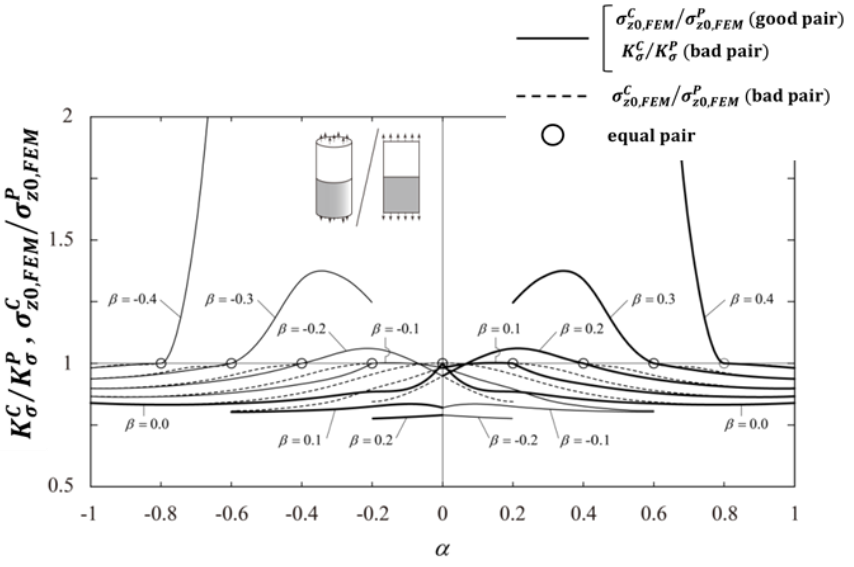

(b) Minimum values

Fig. B1 K^C_σ/K^P_σ and $\sigma^C_{z0,\,FEM}/\sigma^P_{z0,\,FEM}$ in $(\alpha,\ \beta)$ map for bonded cylinder (h/W≥1.0)

Table B1 Maximum and minimum values of K_σ^C / K_σ^P of bonded cylinder ($h/W \geq 1.0$)

		β										
		-0.45	0.4	0.3	-0.2	-0.1	0.0	0.1	0.2	0.3	0.4	0.45
α	-1.0	0.995	0.981	0.937	0.898	0.866	0.839					
	-0.9		1.146 0.992	0.996 0.944	0.935 0.899	0.892 0.863	0.859 0.834					
	-0.8			1.089 0.957	0.977 0.906	0.919 0.865	0.879 0.832					
	-0.7			1.321 0.976	1.032 0.918	0.948 0.870	0.899 0.833					
	-0.6				1.121 0.936	0.981 0.88	0.918 0.837	0.802				
	-0.5				1.346 0.962	1.022 0.895	0.937 0.843	0.827 0.804				
	-0.4					1.084 0.916	0.955 0.854	0.845 0.808				
	-0.3					1.234 0.944	0.972 0.87	0.856 0.814				
	-0.2						0.986 0.885	0.861 0.825	0.775			
	-0.1						0.996 0.896	0.855 0.835	0.789 0.781			
	0.0				0.791 0.789	0.866 0.820	1.000	0.866 0.820	0.791 0.789			
	0.1				0.789 0.781	0.855 0.835	0.996 0.896					
	0.2				0.775	0.861 0.825	0.986 0.885					
	0.3					0.856 0.814	0.972 0.870	1.234 0.944				
	0.4					0.845 0.808	0.955 0.854	1.084 0.916				
	0.5					0.827 0.804	0.937 0.843	1.022 0.895	1.346 0.962			
	0.6					0.802	0.918 0.837	0.981 0.88	1.121 0.936			
	0.7						0.899 0.833	0.948 0.870	1.032 0.918	1.321 0.976		
	0.8						0.879 0.832	0.919 0.865	0.977 0.906	1.089 0.957		
	0.9						0.859 0.834	0.892 0.863	0.935 0.899	0.996 0.944	1.146 0.992	
	1						0.839	0.866	0.898	0.937	0.981	0.995

Upper: maximum value, lower: minimum value

Table B2 Maximum and minimum values of $\sigma^{C}_{z0,\,FEM}/\sigma^{P}_{z0,\,FEM}$ of bonded cylinder ($h/W \geq 1.0$)

		β										
		-0.45	-0.4	-0.3	-0.2	-0.1	0.0	0.1	0.2	0.3	0.4	0.45
α	-1.0	0.995	0.981	0.937	0.898	0.866	0.839					
	-0.9	1.237 1.000	1.098 0.994	0.993 0.945	0.934 0.900	0.892 0.864	0.859 0.834					
	-0.8	2.276	1.327 1.000	1.066 0.962	0.974 0.909	0.919 0.866	0.879 0.833					
	-0.7		1.862 1.564	1.165 0.986	1.020 0.925	0.946 0.875	0.899 0.835					
	-0.6		3.117	1.299 1.000	1.071 0.951	0.975 0.890	0.918 0.843					
	-0.5			1.447 1.134	1.127 0.983	1.000 0.914	0.937 0.857					
	-0.4			1.525 1.343	1.172 1.000	1.031 0.948	0.955 0.880					
	-0.3			1.444 1.358	1.184 1.036	1.050 0.984	0.972 0.914					
	-0.2			1.246	1.145 1.060	1.052 1.000	0.986 0.955					
	-0.1				1.065 1.022	1.032 1.000	0.996 0.989					
	0.0				0.978 0.948	0.997 0.981	1.000	0.997 0.981	0.978 0.948			
	0.1				0.903 0.878	0.956 0.936	0.996 0.989	1.032 1.000	1.065 1.022			
	0.2				0.844	0.920 0.896	0.986 0.955	1.052 1.000	1.145 1.060	1.246		
	0.3					0.889 0.850	0.972 0.914	1.050 0.984	1.184 1.036	1.444 1.358		
	0.4					0.863 0.826	0.955 0.880	1.031 0.948	1.172 1.000	1.525 1.343		
	0.5					0.838 0.812	0.937 0.857	1.000 0.914	1.127 0.983	1.447 1.134		
	0.6					0.808	0.918 0.843	0.975 0.890	1.071 0.951	1.299 1.000	3.117	
	0.7						0.899 0.835	0.946 0.875	1.020 0.925	1.165 0.986	1.862 1.564	
	0.8						0.879 0.833	0.919 0.866	0.974 0.909	1.066 0.962	1.327 1.000	2.276
	0.9						0.859 0.834	0.892 0.864	0.934 0.900	0.993 0.945	1.098 0.994	1.237 1.000
	1.0						0.839	0.866	0.898	0.937	0.981	0.995

Upper: maximum value, lower: minimum value

Reference of Appendix

[1] Noda, N.A, Shirao, R., Li, J., Sugimoto, J.S., Intensity of Singular Stress at the End of a Fiber under Pull-out Force, International Journal of Solids and Structures, 44 (2007), 4472-4491.

[2] Zhang, Y., Noda, N.A., Takaishi, K.T., Lan, X., Effect of Adhesive Thickness on the Interface of Singular Stress at the Adhesive Dissimilar Joint. Transactions of the Japan Society of Mechanical Engineers Series A, 77(2011), 360-372.

[3] Zhang, Y., Noda, N.A, Wu, P.Z, Duan, M.L., A Mesh-Independent Technique to Evaluate Stress Singularities in Adhesive Joints, International Journal of Adhesion & Adhesives, 57 (2015), 105-117.

[4] Zhang, Y., Noda, N.A., Wu, P. and Duan, M., Corrigendum to "A mesh-independent technique to evaluate stress singularities in adhesive joints". International Journal of Adhesion and Adhesives, 60 (2015), 130.

[5] Noda, N.A., Miyazaki, T., Uchikoba, T., Li, R., Sano, Y., Takase, Y., Convenient Debonding Strength Evaluation Based on the Intensity of Singular Stress for Adhesive Joints. Transactions of The Japan Institute of Electronics Packaging, 17 (2014), 132-142.

[6] Miyazaki, T., Noda, N.A., Ren, F., Wang, Z., Sano, Y., Iida, K., Analysis of intensity of singular stress field for bonded cylinder and bonded pipe in comparison with bonded plate. International Journal of Adhesion and Adhesives, 77 (2017), 118-137.